HIGH-TEMPERATURE SUPERCONDUCTING RING MAGNET

Muhammad Zulfiqar Ali

Institute of Energy and Environment

Department of Electronic and Electrical Engineering

University of Strathclyde

This dissertation submitted for the degree of Doctor of Philosophy

December 2020

DECLARATION

This thesis is the result of the author's original research. It has been composed by the author and has not been previously submitted for the examination which has led to the award of a degree.

The copyright of this thesis belongs to the author under the terms of the United Kingdom Copyright Acts as qualified by University of Strathclyde Regulation 3.50. The due acknowledgement must always be made of the use of any material contained in, or derived from, this thesis.

Signed:____

Date:____

Muhammad Zulfiqar Ali

ABSTRACT

Many electrical engineering applications such as motors and generators use permanent magnets which approximately account for 45% of their electricity consumption. The conventional magnets in use have a maximum field of around 1.5-2 T. High performance superconducting materials such as REBCO have facilitated the development of superconducting magnets. Superconducting bulk magnets and stacks of tapes have already demonstrated the extraordinary potential to trap magnetic fields of very high order with very compact sizes. This has significantly increased the efficiency of rotating machines and improved power/torque density, while having low synchronous reactance with large overloading capacity, high transient stability with low noise and harmonic content with the additional cost of cooling.

This thesis focuses on a new type of superconducting magnet which uses superconducting tape as the field source. The most significant limiting factor for superconducting magnets is their size. This new superconducting magnet has made possible the development of HTS magnets with flexible sizes by splitting the 2G HTS tapes to form the persisitent current rings. By stacking HTS closed loop rings into a compact magnet, our HTS ring magnet has been proven to generate a trapped magnetic field higher than 5 T. The main advantage of the new magnet compared to existing trapped field HTS magnets is that the magnetic field lies parallel to the ab plane of the HTS, leading to higher critical currents in the same magnetic field. This thesis reports our key findings so far. Two different stacking configuration magnet samples were tested using the field cooling magnetization at 25 K and 4.2 K, with magnet diameter 90 mm and 150 mm, respectively. Over 4.6 T of the trapped field has been reported by using SuperPower tapes with a field cooling process at 25 K, which is the highest field trapped in the ring magnets for first configuration. A new stacking design was proposed to improve magnetic field distribution within the magnet and has the potential to trap more magnetic field with the estimated trap field of 9.4 T at 4.2 K. A three dimensional model was developed to simulate the performance of the ring magnets, and good agreements between experiment and simulation have been achieved. The new HTS permanent magnet with improved field homogenisation and large diameter is promising for medical imaging applications, as well as propulsion applications.

ACKNOWLEDGEMENTS

I would like to thank all those who have helped and supported me while researching this thesis. I would like to express my sincere and deepest gratitude to my supervisor, Dr Min Zhang, for the invaluable support and guidance she has given me throughout my studies. With her support, I am able to complete this novel work. Also, I would like to thank Dr Weijia Yuan for his generous advice and support.

I am grateful to Dr Richard O'Leary for his invaluable help, for impregnation of my samples which make it possible to achieve good experimental results. I also would like to thank all the staff in the institute of energy and environment at the University of Strathclyde for creating an atmosphere of friendship and cooperation.

At the University of Cambridge, I would like to thank technical officer Anthony Dennis, for his help and time during the experimental work done at the University of Cambridge.

I would also like to thanks my colleagues, in no particular order, Dr Fei Liang, Dr Yawei Wang, Dr Mariam Elsheikh, Dr Mohammad Yazdani Asrami, Muhammad Haseeb Iftikhar, Felix Huber, Zixuan Zhu, Fangjing Weng, Tian Lan, Abdelrahman Elwakeel, Zhishu Qiu, Zhidun Zeng.

Last but not least, I am grateful to my parents, brothers and sister who always love and pray for me unconditionally and gave me enormous encouragement through all my study and life. Thanks to my wife, for being by my side all the time and sharing both the pain and the happiness. Without their love, I would not have achieved all that I have thus far.

Publication

M. Z. Ali, J. Zheng, F. Huber, Z. Zhang, W. Yuan, and M. Zhang, “4.6 T generated by a high temperature superconducting ring magnet,” *Supercond. Sci. Technol.*, vol. 33, no. 4, p. 04LT01, Mar. 2020.

CONTENTS

LIST OF TABLES

LIST OF FIGURES

LIST OF ABBREVIATIONS AND ACRONYMS

CC	Coated conductors
FC	Field Cooling
FEM	Finite element method
FLL	Flux lines lattice
GL	Ginzburg-Landau
HTS	High temperature superconductor
IBAD	Ion beam assisted deposition
LTS	Low temperature superconductor
MOCVD	Metal Organic Chemical Vapour Deposition
MOD	Metal Organic Deposition
MUMPS	Multifrontal Massively Parallel sparse direct Solver
PCM	Phase change material
PDE	Partial differential equation
PLD	Pulse Laser Deposition
PM	Permanent magnet
RABiTS	Rolling Assisted Biaxially Textured Substrate
RE	Rare earth
RCE-DR	Reactive Co-Evaporation Deposition & Reaction
SC	Superconductor
TAFF	Thermally assisted flux flow
VTI	variable temperature insert
ZFC	Zero field cooling

LIST OF SYMBOLS

A	Magnetic vector potential
B	Magnetic flux density
H_c	Critical magnetic field
H_{c1}	Lower critical magnetic field
H_{c2}	Upper critical magnetic field
ξ	Coherence length
λ	Penetration depth
$\boldsymbol{J}$	Current density
J_c	Critical current density
Φ_0	Fluxon (quantum of magnetic flux)
f_p	Pinning force
f_l	Lorentz force
H_{irr}	Irreversibility magnetic field
B_{tr}	Trapped magnetic flux
ρ_{ff}	Flux flow resistivity
ρ_c	Flux creep resistivity
E	Electric field
M	Magnetization

1 INTRODUCTION

The annual electric consumption of the world is estimated to reach 200 trillion kWh by the year 2030 [1]. As the world population is continuously increasing and energy sources are depleting, our energy consumption methods are unsustainable. Practical contributions by scientists and engineers are required to reduce energy consumption without disturbing product quality and productivity. Electric motors account for approximately two-thirds of the worlds energy consumption [2]. The electrical energy consumption of the machines can be minimised either by increasing the machine efficiency, by using better power electronics circuits, or by using better quality materials for machine manufacturing [3]. The main reason for energy dissipation in machines is resistivity to current flow, which wastes energy resources.

Superconductors have zero resistance to electric current below the critical temperature, so they have improved efficiency when used in electrical systems. High-temperature superconductors (HTS) are more promising as compared to low-temperature superconductors, as HTS even at high temperatures have large current densities and high efficiencies. 2G HTS conductors are available in long lengths which make them potential candidates for power applications.

High-temperature superconductors (HTS) have been used to construct HTS magnets for applications such as high field coils, NMR, MRI, magnetic levitation, flywheel energy applications, magnetic bearings, fault current limiters and transformers. One of the main application currently being developed for superconducting magnets is superconducting motor and generator. In electric machines, superconducting magnets provides two main advantages; first, they have good quench performance, and secondly, they have good field quality. Superconducting magnets have the potential to trap high magnetic fields, this higher field results in a higher power or torque density, which enables to design robust, compact and lightweight machines [4]. Two types of superconducting magnets have already been designed and tested, which are discussed in section 1.6, have some limitations in terms of size and mechanical strength. For this reason, a novel superconducting magnet has been designed and developed, which provides the flexibility of size and can trap high magnetic fields. The new superconducting magnet reported in this work has significant potential to be used as trapped field magnet in motors and generator given the high trapped fields achieved experimentally.

An overview of the structure of the thesis is provided in the following section.

1.1 Thesis purpose and structure

This thesis focuses on the design and development of a new superconducting ring magnet. In this work, several magnets are created using 2G HTS tapes from different suppliers, and their behaviour and performance are evaluated in terms of trapped fields and field distribution. The new magnet is validated by experiments as well as by creating simulation models. A brief structure of the thesis is described below.

Chapter 1 is an introduction to superconductivity that also explains the fundamental theories related to the phenomenon of superconductivity. It also explains the other types of superconducting magnets.

Chapter 2 introduces the concept of superconductivity related to ring geometry and gives examples of superconducting ring applications.

Chapter 3 introduces and explains the H-formulation implementation of the ring magnet in both 2D and 3D. Comparison of both models is also conducted.

Chapter 4 explains the preparation of magnets and the structural configurations of different types of superconducting tapes used to created these magnets.

Chapter 5 introduces the experimental setup and compares the modelling and experiment results for all magnets.

Chapter 6 discusses in detail the 3D modelling results in detail in terms of current penetration and trapped field dependencies.

Chapter 7 explains the optimised ring magnet design created to improve the field distribution.

Chapter 8 concludes the thesis with related future work.

1.2 Superconductivity

Certain materials below their critical temperature T_c lose their electric resistivity; this phenomenon is superconductivity. This critical temperature is usually very low (close to absolute zero). Mercury was the first superconducting material discovered by the Dutch physicist Kamerlingh Onnes in 1911; this discovery was made possible during the liquification of helium gas at its boiling point of 4K [5]. The earliest superconductors were mostly metals and alloys. These metallic superconductors work at low temperature below 25K and require helium as a cryogen, and are thus termed as low-temperature superconductors (LTS). In 1986, Muller and Bednorz [6] discovered "cuprate" superconducting materials which operate at a critical temperature above 30 K and are named as high-temperature superconductors (HTS). A year later, in 1987, Yttrium Barium Copper oxide (YBaCuO) was discovered, which has a critical temperature higher than the boiling point of liquid nitrogen 77 K [7]. After that, superconducting materials have been classified into two categories:

Low-Temperature Superconductors (LTS) material: with a critical temperature lower than 30 K.

High-Temperature Superconductors (HTS) material: with a critical temperature higher than 30 K.

These discoveries open new applications for superconductors in electrical engineering such as high field magnets, as the power dissipation is negligible. Superconductors have two distinctive electromagnetic properties: their resistivity vanishes, and the magnetic field is forced out of the superconductors.

i. **Zero electrical resistivity:** A typical dependence of resistance on decreasing temperature of a superconductor compared to a normal conductor is shown below in Figure 1-1. In normal conductors, electrons are current carriers which collide with atoms. These collisions cause energy dissipation and create heat, which causes the electric resistivity in the normal conductor. By reducing the temperature, the thermal vibrations of the atoms reduce and electrons collisions also decreases, which in return reduces the resistivity of the conductor. The resistance of the pure metal reduces to zero as the temperature reduces towards absolute zero. However, practical metal contains some impurities which cause the scattering of electrons, which is independent of temperature. As a result, metals with impurities have some residual resistivity at absolute zero.

   In superconductors, their resistance reduces to zero when cooled down below the critical temperature. Above the critical temperature, the resistivity of superconductors is similar to that of normal metallic conductors. Zero resistivity of the superconductor is due to the formation of Cooper pairs, which is explained in section 1.4.3. At low temperature, the velocity of the Cooper pair is low, and there is insufficient energy to break the pairing. So the DC resistance of the superconductors is zero.

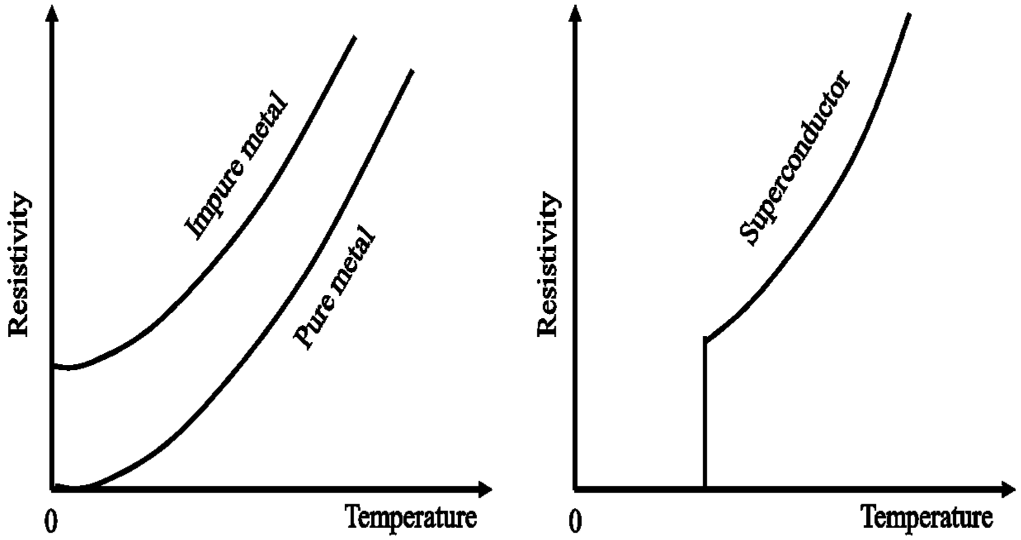

Figure 1-1. Resistance dependence on temperature of pure metal, metal with impurity, and superconductor. The resistivity of a pure metal increases with impurity [8]

ii. **The Meissner effect:** Meissner and Ochsenfeld investigated the magnetic properties of type I superconductors. They discovered that on cooling a superconductor in the presence of an external steady-state magnetic field H, at a critical temperature T_c the magnetic field lines are expelled from the interior of the superconductor. This type of magnetization is referred to as field cooling (FC). This explains how superconductor behaves like a perfect diamagnet. Diamagnetism is the property of a material which expels all the magnetic flux lines from the interior of the material. In contrast, a perfect conductor has no magnetic field expulsion at T_c because there is no time-varying magnetic field. During zero-field cooling (ZFC), in this process a superconductor is cooled in zero external magnetic fields H and subsequently, a magnetic field is applied. Both a perfect conductor and a superconductor will expel flux from the interior. Figure 1-2 explains the difference between the perfect conductor and the superconductor in terms of magnetic field and temperature during FC and ZFC magnetization.

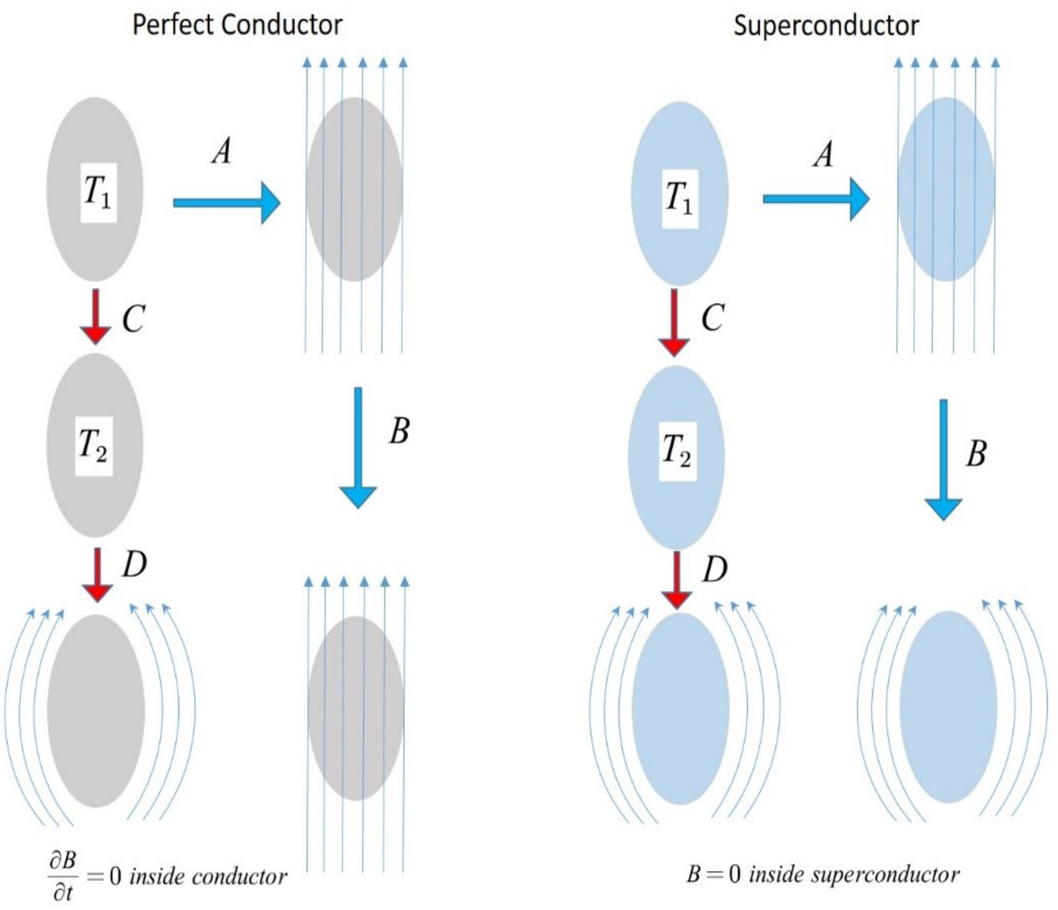

Figure 1-2. Meissner effect: This shows magnetic flux in a perfect conductor and a superconductor. When the temperature is above critical temperature T_1, the perfect conductor and superconductor show similar behaviour. During the C and D transition both show similar behaviour, while the A and B transition behaviours are entirely different. The transition C is zero-field cooling and B is field cooling. In both cases, the superconductor will show diamagnetic behaviour while a perfect conductor exhibits different behaviour. [9]

The relationship between the external magnetic field H, the magnetization of the superconducting material M and the total flux density inside volume of the superconductor is given as:

$$B = \mu_0 (H + M) \qquad 1\text{-}1$$

The Meissner effect typically occurs in type-I superconductors, which occurs when the external magnetic field is below the critical magnetic field H_c. This expulsion from the interior of the superconductor is due to the induced screening current on the surface of the superconductor. In this case:

$$M = -H \tag{1-2}$$

Therefore, the susceptibility is:

$$\chi = \frac{dB}{dH} = -1 \tag{1-3}$$

This effect results in a zero magnetic field B inside the superconductor. When the magnetic field H is greater than the critical magnetic field H_c, M drops to zero and the magnetic field fully penetrates the superconductor, i.e. $B = \mu_0 H$.

Superconductivity is defined by ideal conductivity $(\rho = 0)$ combined with ideal diamagnetism $(\chi = -1)$.

A superconductor's operating region is defined by three inter-related critical boundaries: critical temperature T_c, critical magnetic field H_c, and critical current density J_c. The superconductor will be superconducting within the critical limits of these parameters. The shaded portion in Figure 1-3 corresponds to the superconducting state of the material, which returns to the normal state at the moment any parameter exceeds the critical value. This explains two facts about superconductivity in perfect type I superconductors: superconductivity is a thermodynamic state, and there will be an induced magnetization when an external magnetic field is applied.

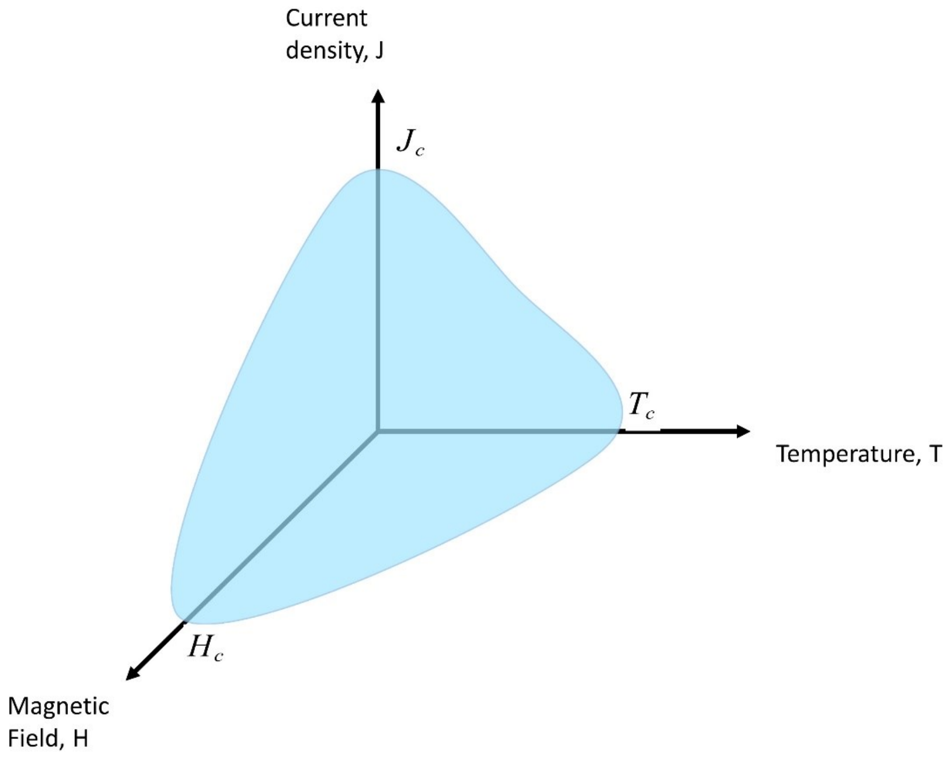

Figure 1-3. Critical surface of the superconductor in terms of critical temperature, critical current density and critical magnetic field. The superconducting state depends on three parameters having values below their critical state.

1.3 Superconductors: history and applications

In the beginning, the only critical temperature T_c was 4.2 K, but due to persistent efforts by researchers, superconductors with higher critical temperatures have been discovered. As already mentioned, many metals and alloys were found to be superconducting below 30 K, and these are named as low-temperature superconductors (LTS) materials. Low-temperature superconductors like Niobium-Titanium have been used as superconducting magnets since the 1960s. Later, in the 1980s, oxide-based ceramics showed superconductivity in the temperature range of 35 K, and were benchmarked to define high T_c superconductors. With improved extensive research around the globe, superconductors with the critical temperature of 135 K have already been discovered. A superconducting material whose critical temperature is below 30 K is known as a low-temperature superconductors, while materials above this critical temperature are high-temperature superconductors. Figure 1-4 shows the discovery history of different superconductors with their critical temperatures and the years in which they were discovered.

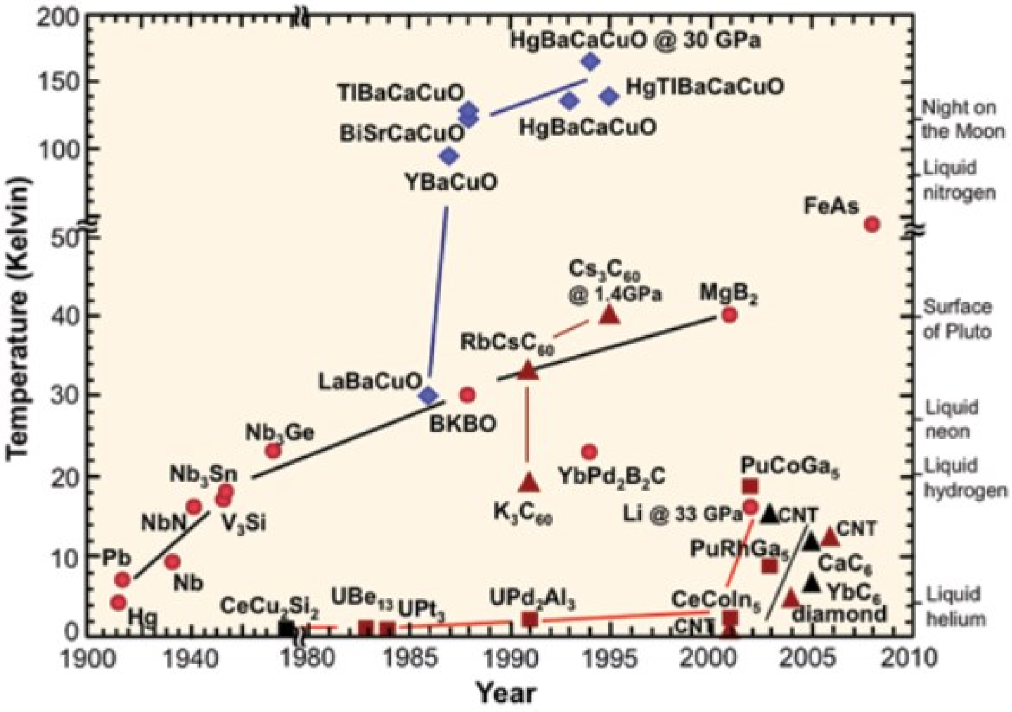

Figure 1-4. Superconductors with critical temperature and the year of discovery [10]

Low-temperature superconductors require expensive cryogenics systems. Most low-temperature superconductors use liquid helium as a coolant, which is very expensive. On the other hand, high-temperature superconductors made of copper oxides use less expensive liquid nitrogen coolant. The reduction in cooling cost makes high-temperature superconductors more promising for practical engineering applications.

In the present world, superconductors have made important contributions in major engineering fields. HTS materials such as YBCO have great potential for various fields. Major application categories of YBCO are bulk applications and films applications. Superconducting bulk and tapes applications are magnetic bearings [11], flywheels [12], electric machines [4], water purification by magnetic separation method [13], HTS maglev [14], HTS coils [15], fault current limiters [16], and cables [17]. Commercially two types of HTS wires are available: BSSCO wire [18] and YBCO wire [19], [20]. Figure 1-5 categorize some of the practical applications of superconductors. This thesis contributes towards the new HTS magnet, which has applications related to machines, magnetic separators, and maglev.

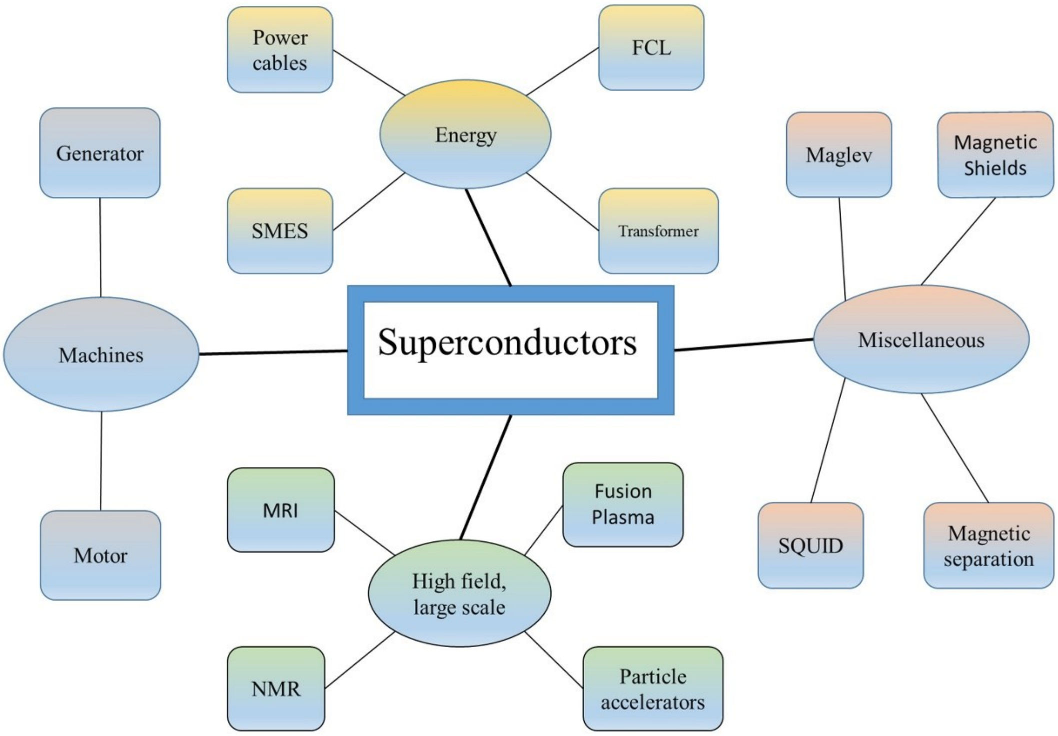

Figure 1-5. A few applications of superconductors. The most prominent and commercial application is the generation of high magnetic field densities. Superconducting magnets are becoming feasible for use in machines.

1.4 Microscopic theories of superconductivity

The definition of superconductivity, along with its history and applications, were discussed in sections 1.1. and 1.2. The following sections will discuss superconductors types and explain the theories vital for understanding the fundamental physics related to superconductivity.

1.4.1 Type I and type II superconductors

As discussed in section 1.2, to be a superconductor, the material should have a Meissner state. However, superconductors exhibit different behaviours with the increasing external magnetic field H. Superconductors can be divided into two types: type I and type II superconductors. Type I superconductors directly enter the normal state, while type II superconductors enter the mixed state before returning to normal states.

Figure 1-6 shows schematic phase diagrams of type-I and type-II superconductors (a) type-I and (b) type-II superconductors. The type-I superconductors are usually made from single metallic elements, and exhibit two properties in the superconducting state: perfect conductivity and perfect diamagnetism. They must expel all external magnetic field to stay superconducting, and this means they can be placed in magnetic fields of lower strength. Type-II superconductors are always alloys or compounds, and they can remain superconducting at higher magnetic field strength and current density levels.

Type I superconductors have a single critical magnetic field H_c. Once the external field increases beyond this magnetic field level, it changes from superconducting state to normal state, and the magnetic flux fully penetrates the superconductor. Type II superconductors have two critical magnetic field limits, the lower magnetic field H_{c1} and upper magnetic field H_{c2}. Between H_{c1} and H_{c2} lies the mixed state phase. When the magnetic field strength is below H_{c1}, it is superconducting with zero resistivity and magnetic field. H_{c1} for a type-II superconductor is equivalent to H_c for type-I superconductors. When the external magnetic field is between H_{c1} and H_{c2}, it allows some penetration of the magnetic field. In the mixed state, the magnetic field penetrates the superconductor through a series of flux vortexes that pass through the material. Section 1.4.5 explains this flux penetration in detail. Once this magnetic field strength exceeds H_{c2}, the superconductor becomes a normal conductor.

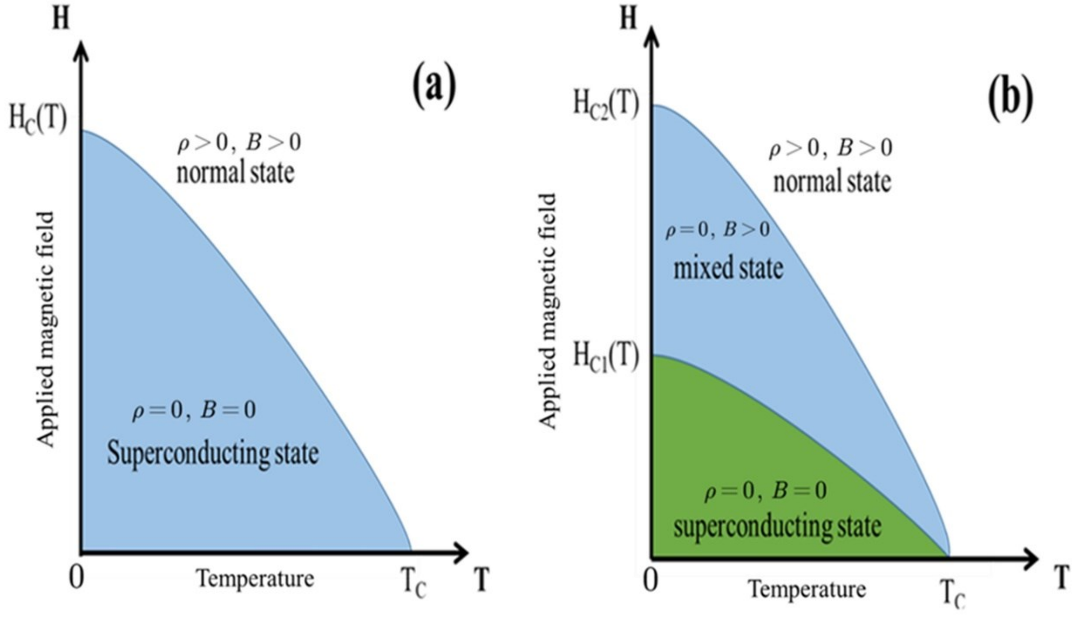

Figure 1-6. (a) The phase diagram for type I superconductors. The shaded part in blue colour is the Meissner state while outside this limit of the magnetic field vs temperature ($H - T$) curve it is the normal state. (b) The phase diagram of type-II superconductors, which have two critical fields H_{c1} and H_{c2}. Below H_{c1} is the superconducting Meissner state and above it up to H_{c2} is the mixed state. In mixed states, magnetic flux penetrates the superconductor in the forms of fluxons.

The critical field H_c for type-I superconductors is relatively low, i.e. 10-20 mT. This means that even a small self-field can destroy the superconducting state of type-I superconductors. For type-II superconductors, the high critical magnetic field H_{c2} can be very high such as for NbTi where it is 12 T, for Nb_3Sn it is 27 T, for MgB_2 it is 15 T, and for YBCO and Bi-2223 it is >100 T; all these values are at 4 K [21]. This indicates that type-II superconductors are promising for practical applications such as large magnets.

It is possible to differentiate between type-I and type-II superconductors by analysing the magnetization behaviour,. In this thesis, more importance is given to type-II superconductors. Fundamental physics related to superconductivity are discussed in the coming sections.

1.4.2 London equation

The London model is the mathematical explanation of the Meissner effect. The surface shielding current which creates the ideal diamagnetism in a superconductor has a finite depth penetration into the surface of a superconductor. The penetration depth λ is proportional to the super electron density n_s. Assuming the superconductor is an ideal conductor, in a frictionless environment the acceleration of the carrier in terms of an electric field E is:

$$m\overset{*}{u} = -Eq \qquad \text{1-4}$$

where m is the mass of the charge q and $\overset{*}{u}$ is the acceleration of the carrier obtained by the time derivation of velocity u. The current density can be expressed in terms of the density of super electrons as $J = -n_n q u$, so equation 1.4 can be written as:

$$E = -\frac{m\overset{*}{u}}{q} = \frac{m\overset{*}{J}}{n_s q^2} = \mu_0 \lambda^2 \overset{*}{J} \qquad \text{1-5}$$

where $\lambda^2 = m/\mu_0 n_s q^2$ and λ is the electrodynamic screening length. Taking the curl of both sides:

$$\nabla \times E = \mu_0 \lambda^2 \nabla \times \overset{*}{J} \qquad \text{1-6}$$

From Faraday's law of induction:

$\nabla \times E = -\overset{*}{B}$ and $\nabla \times B = \mu_0 J$. The term $B = -\mu_0 \lambda^2 \nabla \times J$ is the second London equation [22] and explains the Meissner effect in a superconductor:

$$\overset{*}{B} + \lambda^2 \nabla \times \nabla \times \overset{*}{B} = 0 \qquad \text{1-7}$$

By using the derivative property $\nabla \times \nabla \times B = \nabla(\nabla.B) - \nabla^2 B$ and $\nabla.B = 0$, equation 1.7 can be written as:

$$\lambda^2 \nabla^2 \overset{*}{B} = \overset{*}{B} \qquad \text{1-8}$$

whose solution after integration with zero constant gives the static magnetic field as B

$$B = B_a e^{\left(-\frac{x}{\lambda}\right)} \tag{1-9}$$

where $B_a = \mu_0 H$ and is the external applied magnetic field. Also, equation 1.7 can be solved for the screening current density J instead of the magnetic field B by using $\nabla \times E = -\overset{*}{B}$ and $\nabla \times A = B$ can be written as:

$$J = -\frac{A}{\mu_0 \lambda^2} = -\frac{n_s q^2}{m} A \tag{1-10}$$

A is the magnetic vector potential and λ is the London penetration depth.

$$\lambda = \sqrt{\frac{m}{\mu_0 n_s q^2}} \tag{1-11}$$

Equation 1.9, describes the Meissner effect: When a superconductor is placed in a static external magnetic field, a supercurrent arises in the surface layer with penetration depth λ , which creates an opposing field and cancels the external field inside the superconductor. The London equation gives an approximate description of the electrodynamic phenomenon. The next steps towards the explanation of superconductivity are the BCS theory and Ginzburg-Landau theory, which are explained in the next sections.

1.4.3 BCS theory

In 1957, a microscopic theory was proposed to numerically predict the properties of superconductors in terms of quantum mechanics, and named after Bardeen, Cooper, and Schrieffer (BCS) [23]. According to this theory, a single-electron in a cation lattice will create an area of greater positive charge density around it, which will attract another electron in the lattice and form the electron-phonon interaction. The supercurrent is carried by the formation of this electron-phonon interaction, which is called a Cooper pair.

This Cooper pair experiences less resistance in the lattice as the attraction between the partner electrons keeps them stable during the vibrations. So thermal vibrations have a negligible impact on the movement of the Cooper pair below the critical temperature. Figure 1-7 shows the Cooper pair in a cation lattice. The dependence of the energy gap at a specific temperature T and at the critical temperature T_c is correctly predicted by the BCS theory. It also predicts the Meissner effect. This theory only holds for low T_c superconductors and for elements and simple alloys; it cannot be applied to hight T_c superconductors. Also, it cannot derive sufficient information for a macroscopic model of superconductivity [24].

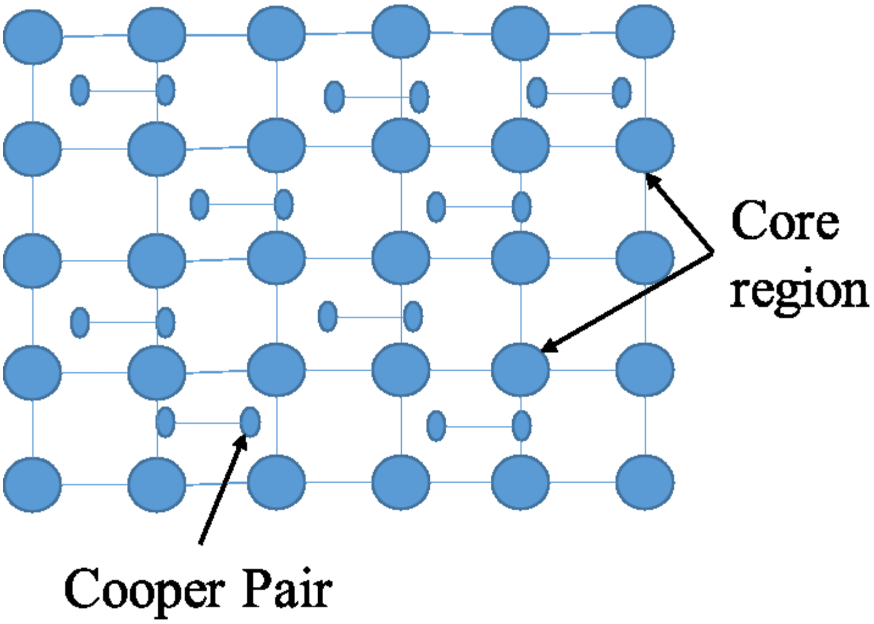

Figure 1-7. Cooper pairs carry the supercurrent relatively unresisted by thermal vibrations in a lattice.

1.4.4 Ginzburg-Landau (GL) theory

Ginzburg and Landau (1950) pointed out that the London phenomenological theory does not take into account two aspects. First, it does not consider the surface tension at the boundary between the normal and superconducting state. The surface energy connected with the field and super-current is positive, and is of non-magnetic origin and greater than the field distribution. Secondly, it does not take into account the destruction of superconductivity by current but considers it as a function of temperature only [25].

Ginzburg-Landau theory uses thermodynamic arguments and introduces the order parameter to predict the existence of the coherence length ξ and penetration depth λ. The theory starts with the expression of the wave function ψ for any order parameter, which is zero above the critical temperature T_c and increases gradually below the critical temperature T_c [26]. It can be written as a product of the phase factor term and modulus term as:

$$\psi = \sqrt{\frac{1}{2} n_s} e^{i\varphi} = |\psi| e^{i\varphi} \tag{1-12}$$

where n_s is super electron density, $|\psi| = \frac{1}{2} n_s$ and φ is the phase angle.

The Landau free energy density expansion is defined by quantum mechanics and can be summed up as the Ginzburg-Landau free energy density of the superconductor represented as a complex parameter:

$$F_s = F_n + \alpha |\psi|^2 + \frac{\beta}{2} |\psi|^4 + \frac{1}{2m} |(i\hbar\nabla - 2eA)\psi|^2 + \frac{1}{2\mu_0} B^2 \tag{1-13}$$

where α and β are temperature functions, A is the magnetic vector potential given as $B = \nabla \times A$, m is the mass, and e is the charge of a particle described by the wave function ψ. The term $(-i\hbar\nabla - 2eA)$ is defined as a momentum operator in a magnetic field B, and will be replaced by a vector G.

Any variations in parameter ψ and vector potential A should have the least impact on the free energy. The first GL equation can be derived by taking the variational derivative of F_s with respect to the free energy of ψ

$$GL - I\colon\ \alpha\psi + \beta |\psi|^2 \psi + \frac{1}{2m} G^2 \psi = 0 \tag{1-14}$$

which provides the relationship between the super electron density ψ and the magnetic field B. The second GL equation can be derived by taking the variational derivative of equation 1.13 with respect to magnetic vector potential A which gives the supercurrent density J by using the Maxwell equation:

$$GL-II\colon\ J=\frac{e}{m}\left[\psi^{*}(G)\psi\right]+c.c \qquad \text{1-15}$$

When no external field is applied, derivative of F_s with respect to ψ leads to a condition for equilibrium as:

$$\frac{\delta F_s}{\delta\psi}=0\rightarrow(\alpha+\beta\,|\,\psi\,|\,^{2})\ |\,\psi\,|=0 \qquad \text{1-16}$$

which means that the super electron density vanishes above T_c and gives one solution as $|\,\psi\,|=0$. The other solution is $\alpha+\beta\,|\,\psi\,|\,^{2}=0$, obtained by equating $\alpha(T)=\alpha_1(T-T_c)$, where α_1 is a constant:

$$|\,\psi\,|\,^{2}=n_s=-\left(\frac{\alpha}{\beta}\right)=-\frac{\alpha_1}{\beta}(T-T_c)$$
$$n_s\propto(T-T_c) \qquad \text{1-17}$$

Which means that the free energy related to super electron density n_s starts to increase at T_c, and as the temperature decreases further, this density increases. This explanation is for low T_c superconductors, while for high T_c superconductors the temperature dependency and material dependency in the GL equations should be taken into account in the form of coherence length ξ. It is derived by solving the differential equation F_s in the absence of the external field B, and ξ is defined as:

$$\xi=\left(\frac{\hbar^{2}}{2m\alpha(T)}\right)^{\frac{1}{2}} \qquad \text{1-18}$$

which has the units of length. This length is of vital importance in superconductors, and it is the total length of the wave function ψ stabilization. This length measures the scale over which the change from the normal to the superconducting state occurs at the boundary. It gives the penetration of the superconducting charge carrier density n_s into the superconductor. A comparison of penetration depth and coherence length explains type-I and type-II superconductors. A comparison of type I and type II superconductors in terms of coherence length and penetration depth is shown in Figure 1-8 . If $\lambda < \xi$, then the superconductor is type-I, whereas in the opposite condition the superconductor will be type-II.

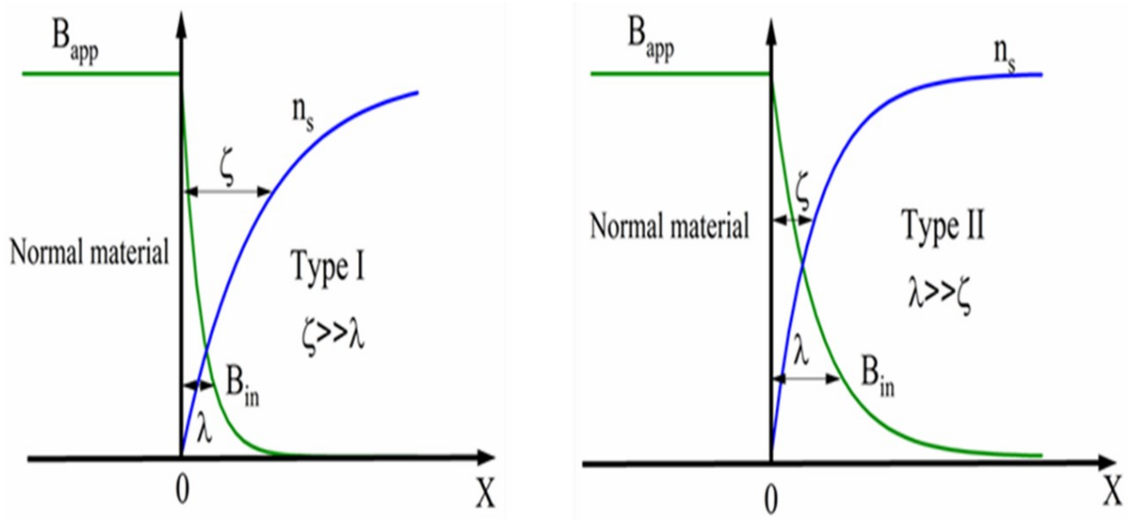

Figure 1-8. Comparison of type I and type II superconductors in terms of coherence length and penetration depth. The super electron density n_s distinguishes the superconducting state, which increases from zero at the interface deeper than the coherence length, this means that if λ is less than ξ , it is a type I superconductor. On the other hand, if the magnetic field penetrates to distance more than its coherence length into the sample so that $\lambda >> \xi$ it is a type II superconductors [27].

This ratio between penetration depth and coherence length is known as Ginzburg-Landau ratio $\mathcal{K}$

$$\mathcal{K} = \frac{\lambda}{\xi} \qquad \text{1-19}$$

This is an important parameter to distinguish between the types of superconductors. It is also not temperature-dependent, unlike λ and ξ . The ratio inequalities defining the types of superconductors are:

$$\begin{aligned} &Type\ I\colon\ \mathcal{K} < \frac{1}{\sqrt{2}} \\ &Type\ II\colon\ \mathcal{K} > \frac{1}{\sqrt{2}} \end{aligned} \qquad 1\text{-}20$$

1.4.5 Basic vortex dynamics

The Ginzburg-Landau theory also explains the concept of flux penetration in type-II superconductors. Flux penetration is due to discrete flux quanta $\Phi_0 = \frac{h}{2e}$ which occur in the form of a hexagonal lattice known as Abrikosov flux lattice [28] and is shown in Figure 1-9. Surrounding the core region (vortex) is a circulation current (vortex current) which shields the magnetic field. The magnetic field's peak value lies at the centre of the core region [27]. The Lorentz force due to the circulation current in the core region is transmitted to the whole vortex. Each core region interacts with the forces that are present between the lattices of the material. The movements of the vortices cause the vibrations which are the cause of thermal dissipations in type-II superconductors, unlike metals, where collisions of the electrons are the major cause of the thermal dissipation.

The circulation currents of neighbouring vortices interact with each other and creates repulsive forces. In the mixed state, these repulsive forces are equal to the magnetic stress and the vortex pattern formed due to these forces is known as the Abrikosov flux line lattice. According to Ampere's law, the macroscopic current is equal to the magnetic gradient inside the type-II superconductors. Type-II superconductors should have some impurities and crystalline defects so the vortices can be trapped to form a magnetic gradient. This phenomenon is known as "flux pinning", and the impurities or crystalline defects are named as "pinning centres" [29]. At vortex, the pinning force should be greater than the Lorentz force $f_p > f_l$ to avoid the movement of the vortex in the direction of the Lorentz force. "Flux pinning" is thus crucial for the practical application of type-II superconductors. However, there is still a possibility of a vortex to jump out of pinning potential due to thermal instabilities, which gives rise to the phenomenon of "flux creep". In a mixed state, the Lorentz force can exceed the pinning force and give rise to the movement known as "flux flow", which also causes the thermal dissipation.

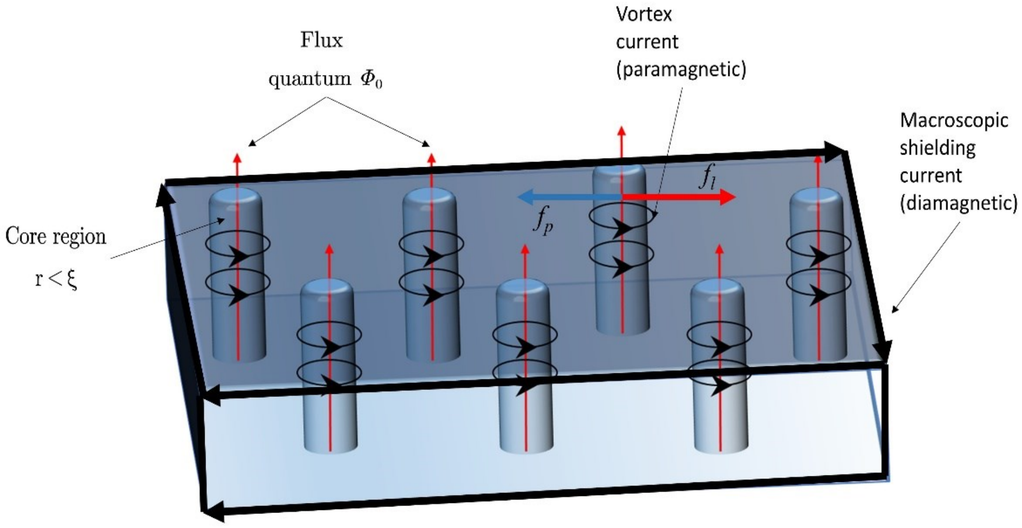

Figure 1-9. The external magnetic field penetrates the type II superconductor in the form of a flux lattice. Lorentz force f_l and pinning force f_p on the vortex in type II superconductors

1.5 Macroscopic theories for type-II superconductors

In type II superconductors, the magnetic field enters the superconductor in the form of vortices containing magnetic fluxoids. The movement of the vortices is the main cause of electromagnetic macroscopic behaviour in a mixed state. As already mentioned, these vortices in the form of the Abrikosov flux lines lattice enters the pure type II superconductor, which has no disturbance in background energy. Practical type II superconducting materials contain impurities and defects in their crystalline structures, which creates a disturbance in the background energy and vortices are pinned into positions which trap the potential. The pinning force is transmitted from vortex to vortex through interactive forces, and collectively they result in flux pinning.

Figure 1-10 shows the relationship between the microscopic and macroscopic electromagnetic theories of type-II superconductors. Flux line lattices and pinning forces are the main constituents of macroscopic theory for type II superconducting materials. Two models are used to explain this theory: the critical state model and the flux flow and creep model. For the flux creep and the flow model, the E-J power law has been derived.

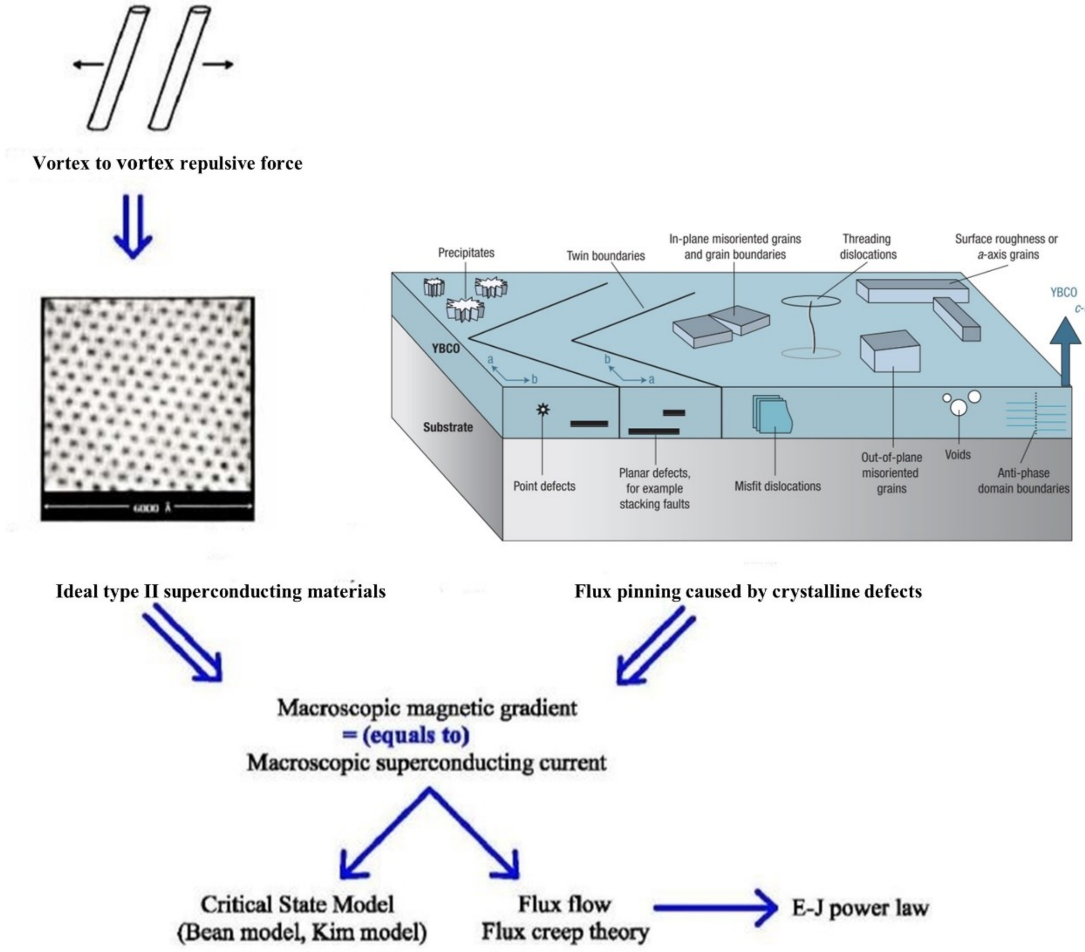

Figure 1-10. Relationship between the microscopic and macroscopic vortex dynamics of electromagnetic theories for a type II superconducting material in mixed state [30], Flux pinning [31], Ideal type II superconductors [29], [30].

This section discusses the macroscopic electromagnetic model for vortex dynamics, which will be followed by the critical state model and the E-J power law.

1.5.1 Critical state model

As the Meissner effect explained above describes how a type-I superconductor responds to the external magnetic field by expelling the magnetic field from the interior of the superconductor using a shielding current confined by the penetration depth λ from the surface, the critical state model explains how the shielding and flux penetration occur in the mixed state of type-II superconductors. The basis of the critical state model is flux pinning explained in section 1.4.5 In this model, the Maxwell relationship couples the supercurrent density and magnetic field as $\nabla \times B = \mu_0 J$, and they can be calculated by knowing any one of these values. Two general types of current are possible in a superconductor: transport current and magnetization current. Transport current is due to the action of an external voltage or current source, and the magnetization current is induced in the superconductor by the time-varying external magnetic field. Only magnetization current is relevant to this report so the critical state model will be explained in the context of this current.

The critical state model can further be classified into two models: the Bean model and the Kim model. In the Bean model, it is assumed that the amount of current flowing in a superconductor is always equal to the constant current density J_c. On the other hand, Kim model considers the field dependence of the critical current density $J_c(B)$. Bean model can only be used to predict the magnetization of regular shaped hard superconductors, while the Kim model is more general in its prediction of magnetization.

1.5.1.1 Bean Model

The Bean model is the simplest form of critical state model which states that the magnitude of the critical current density in an area of superconductor which experiences flux flow can take only three values: either $0 \ or \ \pm J_c$ [32]. The induced current will be equal to the full critical current density value when even a small electromotive force is applied across the superconductor in a mixed state. Also, the current density will be zero only for regions which never experienced the magnetic field. When the whole superconducting sample is penetrated by $\pm J_c$ it is said to be in a critical state. The Bean model is usually applied to estimate the magnetization of a superconductor during zero-field cooling and field cooling processes. A slab of infinite length and width with no demagnetization effects makes ideal geometry for Bean model implementation. Fig 1.11 shows the Bean model penetration of the magnetic field during the zero-field and field cooling methods. During zero-field cooling as shown in Figure 1-11 (a) the superconductor is cooled down below the critical temperature, and then the magnetic field is applied. During every cycle, the induced magnetic field increases until it completely saturates the sample. If the superconducting sample can trap H_p at the centre, then the applied field required in ZFC is $2H_p$ to fully penetrate the sample. During field cooling as shown in Figure 1-11 (b), the applied field needed to fully penetrate superconductor is equal to the final trapped field of the sample i.e. $H_a = H_p$.

(a) Zero-field cooling

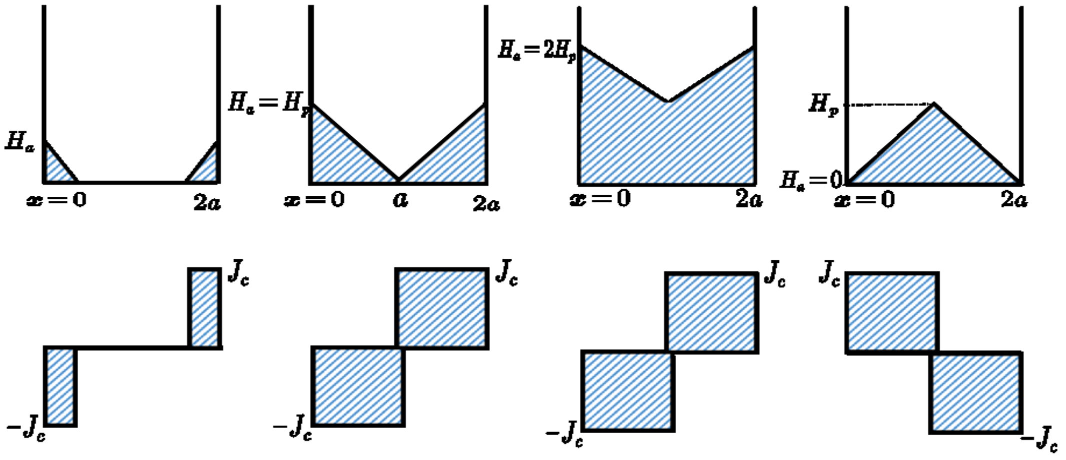

(b) Field cooling

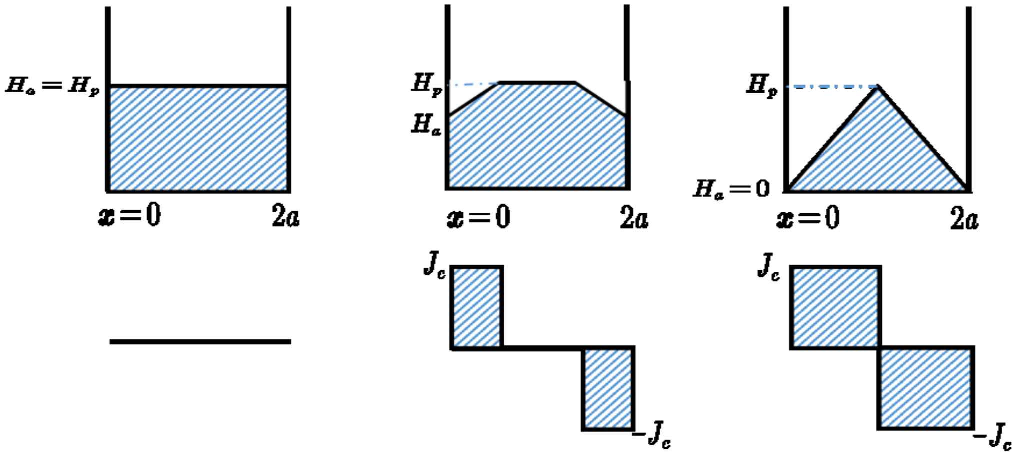

Figure 1-11. Bean model magnetization of a hard superconductor during zero-field cooling and the field cooling method

1.5.1.2 Kim model

This model is a more realistic approach in defining the magnetization of a type-II superconductor. It states that J_c is dependent on the magnetic flux density [33] instead of having a constant value as defined by the Bean model. As in type II superconductors, the pinning force at a specific temperature is fixed, and the only impact of an increase in the magnetic field is the increase in the Lorentz force which leads to smaller critical current density. The relationhip between the magnetic field, Lorentz force and critical current density is expressed as [26]:

$$f_l = J \times B \Longrightarrow J = \frac{f_l}{B} \qquad 1\text{-}21$$

The most common form is explained by the Kim model and is given as [34][35]

$$J_c(B) = \frac{J_{c0}}{1+\frac{B}{B_0}} \qquad 1\text{-}22$$

Table 1-1 below gives the critical current and magnetic field relationships for several critical state models [27]:

Table 1-1. Current-field relationships for different critical state models

Relationhip	**Model**
$J(B) = J_c$	Bean
$J(B) = \frac{J_c}{\frac{B}{B_0}}$	Fixed pinning
$J(B) = \frac{J_c}{\sqrt{\frac{B}{B_0}}}$	Square root
$J(B) = \frac{J_c}{1+\frac{B}{B_0}}$	Kim
$J(B) = \frac{J_c}{1+\left[\frac{B}{B_0}\right]^2}$	Quadratic
$J(B) = \frac{J_c}{\left[1+\frac{B}{B_0}\right]^\beta}$	Generalized

1.5.2 Superconductor Magnetization Hysteresis

The magnetization of a superconductor is fundamentally different from the magnetization of ferromagnetic material. In superconductors, magnetization is due to macroscopic current flowing in the interior of a superconductor, while in ferromagnetic material it has a local value at any point throughout the material. The most important parameter for superconductor applications is the critical current density J_c . It determines the diamagnetic response of the superconductor. The critical current density J_c can be estimated from the magnetic measurement from the Bean model formula using the critical state model:

$$J_c = \frac{3\triangle M}{2R} \qquad 1\text{-}23$$

In the above formula, $\triangle M$ is the hysteresis width, and R is the radius of the current circulation [36].

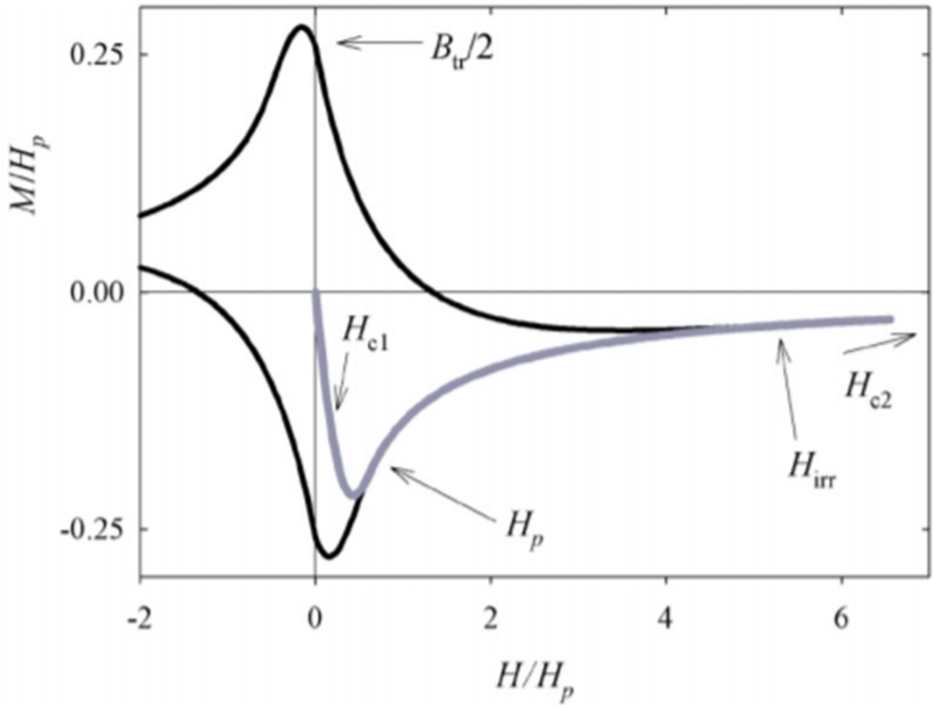

Figure 1-12. Characteristic field on magnetization hysteresis of superconductor. The H_{c2} field is larger than the maximal external field [36]

The parameters describing type-II superconductors are: lower critical field H_{c1}, upper critical field H_{c2}, the full penetration field H_p, the irreversibility field H_{irr}, the trapped flux B_{tr}, the equilibrium layer depth l_s, and the critical current density J_c which is analysed by magnetization hysteresis. The main stages of magnetization hysteresis are shown in Figure 1-12 and summarised as:

1. The dependence of magnetization M on the magnetic field H in the superconducting phase approaches zero as the magnetic field H approaches the upper limit H_{c2}.
2. At H_{c1}, the $M(H)$ dependence begins to deflect from the linear line and coincides with the magnetization loop when the magnetic field H is equal to the full penetration field H_p, as illustrated by the grey line in Figure 1-12. At this point, the $M(H)$ dependence becomes reversible at a magnetic field H greater than the irreversibility field H_{irr}. At H_{c2}, the superconductivity and diamagnetism disappear and field H_{tr} becomes trapped in the magnet which is equal to $\mu_0 \triangle M$ at zero magnetic field H.
3. The reversible part of the magnetization hysteresis gives the estimated magnetic field penetration λ_0.
4. The hysteresis asymmetry relative to $M = 0$ depends on the radius of the circulating current R and is independent of the critical current density J_c. This asymmetry is the ratio of the surface layer depth l_s and current circulation radius R. The vortices are not pinned in the surface layer. The surface layer depth l_s is less than the field penetration λ_0. Asymmetry in magnetization hysteresis is observed when $R < 10\lambda$.
5. The Bean model can be used to plot the averaged critical current densities J_c dependencies on the cross-sectional perpendicular external magnetic field H. The maximal pinning field and irreversibility field can be determined from the field dependence of the pinning force. Vortex lattice transition and phase separation

information can be deduced from the peak position and its temperature evolution from the magnetization hysteresis and the on-field dependencies of the critical current densities and pinning forces [37].

1.5.3 Flux creep, flow and *E*-*J* power law

The critical state model does not take into account the effect of flux creep. In the critical state model, the flux lines lattice (FLL) is considered independent of thermal disturbances and considered to be stable. In reality, this is not true as the temperature is above 0 K, and for type II where the operating temperature is 77 K, the magnetic relaxation comes into play known as flux creep [38].

Figure 1-13 shows a graph between the measured values of current density J and electric field E in the presence of an external magnetic field. Three different parts of the curve are labelled as "TAFF", which stands for thermally assisted flux flow, flux creep and flux flow. TAFF is experienced in the low current; flux flow is the high current region, and flux creep is the transition region between the two. This explains why there is no hard and fast rule to define I_c, but it is related to the measurement of current at the electric field $E = 1\mu V/cm$.

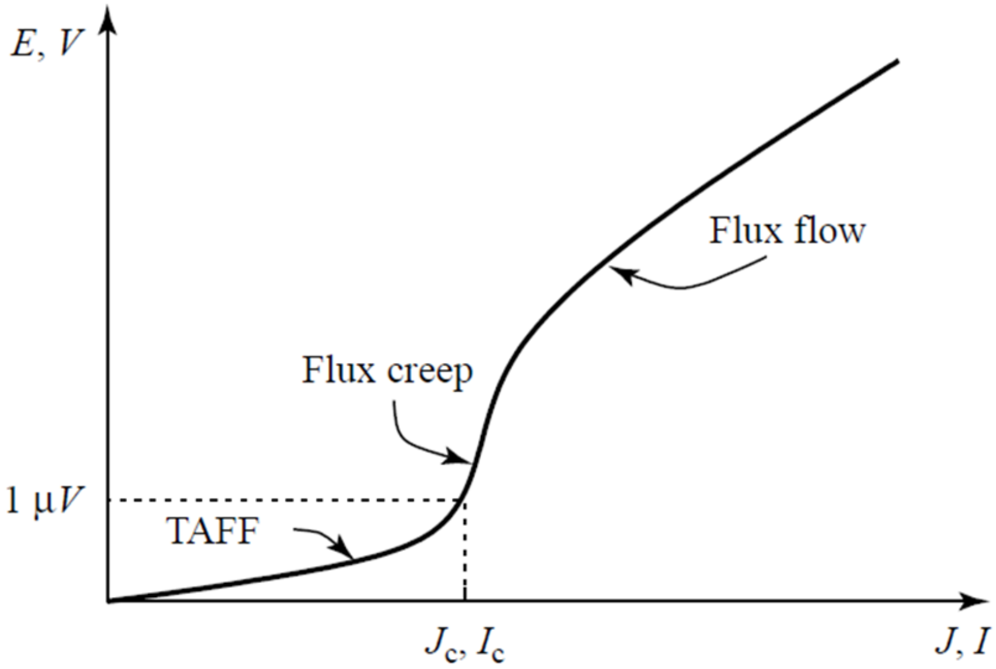

Figure 1-13. Defining I_c or J_c by transport measurement. The curve has three regions: linear, nonlinear, and finally linear again. Effective resistance in the two regions has ohmic behaviour. This plot is read as $E-J$ characteristics. [26] page 204.

Flux flow is related to high currents which tear loose the flux lattice and set the lattice in motion. Flux flow theory is widely accepted and was given by Bardeen and Stephen [39]. In this theory, the vortex core is in a normal state, and its radius is equal to the coherence length ξ . The transport current will set the vortex in linear motion due to this electric field which is generated in the surrounding region. This is only possible if $f_l > f_p$ and the vortex velocity is given by force balancing in the surrounding medium, which is dependent on the current density and magnetic field:

$$v = \frac{1}{\eta}\Phi_0 J \qquad \text{1-24}$$

Multiplying the above equation by the magnetic field gives the electric field:

$$E = Bv = \frac{B}{\eta}\Phi_0 J = \rho_{ff} J \qquad \text{1-25}$$

So, the electric field induced by flux flow is given by:

$$E = E_c + \rho_{ff} J_c \left(\frac{J}{J_c} - 1 \right) \qquad 1\text{-}26$$

which gives the flux flow resistivity:

$$\rho_{ff} = \frac{1}{\eta} B \Phi_0 \qquad 1\text{-}27$$

As already mentioned, some of the vortices jump out of the lattice due to thermal forces even after pinning, and the movement of jumped out vortices is named flux creep. This flux creep concept is explained by Anderson's flux creep model [40], and the rate of jumping out pinning centres is described by the Arrhenius equation, which is determined by the Boltzmann factor [41]:

$$R = v_0 e^{\frac{-U}{kT}} \qquad 1\text{-}28$$

where R is the escape rate, v_0 is the microscopic escape frequency of the order $10^{-8} - 10^{-10}\ s^{-1}$, U is the height of the barriers, also known as the pinning potential, k is the Boltzmann constant, and T is the absolute temperature. With the increasing critical current density J_c, the height of the potential barrier decreases as shown in Figure 1-14, which can be expressed as:

$$U = U_0 \left(1 \pm \frac{J}{J_c} \right) \qquad 1\text{-}29$$

where J_c is the critical current density which is equal to the gradient of the potential barrier with respect to distance x dU/dx. The $E - J$ relationship of flux creep is derived by substituting Eq. 1.31 into Eq. 1.30 and multiplying it by B, which gives:

$$\begin{aligned} E = Bv &= Bv_0 l \left\{ e^{-\frac{U_0(1 - J/J_c)}{kT}} - e^{-\frac{U_0(1 + J/J_c)}{kT}} \right\} \\ &= \rho_c J_c \sinh\left(\frac{U_0 J}{kT J_c} \right) e^{\left(-\frac{U_0}{kT} \right)} \end{aligned} \qquad 1\text{-}30$$

where $\rho_c = Bv_0 l / J_c$ is the flux creep resistivity.

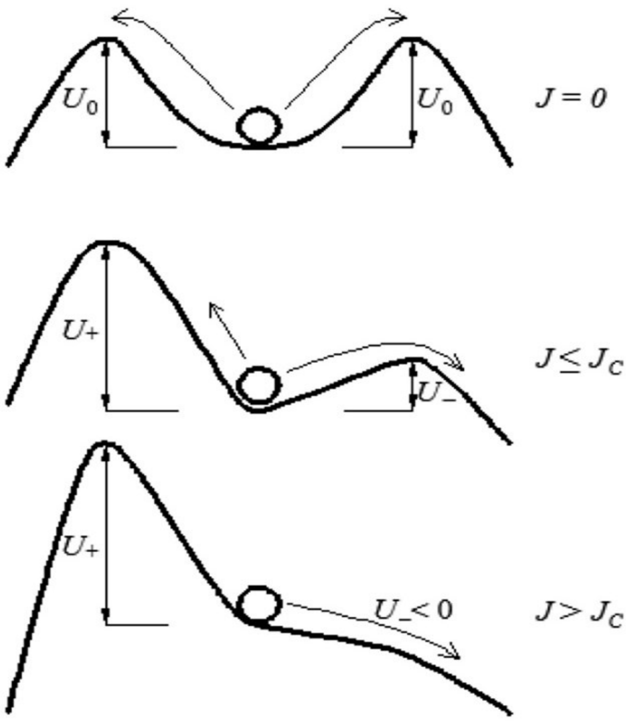

Figure 1-14. Energy landscape of pinned flux lines in the uniform external current [26]

By combing the electric field equations obtained for flux flow (1.28) and flux creep (1.32), we have the $E-J$ characteristics of type II superconductors. For practical application, the more commonly known $E-J$ power law is used, which is derived by using the four-point probe method [42] for transport current measurement. The $E-J$ power-law used for modelling is [43]:

$$E = E_0\left(\frac{J}{J_c}\right)^n \qquad \text{1-31}$$

where $E_0 = 10^{-4} V/m$ is the criterium used to determine experimentally the critical current density by using the four-point measurement method: $n = U/kT$ determines the stiffness of the $E-J$ curve.

1.6 Superconducting permanent magnets

Superconductors can transport high currents with minimum losses, which makes them an ideal selection for high field magnets. Superconductors for a practical application can be categorised in three broad forms: wires and tapes, thin films, and bulks. The rare earth element class of superconductors are mostly used in practical applications. The chemical formula is $(RE)Ba_2Cu_3O_{7-x}$, where RE stands for rare earth element and more simply it is written as $(RE)BCO$. YBCO is the most widely used superconductor belonging to this class. GdBCO is popular because of its high critical current density at 77 K. When compared to conventional magnets which can only provide a magnetic field in the range of 1.5-2 T, the superconducting magnet are attractive for a number of practical applications which rely on their high magnetic field. The National High Magnetic Field Lab (NHMFL) in the USA has already achieved a 45 T field using a resistive-HTS hybrid magnet [44].

1.6.1 Bulk Superconducting magnet

A (RE)BCO bulk can sustain a high persistent current after magnetization which can act as a quasi-permanent magnet to provide a higher magnetic field of several teslas with a small volume of material. A record trapped field of 17.6 T at 26 K in a stack of two silver-doped GdBCO superconducting bulk samples fabricated by the top-seeded melt growth method has been reported by the Bulk superconductivity group, University of Cambridge [45], which makes a new world record by leapfrogging the previous record of 17.24 T at 29 K [46]. The trapped field of the superconducting magnet is proportional to the volume of the superconductor and the critical current density J_c [47], [48]. The YBCO anisotropic behaviour of superconducting and thermal properties is due to its anisotropic crystalline structure, as shown in Figure 1-15.

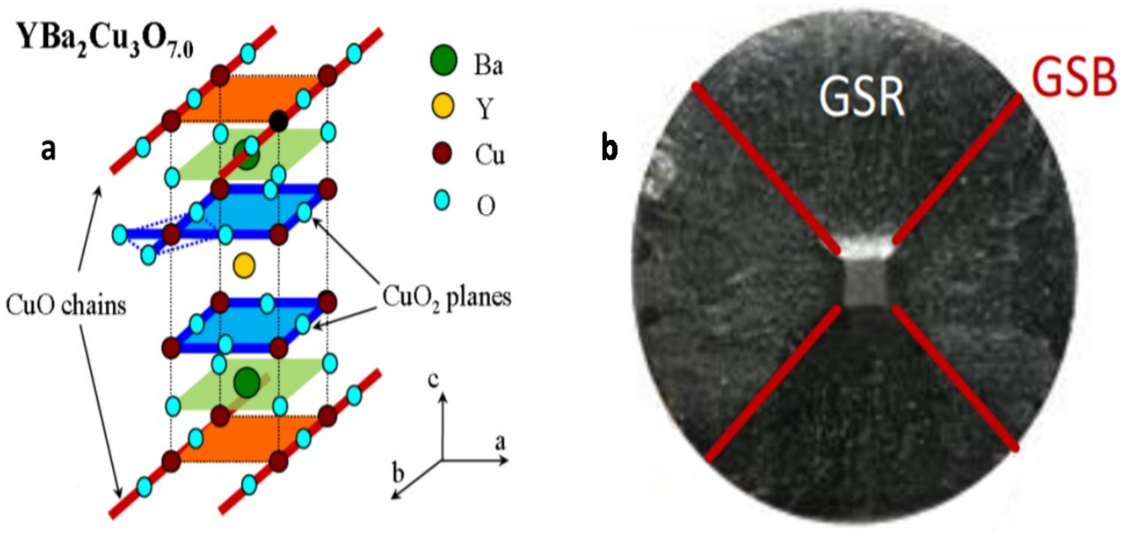

Figure 1-15. (a) The crystalline structure of YBCO. The CuO chains are responsible for carrying current, which gives a higher critical current density J_c than the current along the c-axis.[49], [50] (b) The view of the bulk superconductor fabricated by top-seeded melt growth showing the growth sector region (GSR) and boundaries (GSB) having different J_c [51].

The J_c performance of a YBCO bulk is enhanced in the form of a large single grain, as it reduces the presence of misoriented grain boundaries which are the main cause of poor macroscopic J_c. A large grain bulk is produced by top-seeded melt growth, which is done by placing a small seed crystal of similar lattice parameter and high melting point on top of a pre-sintered YBCO pellet. It is done by increasing the temperature high enough, which melts the YBCO to nucleate around the seed, which forms the single domain during cooling [48]. To enhance the critical current and homogeneity over its length, the flux pinning performance and size of a single domain can be maximised by applying seeded melt growth. To reduce the formation of microcracks which impede the current flow, an array of holes parallel to the c-axis are fabricated within a single domain YBCO bulk, which improves the oxygenation and has been proven successfully for trapping magnetic fields [52], [53]. Although, REBCO bulk superconductors are widely used, their limitations: they are expensive and time-consuming to produce with brittle mechanical properties, low thermal conductivity, and cannot have larger diameter: the maximum diameter available is 60 mm. Also, the critical current density in terms of temperature and magnetic field varies significantly with axial and transverse distance from the seed crystal [54]. The trapped field on the top side of the bulk is greater than the trapped field on the bottom side due to the higher critical current J_c near the seed crystal [55]. In addition, the critical current density J_c is higher at the growth sector boundaries than in the growth sector regions [51], which causes inhomogeneities in the trapped field and contributes towards the pyramidal trapped fields [56]. To overcome the inhomogeneities of superconducting bulk properties, rings of varying diameter are re-assembled from a single bulk to misalign the growth sector boundaries [57]. The trapped field of the bulk depends on the temperature and is limited by three factors: J_c, tensile strength, and magneto-thermal instabilities [58]. For trapping a higher field in bulk superconductors, external reinforcement is required to counter the tensile strength limits.

1.6.2 Coated conductor superconducting magnet

Another major form in which (RE)BCO is used is as a coated conductor superconductor. It is created by depositing the (RE)BCO superconductor as a thin film on a metallic tape substrate. In the case of a bulk, the template of the crystallographic texture is instigated by epitaxial growth into the growing (RE)BCO material which makes a localised seed crystal. In the case of a coated conductor, a metallic substrate or an oxide film will act as a template, and the buffer layers act as a medium between the texture and the (RE)BCO film. Even the thickness of the superconducting material is in microns, but the critical current J_c of (RE)BCO layer is greater than in bulks. The mechanical stability given to the thin and brittle (RE)BCO layer is provided by Hastelloy or Ni-W substrate, while in the normal state of (RE)BCO layer the current flows in the silver overlayer. Many applications require further stabilization which is provided from copper layers. Details are discussed in chapter 4.

The ability of the coated conductors to sustain persistent current means they can be used as trapped field magnets. Below 77 K, superconducting bulks experience thermal instabilities and non-uniform distribution of critical current density. In contrast, a stack of coated conductors has a uniform current density in both the radial and axial directions and does not suffer from thermal instabilities [59]. Also, for high trapped fields, a bulk requires external enforcement to compensate for the tensile stress, but in coated conductors, the Hastelloy provides sufficient tensile stress to support the high trapped field. Finally, the size of the bulk is limited compared to the superconducting tapes where the metal substrate replaces the seed crystals to provide the texture of the (RE)BCO film. The critical current distribution of the (RE)BCO tape is uniform, while for bulk, it is at a maximum near the seed crystal, which forms the centre [60]. Also, the trapped magnetic field increases monotonically by increasing the number of tape in a stack [61]. The trapped field in a stack of tapes is independent of the thickness of the stabilizer [62]. Figure 1-16 shows stacks in different shapes already proposed.

Figure 1-16. HTS tapes pieces and stacks in different shapes and sizes to form composite bulk that has already been produced [63].

A trapped field of 7.9 T at 4.2 K was achieved in a double stack of GdBCO tapes, each having 130 layers [64]. In a stack of a coated conductor, the trapped field only depends on the critical current unlike a superconducting bulk, where it also depends on the mechanical properties and the flux jumps at lower temperatures [65]. The strongest permanent magnet created up till now uses a stacked coated conductor and trapped a field of 17.7 T at 8 K without any external reinforcement [63].

The advantages of the stacked coated conductor can be summarised as: these stacks of tapes have flexible geometry, high tensile strength which requires no external mechanical reinforcement to counter the Lorentz force, uniform superconducting properties throughout the volume, and good thermal stability due to the silver stabilizer layer. The only limitation related to magnets created from a stack of tapes is the size which is limited by the width of the tape. The superconducting tape 46 mm wide produced by AMSC

(American Superconductor) is the maximum width of the available tapes. So both bulk and stack magnets have a size limitation, which is countered in this thesis by creating a new ring magnet as will be discussed in the coming chapters.

1.7 Conclusion

This chapter explains the phenomenon of superconductivity along the theories related to electromagnetism for type I and type II superconductors. Superconductivity is ideal diamagnetism. However, a superconductor itself is much more complex and different theories have tried to explain the phenomenon. The basic is the Meissner effect and the London equation, which explains type I superconductors. For understanding the mixed state of type II superconductors the Ginzburg-Landau theory is explained, and further expanded to explain basic vortex dynamics. Critical state models such as the Beam model and the Kim model are also introduced and concepts related to flux creep and flux flow are introduced to drive electric field equation which was used to drive the $E - J$ power equation. This chapter provides the basic knowledge of superconductivity concepts relating to two types of superconductors. Types of superconducting magnets along with their advantages and disadvantages are also explained. The new type of magnet which counters the disadvantages of bulk and stack magnets will be discussed in the coming chapters.

2 INTRODUCTION TO SUPERCONDUCTING RING MAGNETS

This chapter discusses the superconductivity theory related to ring shape superconductors. Theories related to field penetration in superconducting rings are also discussed. This chapter explains how the magnetic flux penetrates the ring geometry. The impact of length and diameter on the induced magnetic field in a superconducting ring magnet is discussed. Also, work related to superconducting rings is presented which explains how these superconducting rings can act as persistent current loops. The contribution of this thesis to the creation of superconducting magnets is also discussed.

2.1 Persistent current in a superconducting ring

When a superconducting ring is placed in a perpendicular changing external field, and the temperature is below its critical temperature, a current is induced according to the Faraday-Lenz law. Below the critical temperature its resistivity becomes zero, so the induced current will remain unchanged after the removal of the external field. This induced current will remain in the superconducting ring and will be termed as persistent current. This circulating current in the superconducting ring will produce a magnetic field which will remain constant below the critical temperature.

According to Faraday's Law:

$$L\frac{di}{dt} = -A\frac{d(\phi_{ext} - \phi_{ind})}{dt} \qquad 2\text{-}1$$

The negative sign explains the direction of the induced current, which follows the Lenz's Law. Here L is the inductance, A is the area, and B is the magnetic field. Initially the induced current is zero, so the induced magnetic field will be zero as well.

$$L\frac{di}{dt} = -A\frac{d\phi_{ext}}{dt} \qquad 2\text{-}2$$

Integrating both sides gives $LI = -\phi A$

$$LI + \phi A = cons\tan t \qquad 2\text{-}3$$

where LI is the amount of flux ϕ through the ring generated by the current I.

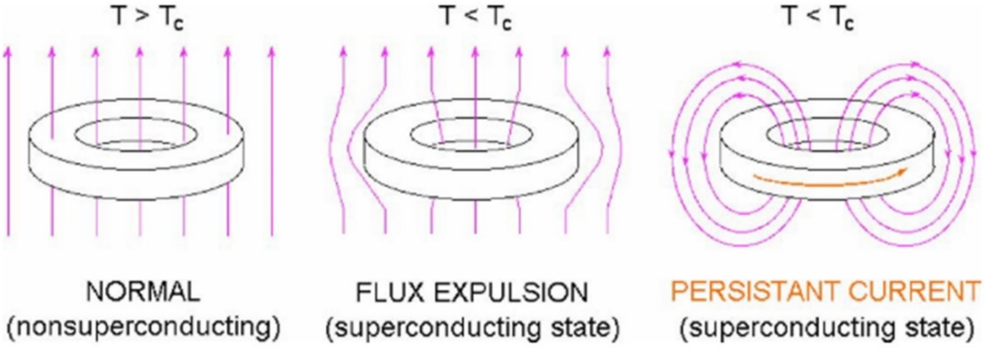

Figure 2-1. Explanation of flux penetration in a superconducting ring when subjected to cooling and changing the perpendicular external field [66].

Figure 2-1 explains the penetration of magnetic flux in the superconducting ring. The external magnetic field passes through the superconducting material when it is in normal state. On decreasing the temperature below the critical temperature of the superconductor and by changing the external field, a current will be induced to compensate for the changes in the magnetic field within the conductor. During this superconducting state, the magnetic flux lines will be expelled from the superconducting material but will pass through the hole and surroundings of the superconducting ring. The superconducting ring will trap the interior flux instead of expelling it, which is opposite to the case of continuous solid. Now if the external magnetic field is removed completely, the current circulate within the superconducting ring which will keep the magnetic flux of the ring constant. As the resistance of the superconducting ring is zero, the current will not decay, and a persistent current will flow in the superconducting ring if the temperature is kept below its critical temperature. In type II superconductors, there is complete flux expulsion below $H_{c1}(T)$ but partial expulsion between $H_{c1}(T)$ and $H_{c2}(T)$.

2.2 Impact of superconductor ring geometry

As already discussed in the literature, the macroscopic properties of type II superconductors are dependent on critical current densities J_c , obtained from experimental magnetization by using the Bean critical state model. The critical current density J_c and magnetization data are geometry dependent. To determine the critical current density J_c in the magnetic field, an important parameter is the penetration field H_{pen}. It is the minimum applied field which fully penetrates the type II superconductor. It can be related to the critical current density and the geometry of the sample as:

$$H_{pen} = J_c f(\Omega) \qquad 2\text{-}4$$

$f(\Omega)$ represents the geometry function [67] which can be found in theory once J_c is calculated by taking measurements using a Hall probe. The superconductor geometry plays an important role in practical applications such as magnetic bearings [68] and permanent magnets [46]. The ring geometry due to hole presents some different properties from a bulk and stacks of bulks, but maintains the cylindrical symmetry. Ring geometries for bulks have been studied for grain boundaries [69], [70]. Compared to cylindrical bulk superconductors, the ratio of weight to trapped magnetic flux is lower for ring shape geometries [71]. As noted, in case of bulks, there are mechanical problems which increase the stress in the middle; this problem can be avoided in superconducting rings as there is no central part [72].

2.2.1 Current and field penetration in rings

Current and magnetic field penetration in a type-II superconducting ring depends on its length L and diameter R. In rings, there are two radii: the inner radius R_{in} and the outer radius R_{out}. When the superconducting ring is placed in a uniform external field whose value is much greater than the lower critical field H_{c1} of a type II superconductor, the current will be induced in the superconductor. The current will flow in an angular direction due to the cylindrical symmetry. During zero-field cooling, following the critical state model, the current induced $I_{ind} = J_c(R)\,(L)$ decreases the magnetic energy during each cycle of increasing external field until it becomes impossible for further reduction of a magnetic energy, and the current becomes saturated.

In case of an infinite superconducting ring, the external field is shielded in the interior of rings as well as in the middle hole due to induced current. However, in case of a finite superconductor ring, the field in the hole is not zero and the shielding impact of the induced current is only limited to the volume of the superconductor. Due to the hole in the middle, the current penetrates from both inner and outer sides of the ring as the flux lines are not zero in the middle. For a fixed length L, the inner radius R_{in} determines the penetration field for current saturation.

As the current penetrates the rings from the outer surface as well as from the inner surface, it is impossible to predict the last penetration place in the superconducting ring. However, an energy minimization procedure can predict the last place of current penetration in the superconductor ring. The full penetration field depends on the length of the ring. For larger rings, a higher penetration field is required to saturate the superconducting ring. So the penetration field for a specific length and diameter can be generalised as [67] where the length is normalized with respect to R_{out} and the magnetic quantities by $H_{pen}(\gamma \to \infty, \delta = 0) = J_c R_{out} = H_{pen}^{\infty - bilk}$ which is the full penetration field of the infinitely long bulk cylinder, which means for an infinitely long bulk, an internal hole of zero means that $R_{in} = 0$

$$\frac{H_{pen}(\gamma,\delta)}{H_{pen}^{\infty - bulk}} = \frac{\gamma(1-\delta)}{2(1+\delta)} \ln\left(\frac{2(1+\delta)}{\gamma} + \left\{1 + \left[\frac{2(1+\delta)}{\gamma}\right]^2\right\}^{\frac{1}{2}}\right) \qquad 2\text{-}5$$

where $\delta = \frac{R_{in}}{R_{out}}$ and $\gamma = \frac{L}{R_{out}}$. This gives a dimensionless result rather than in units of J_c, R_{in} and R_{out}. For an infinite ring, the penetration field reduces to:

$$\frac{H_{pen}^{\infty ring}}{H_{pen}^{\infty - bulk}} = 1 - \delta \qquad 2\text{-}6$$

For very thin ring full penetration field approximation is given as [73]:

$$\frac{H_{pen}^{thin-ring}}{H_{pen}^{\infty-bulk}}=\gamma\left(\frac{2(1-\delta)}{\pi(1+\delta)}\left\{\ln\left[\frac{8(1+\delta)}{(1-\delta)}\right]-1\right\}-\frac{1}{2}(\ln\delta+1-\delta)\right) \qquad 2\text{-}7$$

The induced current is averaged across the length. It gives full penetration field for the larger outer radius. Figure 2-2 shows the calculated penetration field for different δ values as a function of γ. As the length of the ring increases while the radius is kept constant, a greater external magnetic field is required to fully penetrate the superconducting ring. When the length is kept constant, the increase in radius decreases the external field for full penetration.

When the current fully penetrates the superconductor, the corresponding magnetic field is the total trapped field of the rings. The trapped field in the middle is independent of the length and only depends on the inner radius of the ring. Increasing the inner radius decreases the trapped field, and a decrease in the inner radius increases the trapped saturation field. The saturated magnetization of a ring is always greater than that of a cylinder bulk for the same length. The experimental proof for magnetic susceptibility concludes that the parameter of D/w differentiates between the disk and the ring [73].

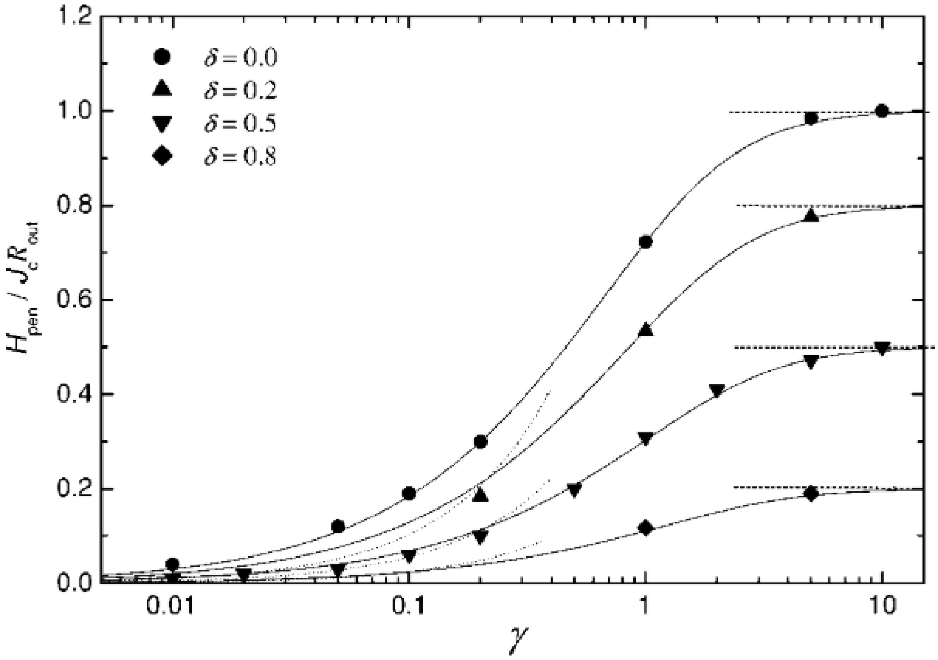

Figure 2-2. Calculated penetration fields for δ and γ . γ corresponds to the length and δ corresponds to the inner radius. Both are normalised values with respect to the outer radius. The dotted lines are approximations for the solid lines, which express Eq. 2.5, while the dashed lines express Eq. 2.6, and the dotted lines express Eq. 2.7. [67]

In case of a superconducting ring with a diameter much larger than the width of the ring, magnetic flux penetration through the hole is only possible if the induced current caused by the external magnetic field is greater than the critical current of the type II superconductor. If the applied field is lower than the critical current value, the magnetic flux is opposed by the flux caused by the screening supercurrent with a maximum value of $I_c = J_c dw$. The external field which saturates the ring depends on the self-inductance of the superconducting ring. This inductance is defined in terms of the magnetic field current as $I = \phi / L$ [74]. The penetration field in terms of self-inductance is given as [75]:

$$H_p = \frac{\ln(8R/w) - 1/2}{\pi R} I_c \qquad \text{2-8}$$

where $L = \mu_0 R\left(\ln\frac{8R}{w} - \frac{1}{2}\right)$ and $\phi = -\pi R^2 \mu_0 H_p$.

2.2.2 Voltage behaviour of the superconducting ring

The superconducting ring can be represented as an RL circuit with non-linear temperature-dependent resistance [76]. This RL circuit explains the superconducting ring behaviour during magnetization with different induced currents. This process helps in calculating different parameters of the superconducting ring such as inductance, critical current, and n-value. Depending on the magnetic current values, the voltage values can be expressed by three states. Each state gives the value of different parameters of the superconducting ring. The ring acts as a perfect inductive state if $I < I_c$. Further increasing the current $I \leqslant I_c$ it starts generating heat and can be termed as a dissipative state, and it involves the power-law terms for voltage calculation. For $I > I_c$, the thermal losses come into play, and the temperature dependency of the critical current is required. It makes a clear distinction that penetration of the magnetic field is not possible below the critical current, and it cannot perfectly shield the external magnetic field in the middle thus allowing some of it to pass through the middle of the superconducting ring.

2.3 Superconducting coated conductor rings review

HTS rings from coated conductors can be created by joining the two ends of the HTS tapes, and recent joint techniques have shown significant development [15], but these joints induce losses and have problems associated with the soldering of superconductors. This creates the need to make jointless HTS loops, which was successfully demonstrated and fabricated by mechanically cutting the coated conductor in the middle along the length of the tape. The pancake coils fabrication process was suggested for using the loop as mentioned above, created from a coated conductor with a cut in the middle [77]. This fabrication process is named a wind-and-flip technique. It involves four steps which are shown in Figure 2-3. This original undivided coated conductor is shown in Figure 2-3 (a), and the cut in the middle of the coated conductor is shown in Figure 2-3 (b). The process showing the winding of tailored coated conductor tape on separate bobbins is shown, and the current path is also shown in Figure 2-3 (c). The direction of the magnetic fields produced by two pancake coils that lie opposite to each other and will cancel out each other are shown on the right side of Figure 2-3 (c). To avoid the cancelling impact of the magnetic fields produced by two pancake coils, one of the two coils is flipped to create a non-zero-field along with the final field directions as shown in Figure 2-3 (d). In this process, twisting is inevitable which has a negligible critical current reduction; still, it experiences homogeneity disturbance of the central magnetic field because two drooping twisted wires lie outside the coil, which is still to be resolved [78].

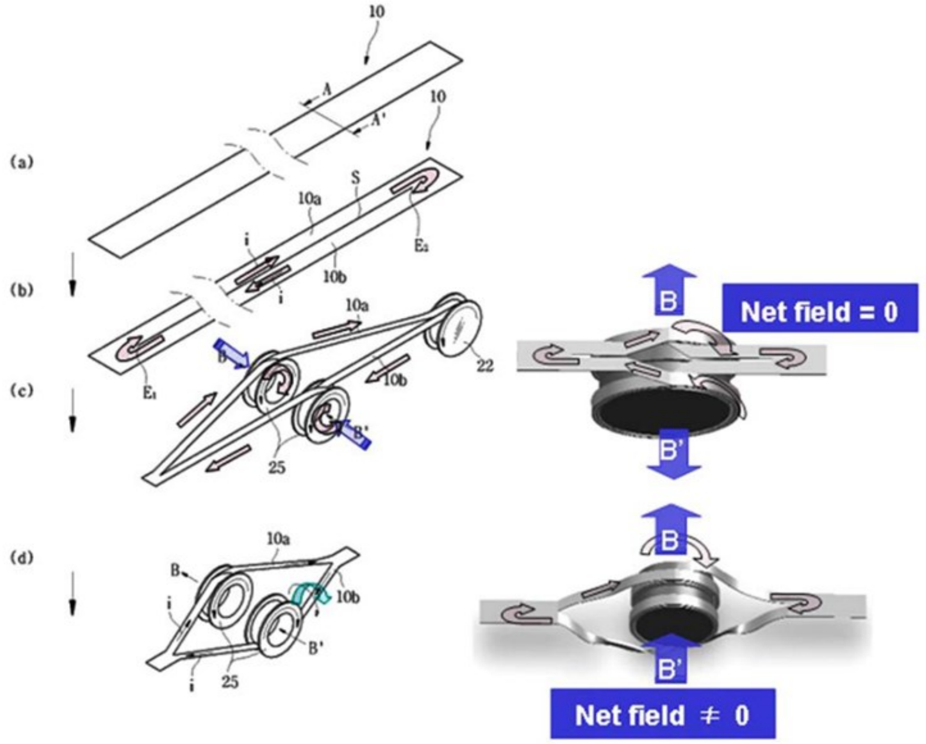

Figure 2-3. Procedure for preparing pancake coils using wind-and-flip method. [77], [78], [79]

The experimental study of the persistent current and decaying rate in the rings made from coated conductors shows that it can sustain larger persistent currents which decay slowly, thus making them a suitable choice for permanent magnet applications [80]. Persistent current in the superconducting ring shows correlation with the applied current pulse parameters, so that increasing the applied current pulse width decreases the amount of persistent current in the superconducting ring [81]. A novel magnetic bearing design by using REBCO tapes which are partially slit to create loops provides larger flux linkages and levitational force than stacked segments [82].

Superconducting rings made from the coated conductors have been used as magnetic bearings, which show a better ratio of levitation force per volume of superconducting material against the bulk [83]. Figure 2-4 shows the levitational force measurement setup using the HTS loops made from superconducting tapes.

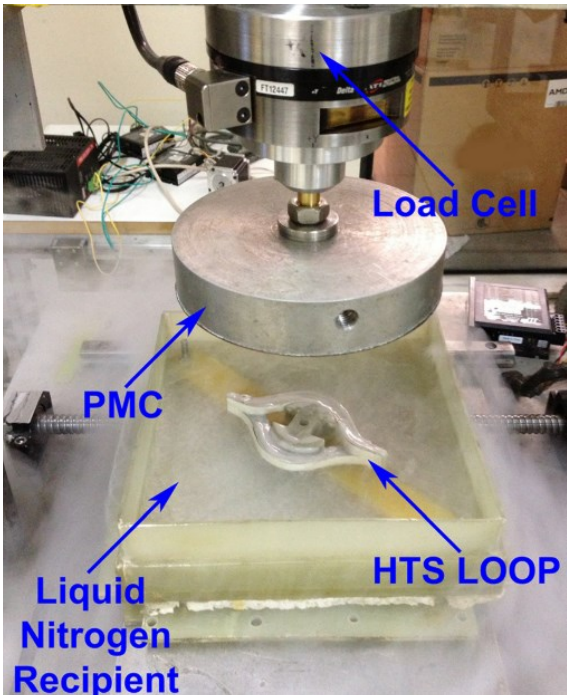

Figure 2-4. Levitational force measurement setup using superconducting coated conductors loops [83]

The loops made from the coated conductors have been used in the self-limiting transformer to form a voltage or current restricting system. Tearing and temporal changes in the current of the machined rings have also been implemented. Figure 2-5 shows the experimental setup which uses loops created from the coated conductor for self-limiting transformers and checking of superconducting rings [84], [85]. A three-phase self-limiting transformer has also been implemented with superconducting loops, which is a further extension of the setup proposed in Figure 2-5. Superconducting loops made from coated conductors can bear a fault current for longer duration and a larger number of times without being damaged [86].

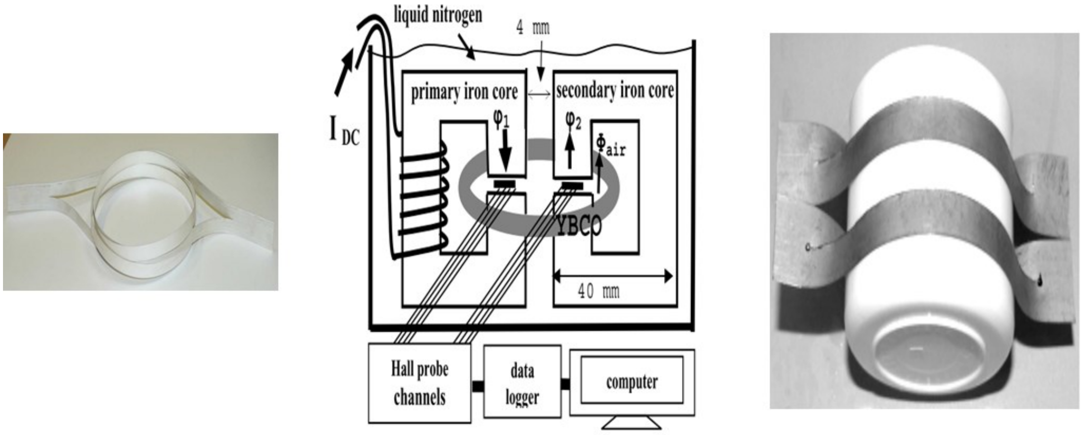

Figure 2-5. Experimental setup for a DC magnetic field using five turn coated conductor serial loop [85], [84].

Loops made from superconducting tapes have been used for fault current applications in which transmissible power and impedance can be influenced by changing the number of loops made from superconducting tapes [87]. Shielding efficiencies for uniaxial and triaxial orientation for the superconducting stacks have been studied [88]. Uniaxial shielding properties point out that the dc magnetic properties of stacks of rings differ from the hollow cylinder in the transverse direction in terms of large saddle-shaped shielding currents loops. A triaxial orientation shows better performance in the transverse direction because of having two more axes. The shielding along the orthogonal axes layer structure is more efficient than the stacked structure. The stacked rings made of the jointless structure have non-uniform current distribution among the turns, and the total trapped field depends on the critical current and applied magnetic field. However, the trapping rate depends entirely on the geometry of the rings; this can be explained with the help of experimentally validated 2D model based on the H-formulation [89].

2.4 Superconducting permanent ring magnet

A new ring shape HTS magnet has been proposed to build an HTS permanent magnet [77][80] with larger diameters. The HTS ring magnet makes a jointless persistent current loop, made from HTS coated conductors by splitting the conductor in the middle and opening it. The HTS rings can be stacked to form a compact magnet, and it can be made flexible in size by choosing different lengths for splitting. The ring magnet is potentially a more resilient device compared to HTS wound magnets as each loop is independent in carrying the persistent current, and any individual loop fault or critical current weak point will not affect the performance of the whole magnet. The full penetration field depends on the critical current density of the superconductor and the geometry of the sample [90]. The critical current density J_c of the ring magnet is relatively higher as compared to HTS stacks and HTS bulks in the same magnetic field. During magnetization, the external magnetic field B_z lies perpendicular to the a-b plane of the REBCO crystals for both HTS bulks and stacks, leading to a dramatic reduction in J_c. The Lorentz force generated by B_z over the induced current helps the individual flux vortices to conquer the pinning forces in the a-b plane. The higher the value of B_z the easier the flux vortex can conquer the pinning forces, therefore the lower the critical current becomes.

In contrast, for HTS ring magnets, the ab plane and the induced current lie parallel to B_z, resulting in zero Lorentz force. The value of J_c will be much less affected by B_z, resulting in a higher J_c. As shown in Figure 2-6, at 25 K and 8 T, the J_c of 2G HTS with advanced pinning in the parallel field is roughly four times the J_c in the perpendicular field (indicated by the blue circles). In other words, four times less HTS materials will be required to take the same amount of current at 8 T for the HTS ring magnet, in comparison to the HTS bulks and stacks. The operational temperature of the magnet also affects the critical current and the generated magnetic field. As shown in Figure 2-6, the lower the temperature, the higher the critical current when subjected to an external magnetic field.

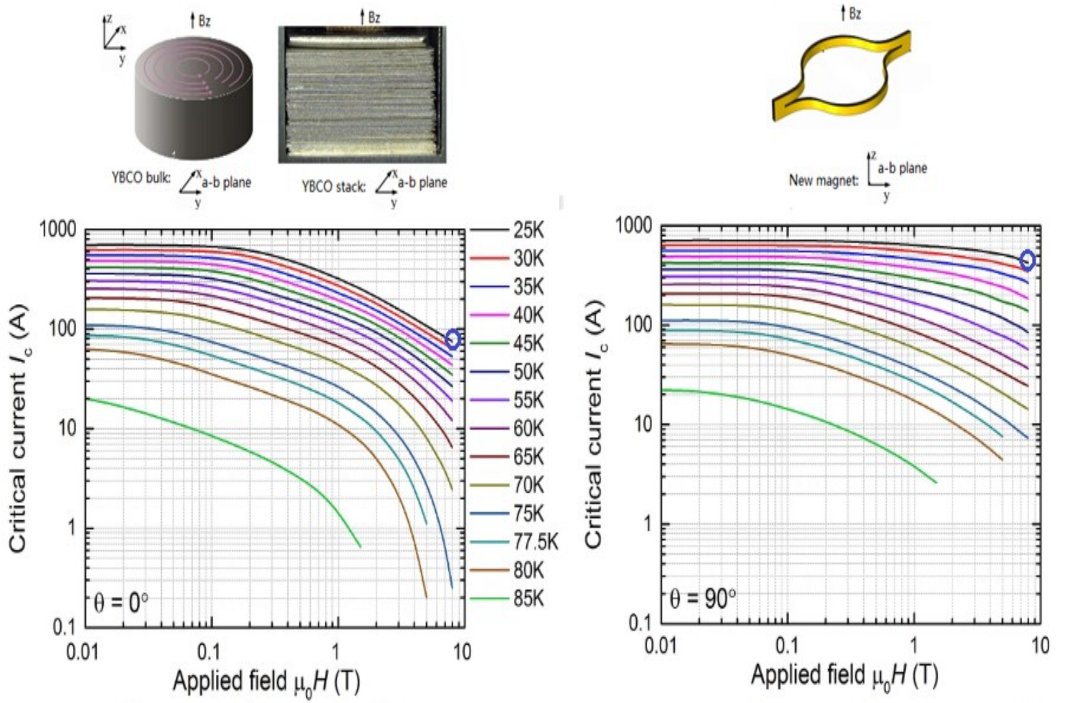

(a) critical current of a 4 mm YBCO tape subjected to an applied field perpendicular to the a-b plane.

(b) critical current of the same 4 mm YBCO tape subjected to an applied field parallel to the a-b plane.

Figure 2-6. The critical current comparison between an HTS bulk/stack and HTS ring magnet showing that at 8 T @25 K, the HTS ring has a critical current five times higher than the HTS bulk/stack. The critical current data reproduced from the detailed measurements of a 2G HTS YBCO wire at the Robinson Research Institute of Victoria University of Wellington [91].

A feasibility study for HTS rings at low magnetic fields has been reported [77]. The relationship between the trapped field and the ring geometry, as well as the demagnetization subjected to a cross AC field, is reported by Jie Sheng et al. [92]. Several persistent current HTS coils have been made using YBCO tapes, and field cooling was performed for trapped fields [93] [94]. The relaxation rate of the current and external magnetic fields have been experimentally validated [95].

2.5 Thesis contribution

Sections 2.3 and 2.4, showed that the rings made from 2G HTS superconducting tapes provide jointless loops and they can sustain persistent currents. Still, they have not been tested to form high field permanent magnets. In the light of the above discussion, it was felt necessary to design and test a permanent magnet which can be used for different applications involving large diameters. Every new magnet design should be investigated thoroughly to prove its effectiveness. The new design needs validation both mathematically and experimentally. For this purpose, a 3D model is needed, which can explain the behaviour of the new ring magnet. Experiments should also be done to prove the models. After proper investigation, if some discrepancies exist, these should be rectified to make the new design practically feasible. The validated model was used to predict the behaviour of the new ring magnet during magnetization. FC and ZFC were performed by using the 2D and 3D models in COMSOL. The 2D and 3D model showed good validation of the experiment results. The 3D model also predicted the asymmetric trapped field distribution in the ring magnet, and the impact of ramping rate and temperature on the trapped field were also examined.

Three superconducting tapes from different suppliers were used. The properties of each superconducting tape used are discussed. The impact of different layers on the stiffness of the tape is discussed. Different cut lengths were used for different inner diameters. Different impregnation schemes were used to improve the thermal conductivity of the magnet.

The experimental setup at the University of Cambridge used to perform FC and ZFC experiments is explained. The experiment results for all magnets have been explained and compared with the modelling results. The behaviour and performance of the different superconducting ring magnets at cryogenic temperature are studied, and the trapped field for each magnet is observed.

A new optimised superconducting ring magnet design made from 2G HTS tapes is proposed and discussed, which can trap high magnetic fields and thus improve field distribution.

2.6 Conclusion

Persistent current can be induced in superconducting rings below the critical temperature. These rings retain the induced current after the removal of the external field if the temperature is kept constant. The induced current creates a magnetic field which is the trapped magnetic field. The magnetization depends upon two factors: the length and diameter of the rings. With an increase in length, a greater external magnetic field is required to saturate the rings, and by increasing the diameter, the trapped field in the middle decreases. Some relevant designs are also presented along with the published results.

3 NUMERICAL MODELLING OF SUPERCONDUCTING RINGS

A new ring magnet is numerically designed and modelled in this chapter. Several numerical models and analytical models have been developed for the critical state of superconductors, which can be implemented for uniform magnetic fields and basic geometries of superconductors. The numerical modelling of superconductors is done using the finite element method (FEM) or finite difference method for solving Maxwell equations, combined with the E-J power law in 2D and 3D. The H-formulation has been implemented for ring magnets. The 3D homogenized model has been designed for ring magnets. Field cooling (FC) and zero-field cooling (ZFC) are performed to calculate the trapped field in the ring magnet. Comparison between the 2D and 3D models for the trapped field is also performed in this chapter.

3.1 Numerical Modelling

Numerical methods can be used to solve the critical state of the superconductors, and for simple geometries and field conditions, the analytical methods have been developed. Analytical methods usually involve simple mathematical equations and provide a time-efficient method to understand electromagnetic behaviour. However, due to different geometries and configurations of superconductors numerical method are more practical. In superconductors, The Meissner effect is one of the obvious characteristics when an external magnetic field is applied, which induces a magnetic field opposite to applied field. The challenging part of the superconducting model is the determination of the self-field or external field current distribution.

3.1.1 Finite element Method

The finite element method (FEM) or finite difference methods are used for numerical modelling of Maxwell equations. FEM is one of the most used tools for solving partial differential equations. In this technique, domains are represented as finite elements, and unknown nodal values of physical fields are expressed as discrete functions of finite elements. Two features of the FEM worth mentioning are 1) piecewise approximation of physical fields on finite elements provides good precision even with simple approximating functions (increasing the number of elements can achieve any precision), and 2) locality of approximation leads to sparse equation systems for a discretized problem. This helps to solve problems with a very large number of nodal unknowns [96]. The main steps involved to execute finite elements solutions can be summarised as discretization, interpolation function selection, elemental properties, assembling of element equations, solving global equations, and additional results computation.

Three main numerical methods are used, which are named after the variables used in the partial differential equations, The A-V-formulation is used for the magnetic vector potential [97] [98], The T-Ω-formulation is used for the current vector potential [99] [100], and the H-formulation is used for magnetic field [101] [102]. Comparison between these formulations has been undertaken in many studies [103] [104]. The H-formulation has been used for my 3D model, as the A-V and T- Ω formulations both involves four variables [104] while the H-formulation has only three variables. Also, in H-formulation, there are no second-order derivatives, which makes gauge choice easier [102] and has better computation speed. Calculation inaccuracies related to vector potential differentiation are not involved in the H-formulation. Integration of boundary conditions can be practically implemented in the H-formulation, which allows for the transport current and external field to be considered together. Conventional Maxwell equations can be used for superconductors with modified material properties. The H-formulation is implemented using COMSOL Multiphysics version 5.a and 2D and 3D. The H-formulation provides a relatively straightforward approach to implement boundary conditions related to the current in superconductors and external magnetic fields. The external field can be applied in boundary conditions, and Amperes Law incorporates the transport current. This space is divided into the air and superconducting regions. This section starts with the conventional electromagnetism problem and extends the concept to superconductors.

Ampere's law defines the quantitative measurement of a magnetic field by a current:

$$\oint H\,.\,dl = I = \int_S (\nabla \times H).dS = \int_S J.\,dS \tag{3-1}$$

$$\int_S (\nabla \times H).dS = \int_S J\,.\,dS \tag{3-2}$$

$$\nabla \times H = J \tag{3-3}$$

Equation 3.3 can be used be for solving the current density **J** if the magnetic field distribution **H** is known. The electrical and magnetic properties of the material can be described as:

$$B = \mu_0\, H \tag{3-4}$$

The Maxwell equations are:

$$\nabla \times E = -\frac{dB}{dt} = -\mu_0 \frac{dH}{dt} \tag{3-5}$$

Equation 3.5 is the Faraday Law of electromagnetism. By knowing the **E** distribution, the time-varying **H** can be solved. It means that after every iteration, the **H** value is incremented and for each new value, the current density distribution **J** and electric field **E** will be changed. For superconductors, The Maxwell equations still work, but the material properties should be changed. The practical approximation used to define superconductor electrical properties is the **E-J** power law [105]. In this the electric field is directly proportional to the current density but with a higher power. The **E-J** power-law used in my model is:

$$E_J = E_0 \times \left(\frac{J_{tot}}{J_{c0}}\right) \times \left(\frac{\text{abs}\,(J_{tot})}{J_{c0}}\right)^n \tag{3-6}$$

where $\mathbf{E_0}$ is the electric field threshold used to define critical current density $\mathbf{J_c}$, and is equal to 10^{-4} μV/m, and *n* is a parameter to fit the above equation to experimental measurements. The n value used for my model is n=31. This higher value was used to give practical flux creep rates, but it causes difficulties in computation. Partial differential equations (PDE) are non-linear and creates instabilities which can be minimised by controlling the parameters such as mesh element size, time steps and tolerance values.

Equation 3.6 along with equations 3.3 and 3.5 are used to calculate the current and magnetic field distributions of a superconductor. As these equations involve only the **H** variable, it is named as the H-formulation [101].

3.2 2D modelling

Several variables calculations relate to the dimensions in the H-formulation. The 1D, 2D and 3D models are named accordingly. The 1D and 2D H-formulation were implemented in COMSOL by Z. Hong, and he got impressive simulated results [101]. Grilli implemented this approach for AC loss calculation, and the model was validated [106]. M. Zhang validated this model for complex geometries and materials [107] [108].

The most widely used formulation is the H-formulation, which was firstly introduced in 2006. The H-formulation is easy to implement in the COMSOL software. Cartesian and cylindrical coordinates can be implemented by using the 2D model. Infinitely long thin film tapes are modelled using cartesian coordinates, while cylindrically shaped coils, rings and bulks are modelled by using equations based on cylindrical coordinates. In the 2D model for a cylindrical shaped object, axis-symmetric models are used. Only one side is modelled practically while the model itself completes the other half. In the results section, we can get the 3D graph of the geometry, which will show the other half of the geometry. Figure 3-1 shows the difference between cartesian and cylindrical systems implemented in COMSOL.

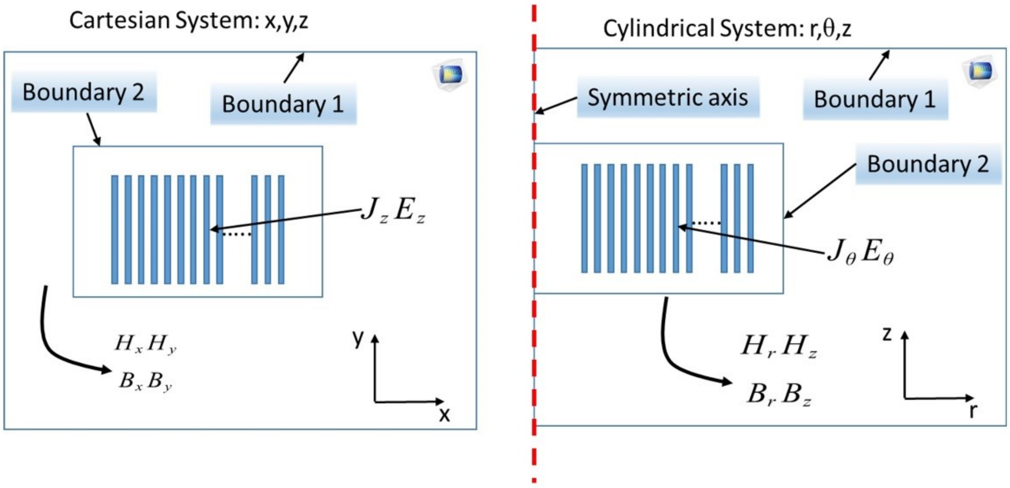

Figure 3-1.Implementation of boundaries and domain for cartesian and cylindrical systems in 2D COMSOL. The cylindrical system is implemented as the axis-symmetric 2D model in COMSOL.

Two variables in the 2D cylindrical model are defined as H= [$H_{r;}$ H_z]. For air and normal conductors, Ohm's Law is simply used as the E-J law, which is $E_\phi = \rho J_\phi$. The Kim model is used to define $J_c(B)$

$$J_c(B) = \frac{J_{c0}}{1 + \frac{B}{B_0}} \tag{3-7}$$

where $B = \mu_0 \mu_r \sqrt{H_r^2 + H_z^2}$. It gives an excellent practical approximation for general J_c behaviour. Ampere's law defines the critical current density concerning the field components as follows

$$J_\phi = \frac{\partial H_z}{\partial r} - \frac{\partial H_r}{\partial z} \tag{3-8}$$

For a cylindrical system, the final partial differential equations in terms of field components are given by:

$$\begin{bmatrix} -\dfrac{\partial\left(rE_0\left(\dfrac{\frac{\partial H_z}{\partial r}-\frac{\partial H_r}{\partial z}}{J_c}\right)^n\right)}{\partial z} \\ \dfrac{\partial\left(rE_0\left(\dfrac{\frac{\partial H_z}{\partial r}-\frac{\partial H_r}{\partial z}}{J_c}\right)^n\right)}{\partial r} \end{bmatrix} = -\mu_0\mu_r r\begin{bmatrix} \dfrac{\partial H_r}{\partial t} \\ \dfrac{\partial H_z}{\partial t} \end{bmatrix} \tag{3-9}$$

A Dirichlet boundary condition was used for boundary 1 in Figure 3-1 and symmetric axis boundary. The superconductor is magnetized by the application of the external magnetic field as time-varying functions:

$$\begin{gathered} H_r = F_r(t) \\ H_z = F_z(t) = B_{app}/\mu_0 \end{gathered} \tag{3-10}$$

B_{app} is defined in the parameters. The general form of partial differential equation used in COMSOL is given as:

$$\nabla.\Gamma + d_a\frac{\partial u}{\partial t} = f \tag{3-11}$$

which contains coefficients in the form of vectors or matrices of vectors. To obtain Equation 3.9, the following values are substituted into Equation 3.11:

$$\Gamma = \begin{pmatrix} \begin{pmatrix} 0 \\ rE_0 \end{pmatrix} \\ \begin{pmatrix} rE_0 \\ 0 \end{pmatrix} \end{pmatrix}, \qquad d_a = \mu_0\begin{pmatrix} \begin{pmatrix} r \\ 0 \end{pmatrix} \\ \begin{pmatrix} 0 \\ r \end{pmatrix} \end{pmatrix}, \qquad u = \begin{pmatrix} H_r \\ H_z \end{pmatrix} \tag{3-12}$$

Careful attention should be given to the type of mesh, tolerance and time steps for stability while solving the above equations in COMSOL. Smaller steps are better for stability, but it increases the computation time. A mapped mesh with a different number of elements was implemented, which is stable enough to complete the simulation with minimum time.

3.3 2D ring model setting

A cylindrical coordinate system is used for the 2D model. In the 2D COMSOL model, this is implemented as a 2D axis-symmetric model, as explained in Fig. 3.1. The external magnetic field is applied to Boundary 1. The 2D axial symmetrical model has two variables, defined as H = [H_r, H_z]. The induced current J_ϕ is in the ϕ direction. The model used to drive the critical current is explained in [109]. The normalised values of currents for the parallel and perpendicular fields are derived by using the data of tapes taken from the database of high-temperature superconducting tapes [91]. These values are used as an interpolation in the model, named as parallel and perpendicular. They are used to calculate the angle which is used to measure the critical current density of the tapes. Figure 3-2 shows the normalised values for SuNAM and Shanghai tapes at 30 K.

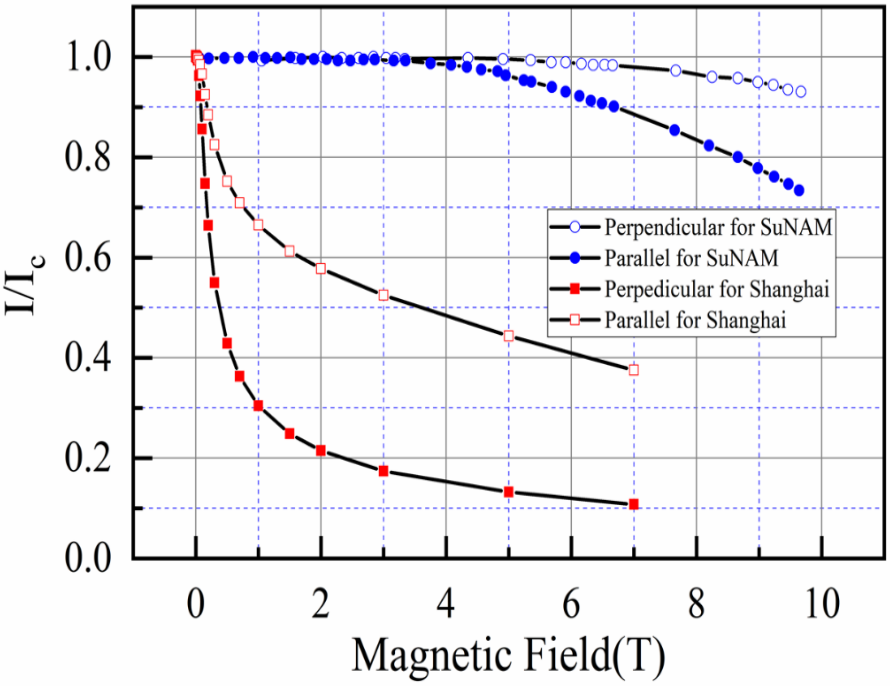

Figure 3-2. Normalised values of current in the parallel and perpendicular field at 30 K. This is obtained from data available in [91]. (Here perpendicular is used when the field is normal to tape surface and parallel for a field direction parallel to the tape surface.

The expression for current density used in the model is [109]:

$$J_c(B,\theta) = J_{c0}*\ (P_1(B) + (P_2(B) - P_1(B))*G(\theta)) \qquad \text{3-13}$$

where G is the normalised angular dependence of the field for which in our model we have taken values up to 7 T, and J_{c0} is the critical current density without external magnetic field. When θ is perpendicular, this means 90° the critical current will depend on the critical current without a magnetic field and perpendicular field dependence. When θ is parallel means 0 (zero), the critical current density will be equal to the product of critical current without magnetic field and parallel field dependence. P_1(B) stands for the perpendicular field dependence of the critical current density. P_2(B) is the parallel field dependence of the critical current.

Figure 3-3 shows the normalised experimental data for the critical current under different field angle. These graphs are used as interpolation for angles in the model, and it defines G(θ) in equation 3.22.

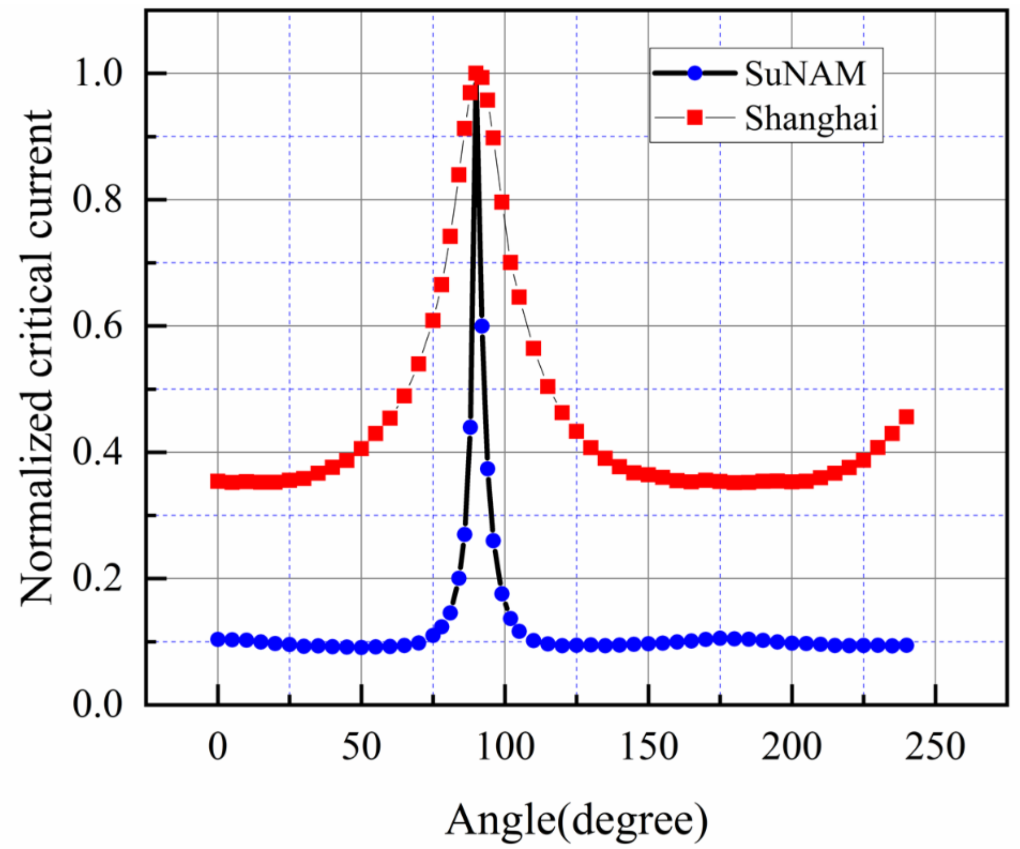

Figure 3-3. Normalised data of the critical tapes under different field angles at 30 K. This is obtained from [91].

3.4 2D to 3D model justification

During the experiment results, it was noticed that the trapped field distribution of the ring magnet is not symmetrical, which was not noticed in the 2D model. It was decided to create a 3D model with the original dimensions of the magnet, as the axis-symmetry 2D model, creates a homogenised distribution along the axis. However, our magnet geometry was not the symmetric, so it was decided to create a 3D model with the original geometry and outlook. The 3D model is explained in the next section.

3.4.1 3D model

In the 3D model, there are three variables for the magnetic field, current, and electric field. H_x, H_y, H_z represent the three-dimensional magnetic field, J_x, J_y, J_z and E_x, E_y, E_z are the current and the electric field representation for 3D modelling. The 3D model provides a more practical approach for complex geometries and for situations in which the current and magnetic fields are not perpendicular to each other.

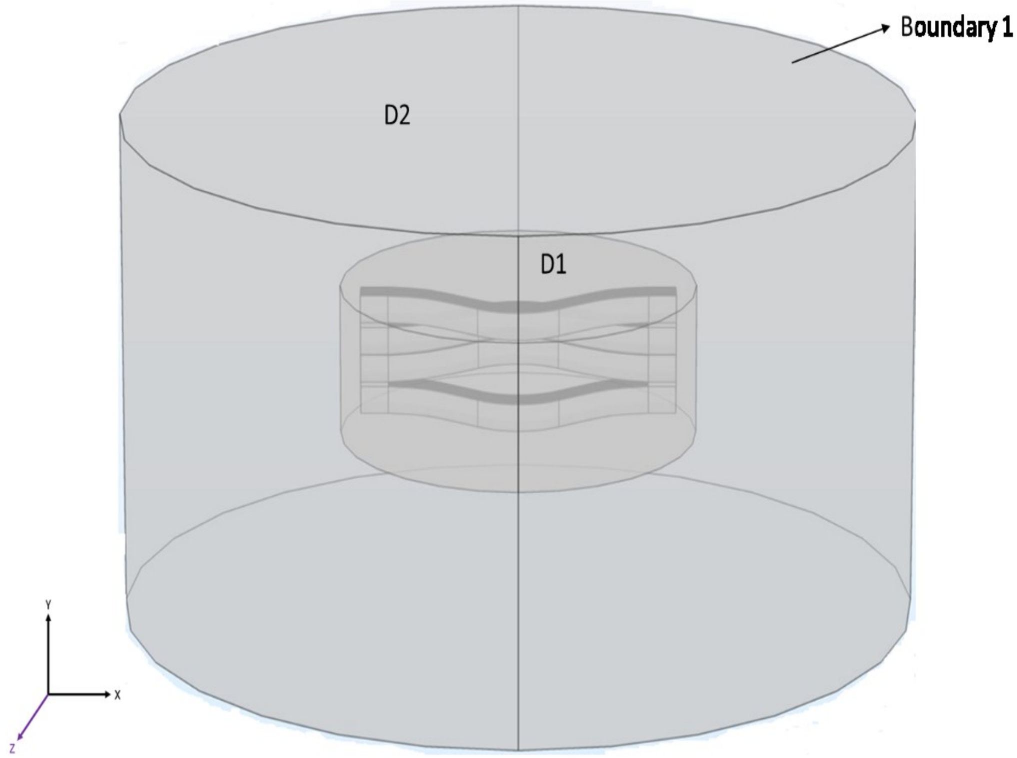

Figure 3-4. 3D configuration of subdomain and boundaries applied in actual 3D model.

Ampere’s Law in 3D dimensions:

$$\begin{bmatrix} J_x \\ J_y \\ J_z \end{bmatrix} = \begin{bmatrix} \dfrac{\partial H_z}{\partial y} - \dfrac{\partial H_y}{\partial z} \\ \dfrac{\partial H_x}{\partial z} - \dfrac{\partial H_z}{\partial x} \\ \dfrac{\partial H_y}{\partial x} - \dfrac{\partial H_x}{\partial y} \end{bmatrix} = \begin{bmatrix} H_{zy} - H_{yz} \\ H_{xz} - H_{zx} \\ H_{yx} - H_{xy} \end{bmatrix} \qquad 3\text{-}14$$

Faraday’s Law in 3D dimensions:

$$\begin{bmatrix} \frac{\partial H_z}{\partial y} - \frac{\partial H_y}{\partial z} \\ \frac{\partial H_x}{\partial z} - \frac{\partial H_z}{\partial x} \\ \frac{\partial H_y}{\partial x} - \frac{\partial H_x}{\partial y} \end{bmatrix} = -\mu_0 \mu_r \begin{bmatrix} \frac{\partial H_x}{\partial t} \\ \frac{\partial H_y}{\partial t} \\ \frac{\partial H_z}{\partial t} \end{bmatrix} \qquad 3\text{-}15$$

The E-J power-law becomes:

$$\begin{bmatrix} E_x \\ E_y \\ E_z \end{bmatrix} = E_0 \begin{bmatrix} \frac{J_x}{J_n}\left(\frac{J_n}{J_c}\right)^n \\ \frac{J_y}{J_n}\left(\frac{J_n}{J_c}\right)^n \\ \frac{J_z}{J_n}\left(\frac{J_n}{J_c}\right)^n \end{bmatrix} \qquad 3\text{-}16$$

Where $J_n = \sqrt{J_x^2 + J_y^2 + J_z^2}$.

The PDE’s of Equations 2.24, 2,25 and 2,26 are combined together and solved in the 3D FEM simulation.

3.4.2 3D homogenization

A technique to implement 3D homogenization for superconducting coils and tape stacks has been discussed by Víctor M R Zermeño et al. [110] [111]. In the original, 200 rings were stacked together with the asymmetric distribution. It was not possible to model all the rings due to the high aspect ratio of the 2G HTS tapes. The main purpose of this homogenization is to make a superconducting bulk material from separate tapes, which exhibits the same electromagnetic properties as tapes stacked together and carries the same current equal to the number of tapes in the stack. This gives a much simpler geometry instead of individual tapes, and improves the computation time. The separation between each tape stack is considered constant. Figure 3-5 shows the comparison of actual stack and its homogenised model. Figure 3-5 (a) shows the actual 200 rings stacked together, while Figure 3-5 (b) shows the corresponding homogenised model, representing the 200 rings with 20 domains. Two assumptions were made in the homogenised model. First, the thickness of the HTS layer has been artificially increased from $1\mu m$ to $74\mu m$, which is the total thickness of the tape. The second assumption is related to the critical current penetration depth. For every 10 HTS rings, one HTS homogenised domain is created. This one homogenised HTS domain has the same critical current distribution as that of 10 HTS rings. This homogenised stack is considered to be a bulk which represents 200 rings. In between each HTS domain there is a air domain whose width is $1\mu m$.

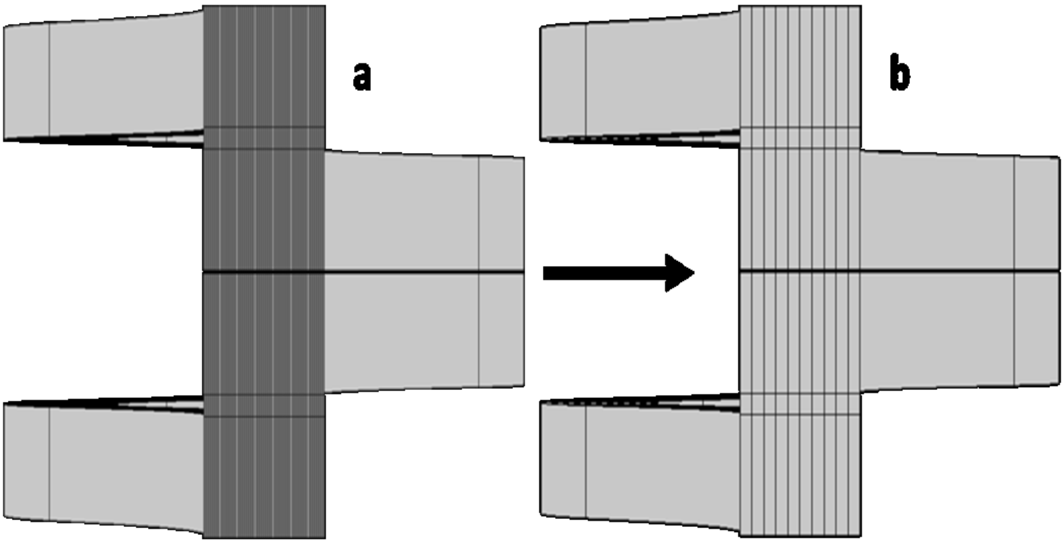

Figure 3-5. Actual layout and the corresponding homogenised model comparison. (a) 200 tapes are stacked together. (b) 20 domains are created in the 3D homogenised model as a set of 20 stacks with each domain equal to 10 rings.

3.4.3 3D ring model settings

Figure 3-4 shows the domains and boundaries to which to apply the Dirichlet conditions. The external magnetic field was applied to boundary 1. The applied field was interpolated to form the desired function:

$$H = f(t) \tag{3-17}$$

where f(t) is a function which varies with time in all directions. The critical current I_c of the tape used was interpolated from the available experimental data. The data file has the current values from 0 to 180 degree in radian units. The interpolated data used in the model is shown in Figure 3-6, and the data was taken for a temperature of 25 K [91]. The figure plots the critical current over magnetic field and angle. The critical current density was obtained by dividing the critical current by the area of the tape.

$$J_c = I_c(pi/2, B_z)/Area \qquad 3\text{-}18$$

Equation 3.28 is substituted in equation 3.26 to implement E-J power characteristics.

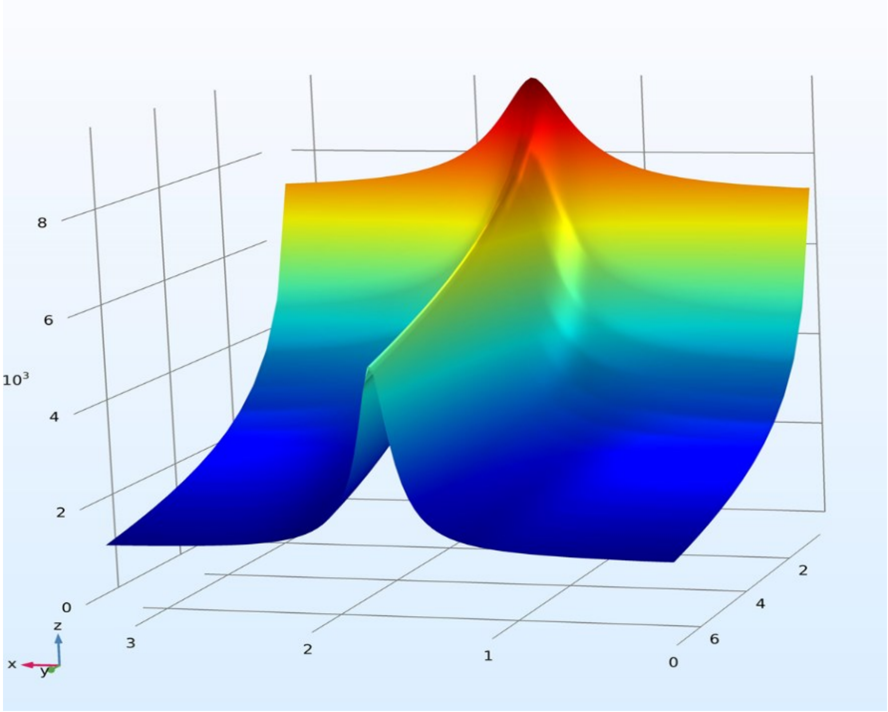

Figure 3-6. Critical Current profile interpolated in the COMSOL model. This was obtained by interpolation of experiment data of SuperPower tapes at 25 K

In the COMSOL 3D model geometry, tetrahedral, mapped and swept meshing are used. For air and refinement area, tetrahedral meshing was used. Tetrahedral meshing automatically meshes the whole area with tetrahedral elements, as shown in Figure 3-7 (a). The only difference is that for the refinement area, a finer element size is used. For the superconducting ring, mapped and swept meshing is used. Each subdomain of the ring is conventionally mapped as a 2D mesh with a different number of elements to make a homogenised ring and then swept by assigning a step size. A single ring stack is swept as a top, middle, and bottom part. Figure 3-7 (b) shows the swept meshing of the ring.

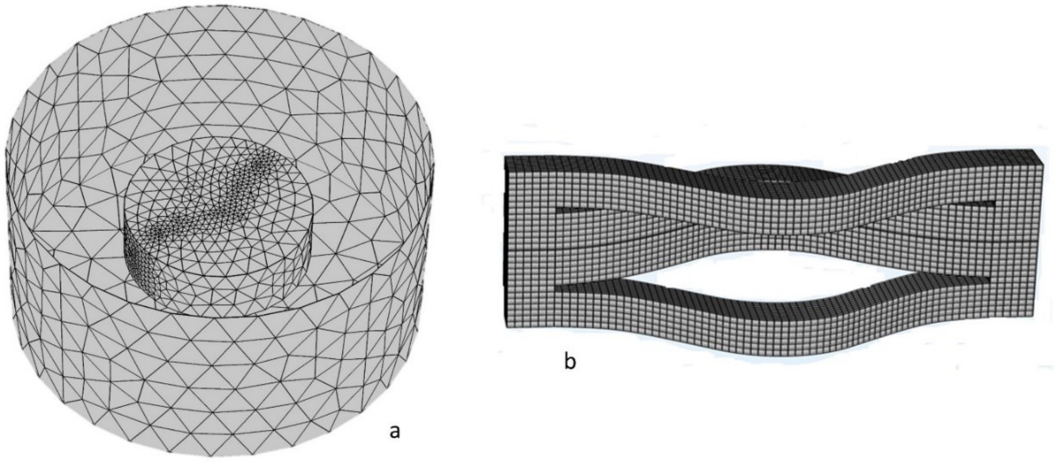

Figure 3-7. (a)Tetrahedral Meshing applied for the air and refinement area (b) swept meshing for the HTS domains.

The swept meshing guarantees that there are sufficient mesh elements in a tape cross-section with a limited total number of mesh elements due to the high aspect ratio. The aspect ratio is defined as width over thickness. The direct method, MUMPS, was used as a default solver. To ensure accuracy in the results, the relative and absolute tolerances of the calculation should be less than the default value, which is 10^{-5}. The time steps depend on the complexity of the geometry; for our geometry, strict time was used with a defined range. The computation was carried out using Intel an i7 3.6 GHz processor with 32 GB of memory.

Computational time is proportional to the number of mesh elements and external stimulations. In this case, the external stimulation was B_{app}. The 3D model contains approximately 250,000 elements, and the computational time was 2 hours.

3.4.4 2D and 3D Model Comparison

In this section, the 2D model and 3D model results are compared for the middle position of the sensor. The 2D model is the axial symmetric type. The field cooling process was used to magnetize the superconducting rings in these models. The superconducting rings were cooled down to the critical temperatures in the presence of the external magnetic field. Temperature variations were not recorded for the rings, as for this purpose the applied field changing rate was kept sufficiently slow.

In both models, the same applied field was used in the form of interpolation. This result was for 200 rings, and the process of magnetization is field cooling. The inner diameter was 1 cm for both 2D and 3D models in Figure 3-8 (a), and the maximum trapped field is plotted by using $B_{trap} - B_{ext}$ expression at 5 T FC, while in Figure 3-8 (b) the diameter was increased to 2 cm and showed the values of the trapped field against the applied field.

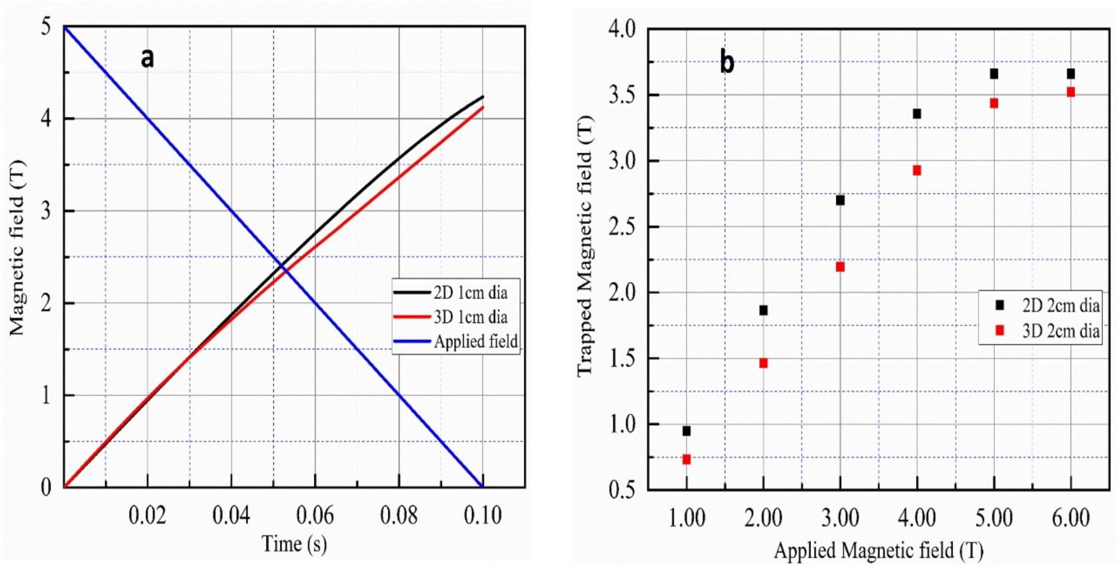

Figure 3-8. Maximum trapped field after FC from the 2D and 3D models with different diameters. The point is (0,0) for the 2D and (0,0,0) for the 3D model. In (a) $B_{trap} - B_{ext}$ values for 5T are presented while time was kept constant for both modelling results, i.e. 0.1 sec while in (b) maximum trapped field values are taken against each applied field for 2 cm diameter rings. The simulation time was 0.1 sec for both 2D and 3D models.

The 2D and 3D model results were nearly identical. The difference is due to the geometry. The actual geometry is considered in the 3D model while the 2D model assumes an asymmetric field distribution. In the actual geometry, the asymmetric shape of the ring magnet is taken into account. For the 2D model, only the diameter was different, but in the 3D model the length of the rings also changes with changing diameter. It was noted that changing the internal diameter affected the trapped field, ao that as the internal diameter increased the trapped field decreased. The 3D model is more practical and beneficial in explanation of this new ring magnet design. Further details are explained in chapter 6.

3.5 Conclusion

This chapter implements the 2D and 3D modelling of the ring magnets. It explains the basic equations for implementing the H-formulation and *E-J* power law. The software used to implement the finite element modelling (FEM) was COMSOL. Comparisons between different formulation techniques of finite element modelling were mentioned, such as the A-V formulation, T-Ω formulation and H-formulation. It explains the boundary conditions, background fields, and meshing applied in the actual model.

For 2D models, axis-symmetric modelling was performed. For each tape used, normalised data for parallel, perpendicular fields and angles were interpolated. The 2D modelling results are presented in chapter 5, along with the experimental data.

The 3D model is implemented using the H-formulation. The 3D model implements the original dimensions of the ring magnet. A comparison was made between the 2D and 3D models at the middle of the tape, and both models had nearly the same values. The difference between the two is due to their geometry.

4 SAMPLE PREPARATION

This chapter provides an introduction to superconducting tapes production methods and the structural differences between the SuNAM, Shanghai and SuperPower superconducting tapes. In total five magnets were prepared and magnetized. The process of creating the superconducting ring magnets along with the impregnation techniques are alsodiscussed in this chapter. The types of hall sensors used for measuing the data during each experiment and their positions are explained in this chapter as well.

4.1 Manufacturing process of superconducting tapes

2G HTS coated conductors (CC) are cost-efficient and have shown better performance in external magnetic fields. The fabrication process of 2G HTS CC is a continuous and automated process in which superconducting material is applied to the metal substrate [112]. 2G HTS coated conductors are commercially available in long lengths of wires and tapes, which makes it possible for them to be used in practical applications such as electric machines, superconducting magnetic energy storage systems, and transformers.

There are two prevalent manufacturing processes of 2G HTS tapes which biaxially align the HTS layer: IBAD and RABiTS. Figure 4-1 shows the typical structure of these processes [113]. These processes define the structure of the final 2G HTS CC. Generally, all 2G HTS tapes consist of a substrate, buffer, HTS, and stabilizer layers. HTS layer is the rare-earth barium copper oxide (REBCO), and the thickness of the substrate layer varies from 50 µm to 100 µm. This layer serves as a carrier to the HTS layer. The buffer layer provides a texture template for the HTS, and its thermal expansion coefficient should match the substrate and HTS layer to avoid thermal cracking.

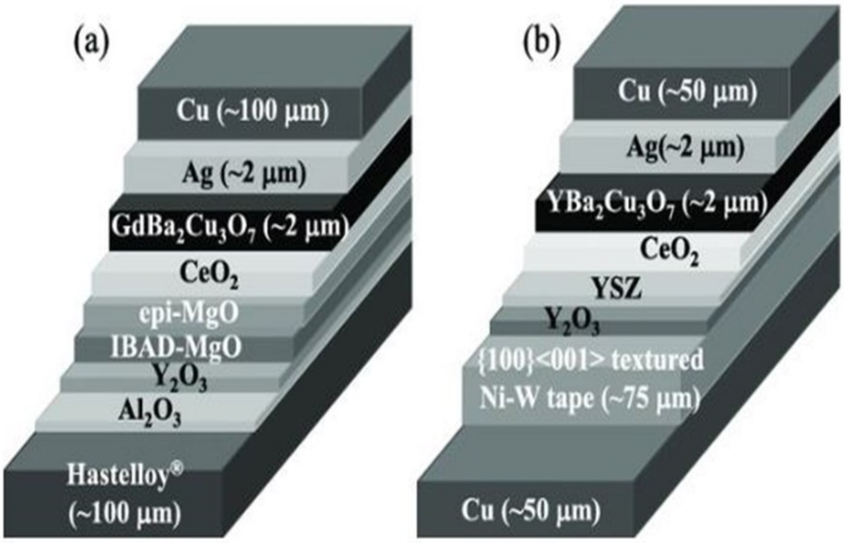

Figure 4-1.Figure. 3.2. Schematic of (a) IBAD and (b) RABiTS type superconducting wires. [113]

IBAD refers to ion-beam assisted deposition. In this, the buffer layer in biaxial orientation is deposited on the non-magnetic substrate (e.g. Hastelloy C276, or stainless steel SS304) by bombarding Ar ions from a slanting direction to form the template layer [114]. Widely used deposition techniques in IBAD are Metal-Organic Chemical Vapour Deposition (MOCVD) and Pulse Laser Deposition (PLD). Superpower uses MOCVD, while Fujikura and Sumitomo use PLD techniques. Usually, copper or stainless steel are used as stabilizers.

RABiTS stand for Rolling Assisted Biaxially Textured Substrate. A. Goyal et al. proposed in [115], Ni substrate is prepared by rolling and annealing with the desired texture. In this process, the Metal-Organic Deposition (MOD) method is used to deposit rare-earth barium copper oxide. Superpower, AMSC and IGC have already produced RABiTS tapes with much better electromechanical properties by using CeO_2/YSZ/Y_3O_3 buffers [116].

The fundamental difference between IBAD and RABiTS is only the substrate type. IBAD uses a non-metal untextured substrate and has a crystalline structure while the RABiTS uses a Nickel-metal or metal textured substrate and has a cubic structure [117]. It is a well-proven fact that the performance of the HTS is affected by the magnetic substrate during the changing magnetic field distribution [24; 25; 26].

4.2 Procedure to make HTS ring magnet

The general procedure to produce the rings used throughout this project is shown in Figure 4-2.

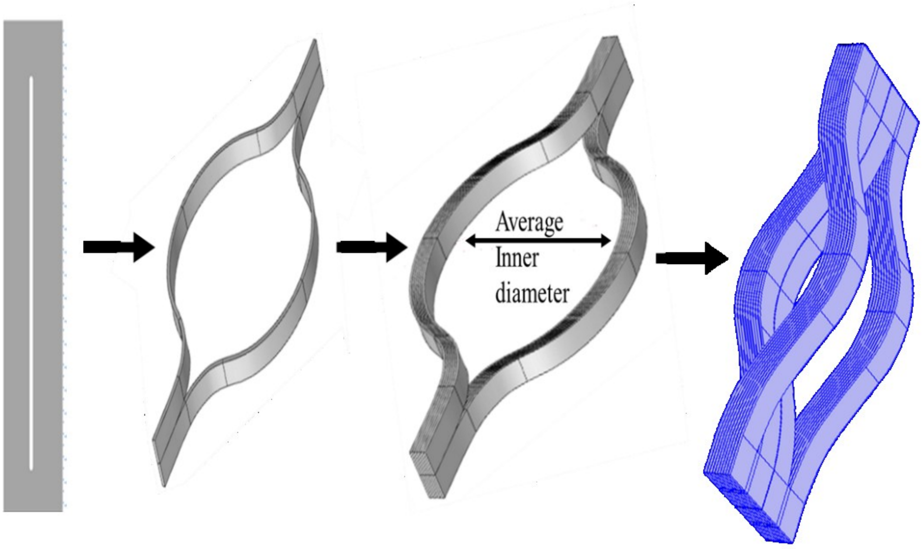

Figure 4-2. Process for creating rings and stacking them to create a ring magnet.

It starts by splitting the 2G HTS coated conductor in the middle. Next is the opening of the tape and giving it a proper ring shape. After shaping it, the next step is the stacking of the rings. One important aspect of stacking is that the first ring makes the inner side of the ring on one side and the outer side on the opposite side. The final arrangement of the ring magnet layers the stacks on each other and is shown in blue in Figure 4-2. The main advantage of 2G HTS ring magnets is their simple and easy construction with larger sizes. The dimensions of each sample used are explained in the following sections of this thesis.

4.3 SuNAM Sample

The tapes used were from SuNAM Co. Ltd. It was 12 mm in width, and it was silver coated. The superconducting material used was GdBCO (gadolinium barium copper oxide). A new deposition method RCE-DR (Reactive Co-Evaporation Deposition &

Reaction) has been used to produce considerable lengths. GdBCO CC manufactured by RCE-DR has a potential critical current of 794 A for a 12 mm width tape [121]. The architecture of the SuNAM tape is shown in Figure 4-3. The superconducting material contributes less than 3% of the overall volume, where the substrate made of Hastelloy C276 accounts for more than 70% by volume. This more significant proportion of Hastelloy by volume makes this tape brittle which makes it difficult to be opened and stacked while making the ring magnet.

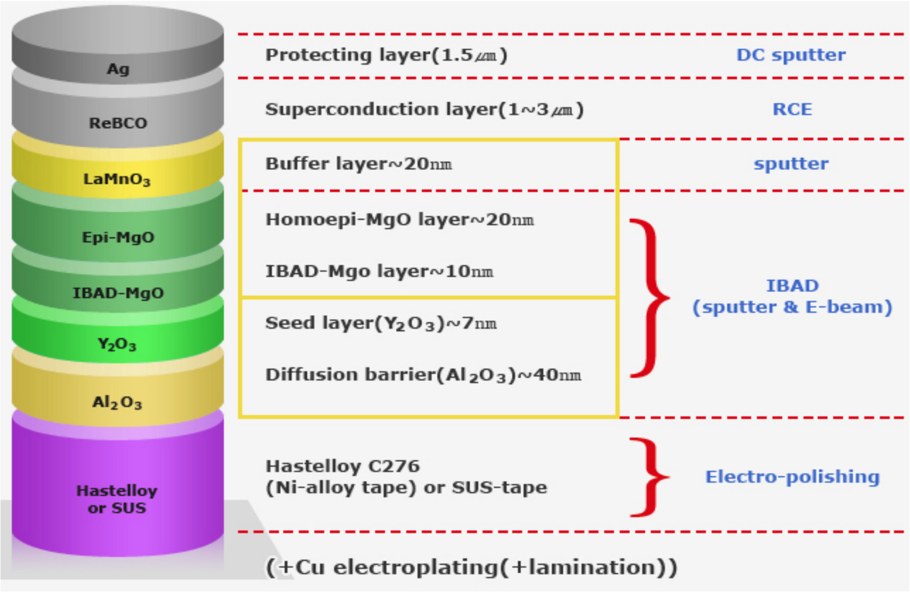

Figure 4-3. Schematic of SuNAM Tape used [122], showing the components and dimensions of 12 mm wide SuNAM superconducting tapes from which the rings were made.

The cut length was 85 mm and 6 mm along the full edge of each side for each ring, as shown in Figure 4-4. A mechanical cutter was used to cut the tape down the middle of the 12 mm tape. The inner diameter of the cup was 35 mm. The cut length depends on the diameter of the former on which these rings are to be adjusted. If the holder diameter is increased, the cut length will increase as well, and vice versa.

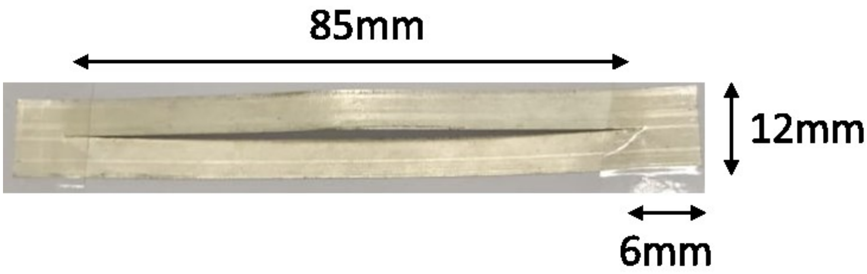

Figure 4-4. SuNAM tape after cutting used for single and double stacks used for the zero-field cooling experiment.

Two samples were developed: a single-layered stack, and a double-layered stack, as shown in Figure 4-5. The holder is made of brass with an external diameter of 90 mm. The middle tube outer diameter was 35 mm, and the inner diameter was 33 mm.

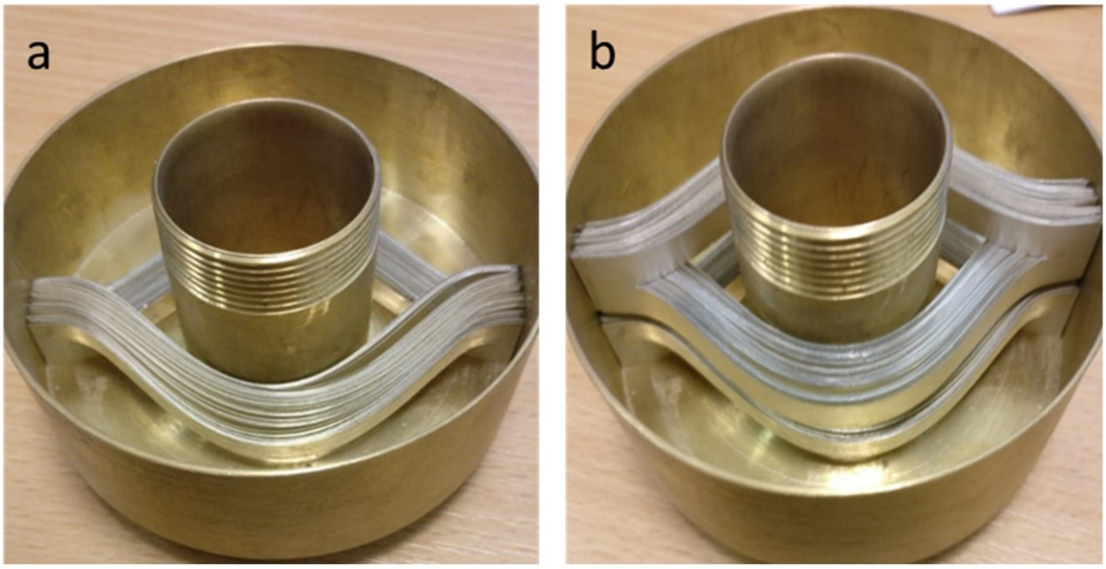

Figure 4-5. a) Single stack having 50 rings. b) Double stack of total 120 rings.

The samples were used without any support or impregnation. The single stack had 50 rings, and the double-stack had 120 rings, with 60 rings in each layer as the inner tube diameter was 35 mm, allowing the use of more than one hall sensor. I used LakeShore hall sensors HGT-2101. Figure 4-6 shows the geometry of the hall sensor and the terminal for current and voltage.

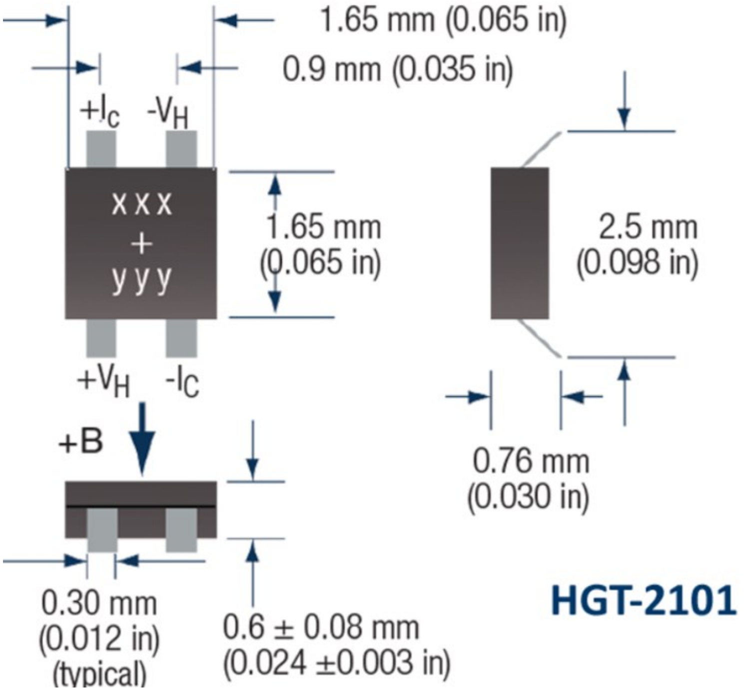

Figure 4-6. LakeShore HGT 2101 hall sensor used for measuring the tapped field in the middle of the ring magnet.

The current needed for the hall sensors was 1 mA. The hall sensors were calibrated for a 5 T external field at a cryogenic temperature of 30 K before using them in the experiment. Table 4-1 gives the measured sensitivities of the hall sensor after the calibration process. Five sensors were soldered onto a PCB. One in the middle was labelled as M, and the other four were at equal distance approximately 10 mm from the centre, and labelled as 1, 2, 3, 4 as shown in the figure below. A single constant current source was used to supply the current of 1 mA to all sensors, and they were connected in series. Every sensor had a separate voltage terminal connected to the data acquisition system in the experimental setup.

Figure 4-7 (a) shows the hall sensors mounted on PCB and the position of the PCB plate in a brass holder.

Table 4-1. Measured sensitivity of the HGT-2101 hall sensor

Hall sensor	**Sensitivity** (mT/V)
Middle (M)	4.84
Hall sensor 1 (H1)	4.54
Hall sensor 2 (H2)	4.91
Hall sensor 3 (H3)	4.86
Hall sensor 4 (H4)	5.03

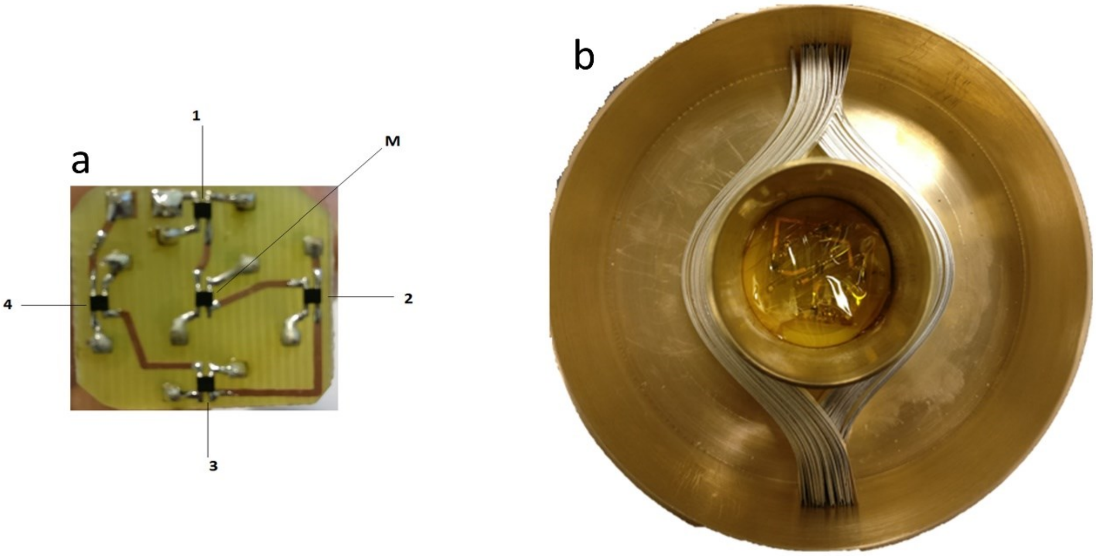

Figure 4-7. a) PCB with five soldered sensors labelled as 1, 2, 3, 4 and M. b) Hall sensor PCB position in the middle tube of the cup with a stack of HTS rings.

4.4 Shanghai superconductor sample

The critical current of both tapes, i.e. with silver and copper coats, was 500 A as provided by the manufacturer. Figure 4-8 a) shows the experimental setup used to obtain the critical current of the tape and Figure 4-8 b) shows the critical current data obtained from the experiment. Four probe method of DC conductivity [123] was used to measure the critical current of all the tapes. The experimentally measured critical current of copper-coated tape after cutting in the middle was around 450 A at 77K.

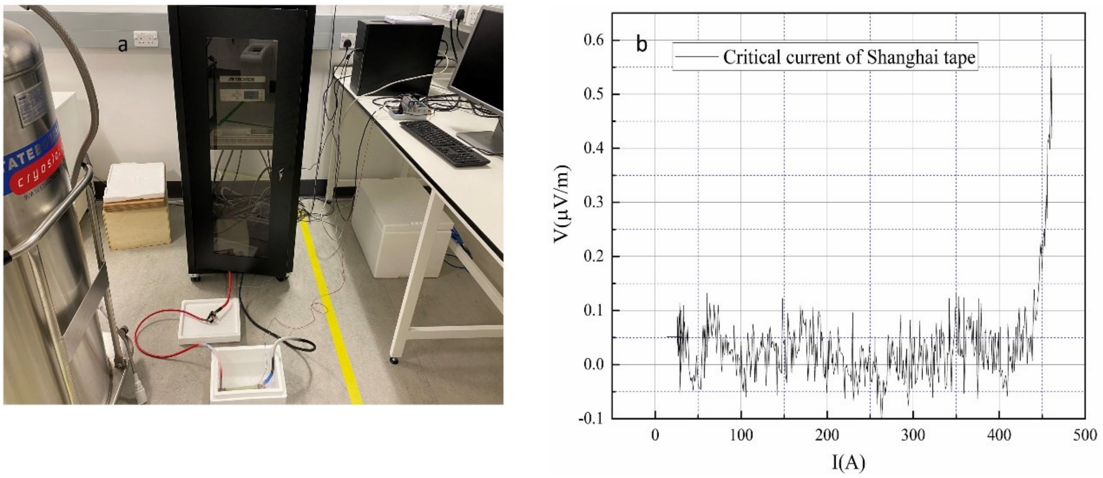

Figure 4-8. a) shows the experimental performed to measure the critical current of the Shanghai tape. b) The measured critical current of the copper-coated Shanghai tape after the slit was made in the middle of the tape.

The configuration of the tapes is shown in Figure 4-9 (a). One tape had a copper coating and the second tape had a silver coating. The thickness of the copper tape was 80 μm, and for silver tape it was 50 μm. Each sample was 88 mm in length. The laser cutter was used to cut the tape in the middle for 72 mm, and 8 mm of tape was left intact on both ends, as shown in Figure 4-9 (b) and (c). The maximum width of the tape manufactured by Shanghai superconductor is 10 mm. After cutting the width of each side of the ring was approximately 4.5 mm.

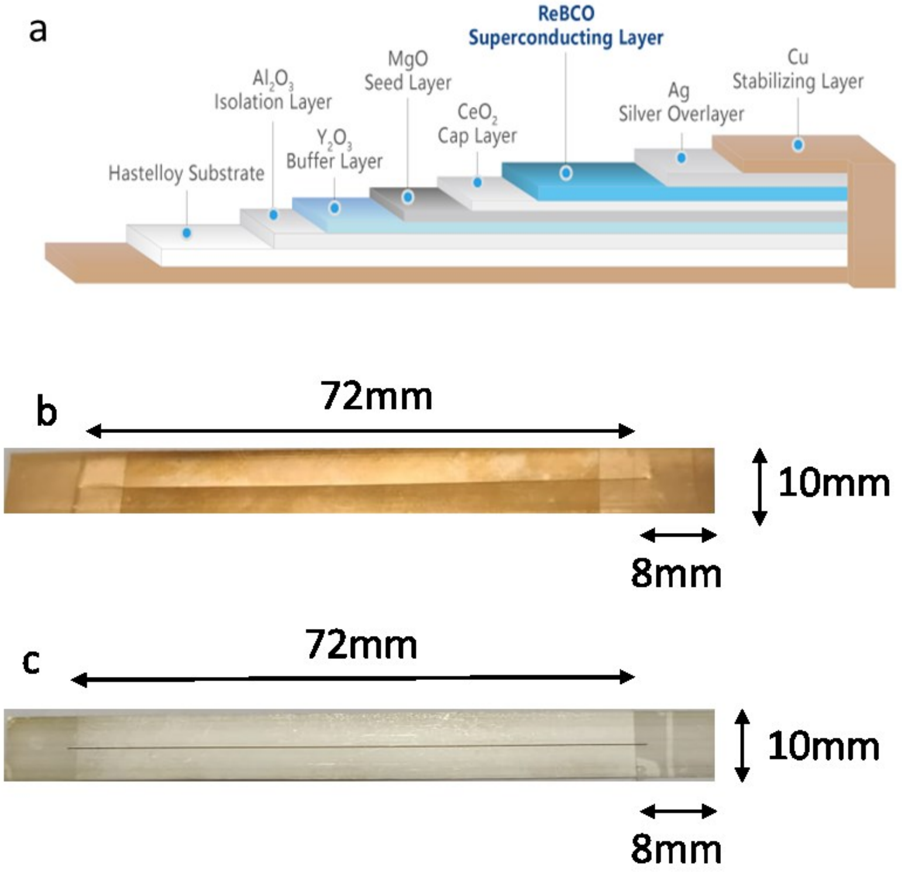

Figure 4-9. a) Schematic of Shanghai superconducting tapes [124] showing the components and dimensions of 10 mm wide Shanghai superconducting tapes from which rings were made. b) Copper-coated Shanghai superconducting 10 mm tape with dimensions of each ring after slitting. c) Silver-coated Shanghai superconducting 10 mm width tape with dimensions of the ring after slitting.

These rings were stacked together in two layers, and each stack contained 95 rings, as shown in Figure 4-10 (a) and (c). In the middle, there was a hollow tube in which a hall sensor was adjusted using a PTFE tube. In this experiment, a single hall sensor was used.

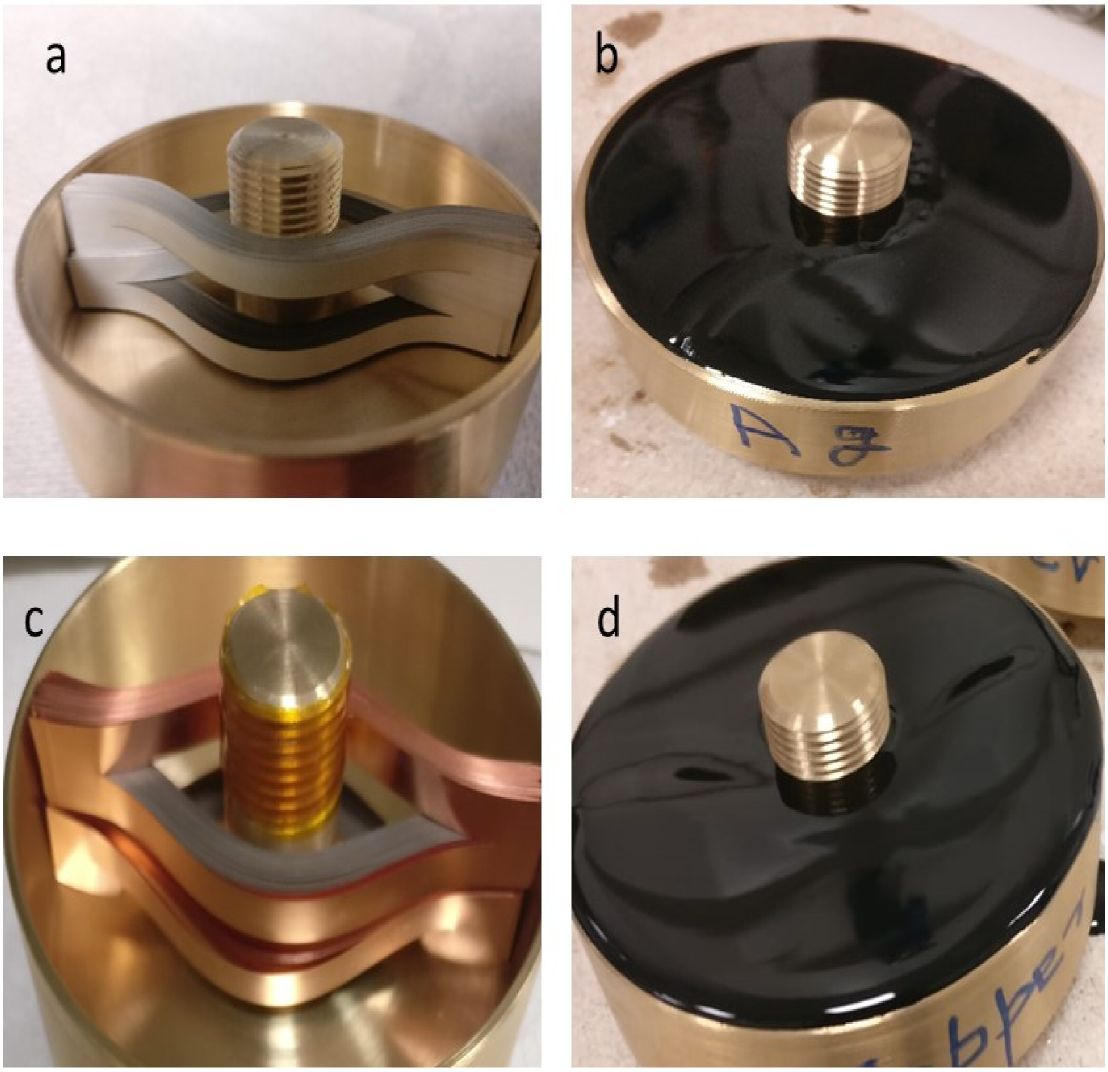

Figure 4-10. a) Silver tapes stacked. b) After Impregnation with Stycast 1250 FT of silver tapes. c) Copper tapes stacked. d) After Impregnation with Stycast 1250 FT of copper tapes.

Stycast is a two-component thermally conductive encapsulant that can be used with different catalysts. Its main features include a low coefficient of thermal expansion, and it is an excellent insulator of electricity. The proportion by weight used in our experiment was 100:7.5, 100 parts by weight of stycast and 7.5 by weight catalyst. The recommended temperature of operation is -65 to 105^0 C. After arranging the rings, epoxy Stycast 1250 FT black in colour along with catalyst 23 was used to impregnate the rings, as shown in Figure 4-10 (b) and (d). The thermal conductivity of this epoxy was 1.1 W/(m.K).

A calibrated cryogenic Hall sensor HHP-NP was used in the middle to measure the trapped field. It is a probe with a synthetic resin that covers it in the transverse direction, and the electrical system has high accuracy and lies parallel to the undersurface. Figure 4-11 shows the sensor used. The properties of the hall sensor are shown in Table 4-2.

Table 4-2. Parameters of HHP-Np hall sensor

Parameter (units)	**Values at 30 K**
Input current (mA)	20
Sensitivity (mV/T)	203.4
Sensitivity error up to 1T (%)	< 0.2
Change of sensitivity due to reversing of the magnetic field (%)	< 1
Operating temperature (K)	1.5-300
Overall dimension (w*l*h) (mm)	5.1*7*1.2

It has four wires, two for the input current and two for the voltage output. Green and black wires act as current control leads while red and orange are hall leads. The output of the sensor is polarity sensitive. If the positive terminal of the current supply is connected to the green colour current lead, and the vector of magnetic induction is perpendicular to the active surface area, then the red hall voltage terminal will experience a positive potential, and vice versa.

Figure 4-11. Calibrated cryogenic Hall sensor HHP-NP by Arepoc used in this experiment.

The Hall sensor was positioned in the middle of two layers, i.e. 10 mm from the bottom of the plate. The middle tube of the brass holders extended from the bottom side to fix the tube with the bolt. Threaded holes were made on the extended part at 120^0; in total three bolts were used to hold tight the PTFE tube in the middle.

4.5 Superpower Sample

The ring magnet design for the SuNAM and Shanghai superconducting tapes has already been discussed in sections 4.3 and 4.4. The fundamental design remains the same, but it differs in the structure of the tape. For this experiment, 12 mm tape from Superpower was used. Figure 4-12 shows the schematic of the Superpower tape used. It was SCS12050-AP tape with 20 um-copper stabilizer. The rated minimum critical current I_c was 520 A. The thickness of the tape was < 0.1 mm. It had a silver overlayer with a thickness of approximately 3.6 microns. The tensile strength of this tape was >550 MPa. Each ring sample was 88 mm in length, and a laser cutter was used to cut the tape in the middle. The centre cut was 72 mm, and 8 mm tape was left intact on both sides.

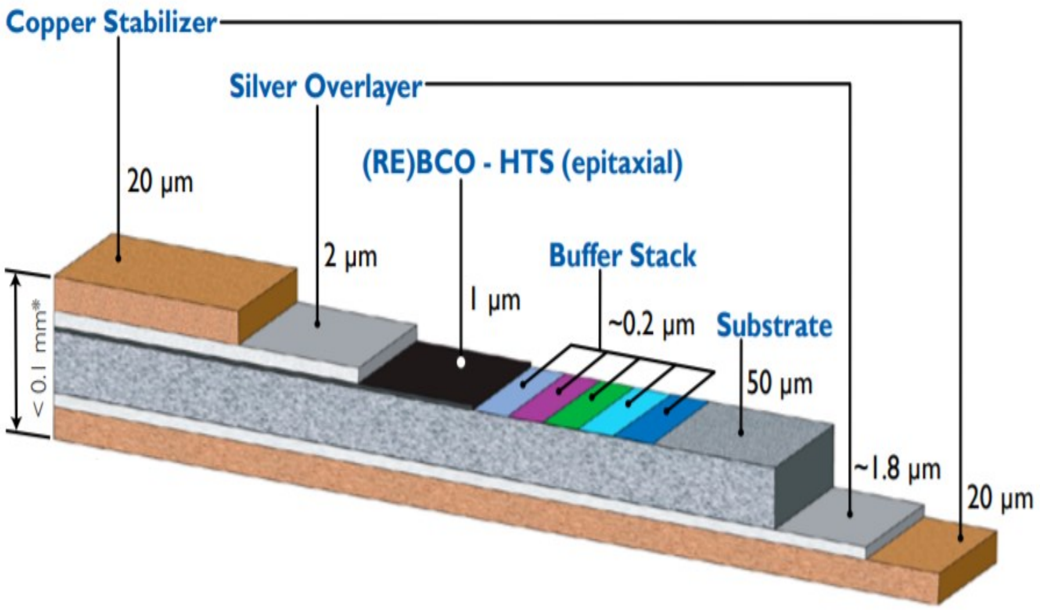

Figure 4-12. Schematic showing the components and dimensions of 12 mm wide Superpower 2G HTS wire from which the rings were made [125]

Figure 4-13 (a) shows the schematic with the dimensions of the tape after cutting. The single ring made from the slitted tape is shown in Figure 4-13 (b). Figure 4-13 (c) shows the sample prepared for critical current measurement. Figure 4-13 (d) shows the measured critical current of the tape after splitting, which was around 490 A at 77 K. There was a 6% reduction in the critical current of the tape after splitting.

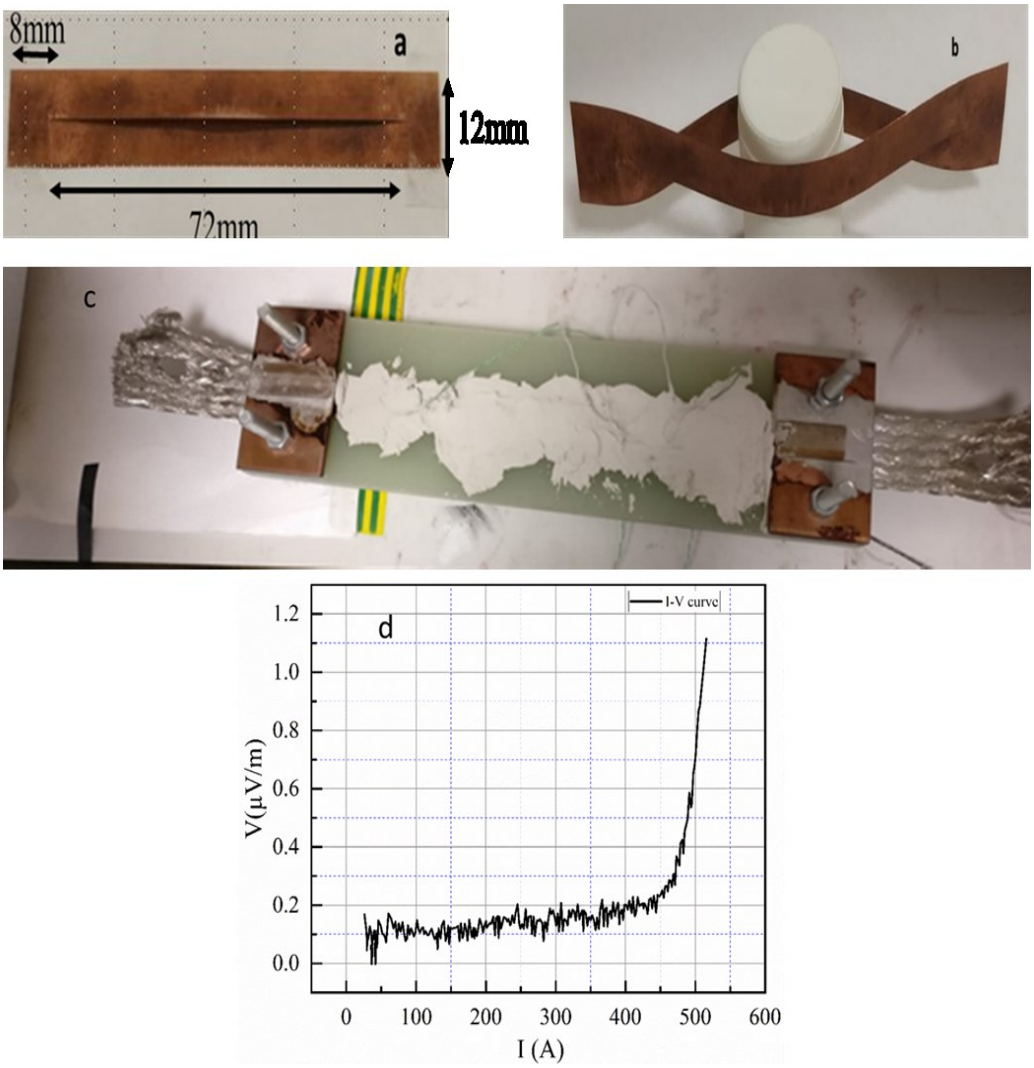

Figure 4-13. (a) Schematic of the slitted tape. (b) Single ring made from the slitted tape. (c) A sample prepared for critical current measurement (d) Critical current of the tape after splitting

100 HTS rings made from 2G HTS coated conductors (CC) were stacked together to form a single stack. There were two stacks in our ring magnet. The inner tube 20 mm in diameter. The brass cup was 90 mm in the outer diameter. The inner diameter of the cup was 86 mm, where rings were stacked. Six holes were created by using brass tubes with an outer diameter of 10 mm. These tubes enable the proper flow of liquid helium through the sample. This structure provides better cooling, which was proved during the zero-field cooling experiment of Shanghai superconducting magnets. After stacking the rings,

the brass cup shows asymmetric geometry. The closed side of the magnet sees two HTS layers closely stacked together while the opened side of the magnet shows a 12 mm gap between the two sides. This configuration is shown in Figure 4-14 (a) and (b).

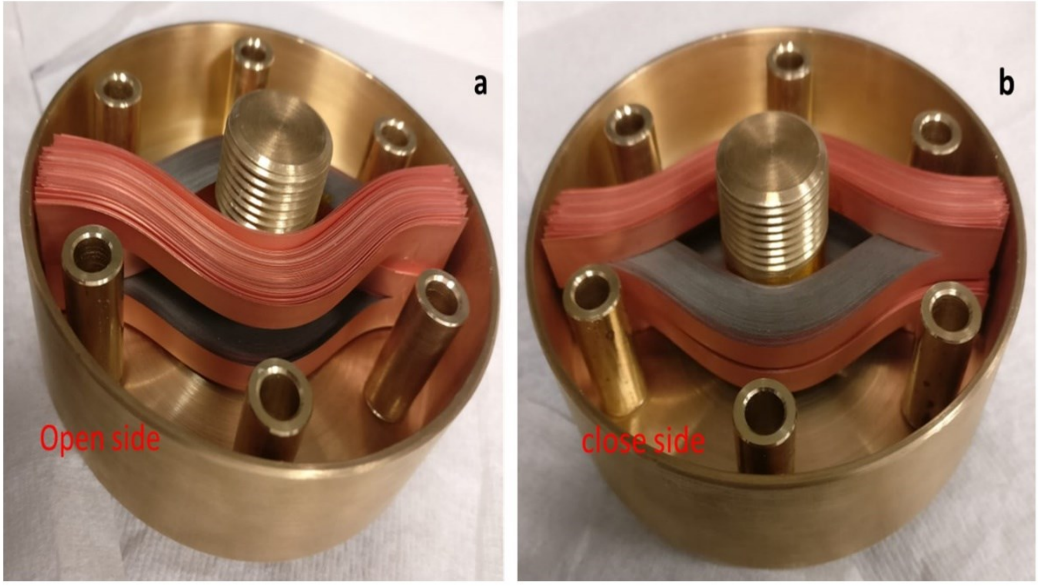

Figure 4-14. (a) and (b) shows the double-layered ring magnet in a brass holder. The opened side and the closed side are marked in the figure.

These ring magnets require impregnation to avoid displacement in the holder. In addition, the epoxy has a degrading impact on the performance of the ring magnets. The main purpose for impregnation in my experiment is to prevent the movement of rings without affecting the cooling/heating of the sample. For electronics devices, phase change material (PCM) provides an effective heat sink with better thermal performance [126]. Ideal PCM has high thermal conductivity, high specific heat and density, durability for the longer term, and dependable freezing behaviour. There are many classes of phase changing materials, but paraffin waxes are the most common and widely used. Paraffin impregnation effectively avoids HTS coil degradation [127].

Paraffin wax has large latent heat values $(145 - 240\ kJ/kg)$ with chemical stability. The only challenge for usin paraffin wax for impregnating my ring magnet was its low thermal conductivity (below $0.1\ W/m.K$). Paraffin wax with a melting temperature of 55^0 C was used to avoid damaging the slitted rings with high temperature. It was decided to use ceramic fillers to enhance the thermal conductivity of the paraffin wax. Ceramic fillers with particle size of less than 10 microns were chosen, because of their low density, low thermal expansion, high thermal conductivity, superior resistivity against thermal shock, and relatively low cost [128]. The concentration of fillers (more than 3%) can improve the thermal conductivity by more than 18% and thermal responsivity by more than 28% [129],[130]. It improves the heat transfer to and from the paraffin wax and sample cooled down to 25K. The sample after impregnation with the paraffin wax mixture is shown in Figure 4-15.

Figure 4-15. Impregnation of the ring magnet sample with a mixture of paraffin wax.

Three hall sensors (LakeShore HGT-2101) were fixed on a double-sided PCB board as shown in Figure 4-16. The hall sensors were labelled as H3 at the centre (marked as M), H4 (marked as 1) 4.5 mm from the centre towards the closed side and H2 (marked as 2) is 4.5 mm from the centre towards the opened side.

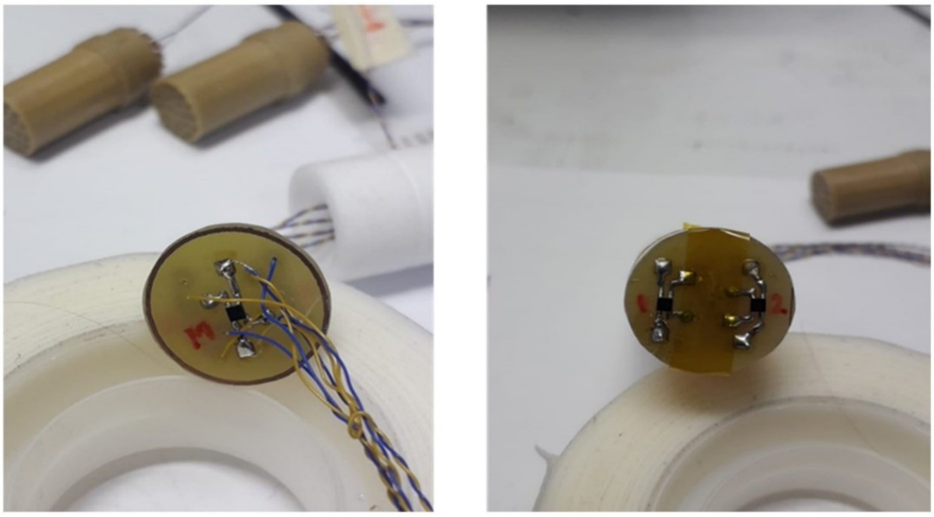

Figure 4-16. PCB double-sided board with three sensors. Two on the upper side marked as 1 and 2, will be referred to in the text as H4 and H2, respectively, and the one on the lower side is marked as M but will be referred as H3 in the text.

4.6 Conclusion

This chapter explains the different manufacturing processes for producing superconducting tapes. It also explains the general procedure to create a ring magnet which is followed throughout this thesis. The magnets, created using the superconducting tapes provided by SuNAM, Shanghai superconductor and SuperPower, are explained along with the structural difference between the magnets used. The SuNAM sample was used without impregnation, and the Shanghai superconductor sample was impregnated using epoxy Stycast 1250 FT. A mixture of paraffin wax with ceramic fillers was prepared to impregnate the SuperPower magnet. The experimental setup and results of these magnets are discussed in chapter 5.

5 FIELD COOLING AND ZERO-FIELD COOLING EXPERIMENT RESULTS

This chapter explains the experimental setup used at the University of Cambridge using a 12 T 100 mm bore solenoid type VTI magnet. It also gives a brief introduction to the acquisition system used during the experiment. Experimental measurements for field cooling and zero-field cooling on the ring magnets prepared with and without impregnation were performed, proving that these ring magnets are capable of trapping high magnetic fields.

5.1 Introduction and Overview

In order to validate the modelling results of chapter 3, it was necessary to perform experiments. There are three different methods to magnetize the superconducting magnets. These are summarised as below.

- Field Cooling

In this process, the sample is cooled in the presence of an external magnetic field. In practice, the temperature is decreased to 100 K in the absence of the field. This temperature depends on the critical temperature of the material used. For my sample, the critical temperature was 92 K. Once the desired temperature is achieved, the external magnetic field is reduced to zero at a specific rate, which depends on the shape of the sample to avoid flux jumps and heat fluctuations.

- Zero Field Cooling

In this process, the magnet is first cooled to the desired temperature, then the external magnetic field is applied.

These techniques are well established for the magnetization of superconducting magnets. Table 5-1 shows the summary of the system parameters and an overview of the system shown in Figure 5-1. The system used was supplied by Oxford Innovative Cryogenic Engineering to the University of Cambridge. The magnet was a 12 T cryogen-free vertical solenoid fitted with a variable temperature insert (VTI). The system was a cryo-cooler operated with a helium gas-filled cooling loop.

Table 5-1: Summary of the key parameters of the system used for the experiment

Parameter	**Explanation**
System type	Dry 1.5 K
Cooling medium	Helium gas
Cryostat sample space	100 mm
Maximum test field	11.8 T at 2.2 K
Stages of cooling	2
Inductance	42.9 H
Rated current at 11.8 T at 4.2 K	137.8 A
Field to current ratio	856.5 Gauss/Amp
Field homogeneity	0.05% over 1 cm DSV 0.5% over 4 cm DSV
Modes of operations	static, dynamic, one-shot

The insert was sealed inside the cryostat. The sample was attached to the copper plate at the end of the insert. The cooling was provided indirectly by the conduction of heat by helium gas. This gas conduction cooling provided more flexibility in terms of sample size and shape, and its performance was better than a conduction-cooled design [131]. In the lateer, the sample has to be rigidly attached directly to the cold head.

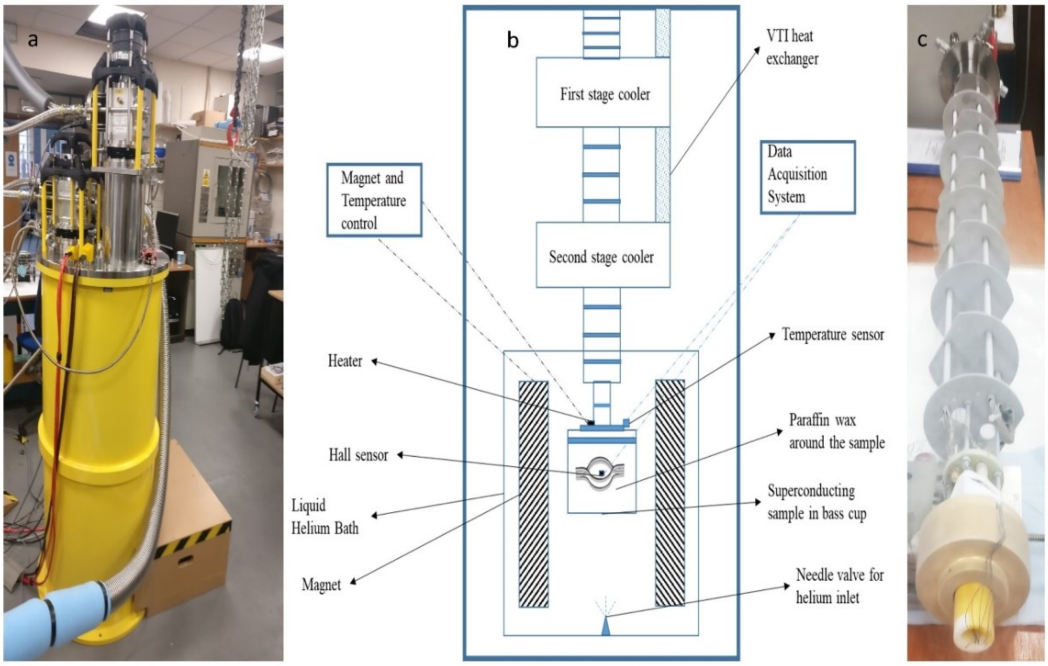

Figure 5-1. a) shows the magnet system for field cooling and zero-field cooling. It is a 100 mm bore, 12 T high field magnet at Cambridge University. b) Schematic illustrating the various parts of the system. The bottom part contains the sample holder and temperature and hall sensors. c) Probe to which the magnet, hall sensor, temperature sensor and heater were attached.

The solenoid temperature should be kept below 4 K at all times, which was monitored as the second stage temperature. The magnetic field should not be ramped up until the temperature is below 4.5 K, and should be removed if the magnet temperature is around 5.5 K. The magnet leads were also made of high-temperature superconductors. The first stage temperature should be kept below 100 K; if it increases beyond 100 K, then the magnet becomes de-energised.

The overall experimental setup is summarised in Figure 5-1 (b). It is a dry system with a sample space of 100 mm, the external field capacity of 12 T for HTS samples testing at high currents. It is a fully insulated cryostat with an Aluminium radiation shield, and this shield is linked to a first stage cold head whose temperature is approximately 50 K. This radiation shield along with the cryostat vacuum and super insulation minimises the heat losses in the sample space due to conduction and radiation heat loads. The variable temperature insert (VTI), shares the same vacuum space with the cryostat. The cryostat consists of two stages. The VTI was inserted into the bore of the superconducting magnet. The sample was attached to the cold plate at the end of this VTI, which connected the two-stage cooler to the sample. The VTI was dynamic which provides better thermal response for sample thermal stability.

There are two modes of operation for the VTI: continuous flow operation and single-shot operation. During the continuous flow operation, the temperature of the sample can be controlled continuously at a required temperature. It is done by continuous circulation of helium gas with the help of a circulation pump and the needle valve of the VTI through which gas flow is regulated. In single-shot operation, the lowest temperature is achieved by creating a liquid helium reservoir for heat exchange in the VTI. Once the helium reservoir is created, the needle valve is switched off, and the sample is cooled down at the lowest pressure to the lowest temperature. A pressure of less than 50 mbar is required for the whole cooling process of the sample.

Helium was used as the medium of conduction cooling. Helium was injected to the sample chamber through the needle chamber. Once the sample cooled down to the required temperature, the system could be switched from dynamic to static sample space. This mode helps to eliminate any direct contact between the sample space and the flow of helium. The helium gas exhaust is pumped outside the sample space tube from the heat exchange of the VTI. The sample cooling is controlled by the amount of exchange gas in the sample space. The probe with a superconducting sample can be assessed without warming up of the cryostat, which reduces the cooling time of the HTS sample.

5.2 Data acquisition

Figure 5-2. a) Data acquisition system, power supplies for sensors, and LakeShore controller for the heater. b) CRYOMAGNETICS power supply and LakeShore temperature controller for monitoring the temperature of the sample and heat exchangers.

Figure 5-2 shows the data acquisition and power supply along with temperature control units. The measurement and magnetization data was interfaced with a computer via a Keithley, 3706 system switch/ multimeter capable of over 14000 readings per second. LabVIEW was used to acquire data from the sensors. A Keithley 2602 source meter was used to provide current to the hall sensors. The currents of 20 mA and 1mA were used for the hall sensors. An INFICON VGC 501 single-channel vacuum pressure controller was used to monitor the pressure of the cryostat, and the pressure was maintained at 2.97 mBar. A LakeShore 336 Cryogenic temperature controller was used to monitor the temperature of the probe, top heat exchanger, static heat exchanger, and dynamic heat exchanger. A LakeShore 340 temperature controller was used to control the heater attached to the copper plater to which sample holder was attached. A

CRYOMAGNETICS, INC, Model 4G-100 superconducting magnet power supply is used to supply current to the external field magnet. LakeShore wire WCT-YB-34-100 is used to connect the PCB mounted sensors to the connectors. Figure 5-3 shows the copper plate to which magnet was attached, and also the position of the heater and the connectors used for connections. The holder containing the HTS ring magnet attached to the copper plate also shown in Figure 5-3 (a).

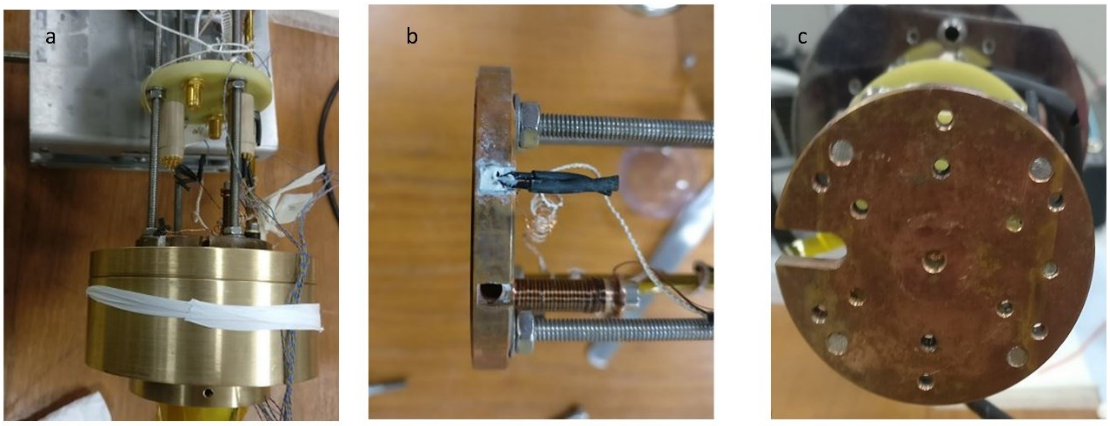

Figure 5-3. a) Attached sample holder to the copper plate, wire and connectors for connections to the data acquisition system. b) Attached heater to the copper plate. c) An outlook of the copper plate to which ring magnet was attached.

For my experiments, tapes from three different suppliers, SuNAM, Shangahi superconductors and Superpower were used.

5.3 Zero Field Cooling of SuNAM sample

Two samples were prepared using SuNAM tapes. One sample was a single stack of rings and the second sample was a double stack of rings. The original plan was to perform both field cooling and zero-field cooling on the magnet. The experiments were performed at 25 K. First, the single stack sample was magnetized. The inner diameter of the ring stack was 35 mm. Five sensors were placed in the middle tube, as shown in

Figure 4-7 (a). The cup was made of brass, and the outer diameter of brass was 90 mm. The bore of the magnet was 100 mm. The sample was without any impregnation. The height of the cup was 30 mm.

5.3.1 Single Stack Magnet

The cup was connected to the cold head and placed in the magnet for magnetization. The single stack had 50 rings. The 2D model was used to predict the trapped field of the single-stack. In the model, the trapped field was noted in the middle. Both field cooling and zero-field cooling were performed in COMSOL, and the experiment was performed to validate the modelling results. The modelling results are shown in Figure 5-4. From modelling, it was predicted that a single stack ring magnet of 50 rings could trap a field of 0.591 T. The model used was the axis-symmetric 2D model, and the values were taken at the centre. The model was already explained in section 3.2.

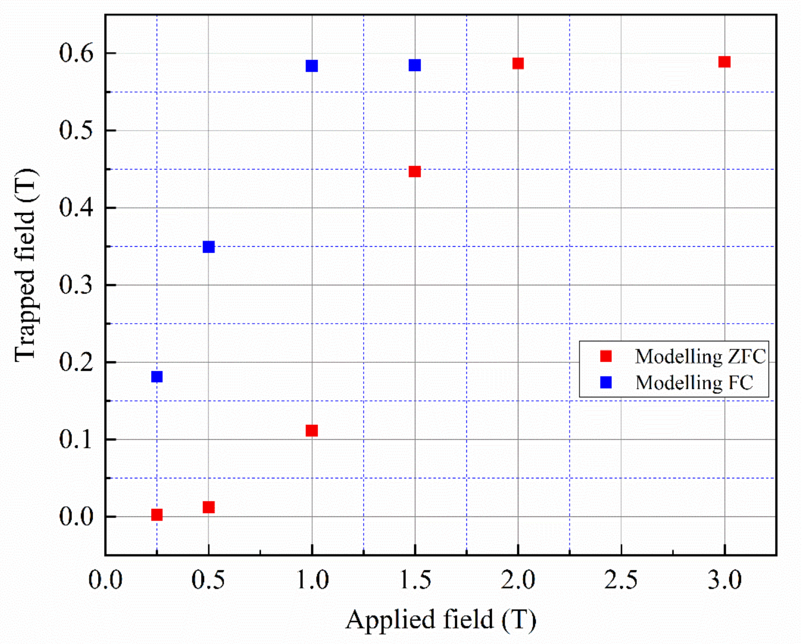

Figure 5-4. Modelling result for 50 rings single stack SuNAM tapes with 35 mm internal diameter. The trapped field achieved for both ZFC and FC is 0.591 T.

To validate this modelling result, ZFC was performed experimentally. The experimental results are shown in Figure 5-5. The applied field was 1 T, 2 T, 3 T and 4 T. The time-lapse between the two consecutive applied field was 30 mins. A mismatch was noted between the experimental and modelling results. The experimental result showed that the trapped field was just around 0.2-0.3 T which is less than 50 % of the expected trapped field. It was further noted that once the magnet was fully saturated, further applying higher external magnetic fields slightly decreased the trapped field. In theory, if the expected trapped field is around 0.571 T, then the external field required to saturate the rings is around 1.5 T. Figure 5-5 shows the experiment results and Figure 5-5 (b) shows the expanded trapped field values.

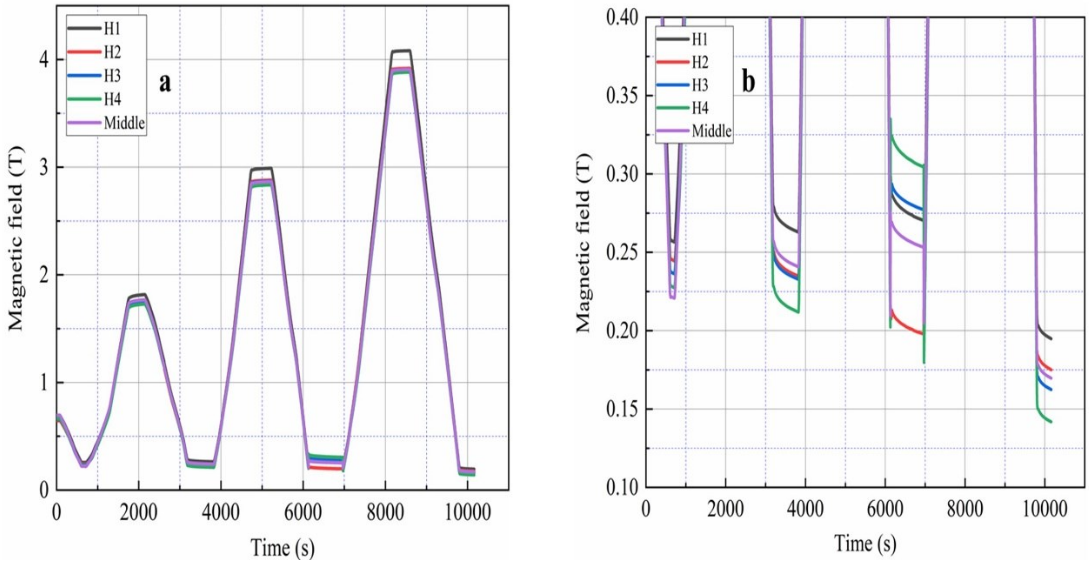

Figure 5-5. Zero field cooling experiment results. The trapped field is around 0.24 T. The applied is 1 T, 2 T, 3 T and 4 T. (a) Original experiment result. (b) expanded trapped field results.

Further investigation showed that, during magnetization, the stack of the ring changed its position vertically, ao that the PCB sensors were no longer positioned in the middle of the rings horizontally. Also, by analysing the data obtained from the hall sensors, it was noted that not only was the single-stack ring displaced vertically but it also rotated in the brass cup. It was expected that the H2 and H4 sensors should have the highest trapped field values as they were placed near the loop sides of the ring, while H1 and H3 should have the lowest trapped field as the distance from loop sides is more than H2 and H4. However, all the sensors were changing the values during every new applied external field.

Figure 5-6 shows the final position of the stack when opened after magnetization. After this experiment, the rings were no longer superconducting. Besides, the literature provided by the manufacturer explains they should be handled with care and should be saved from moisture. These rings were machined mechanically, and they were placed in a brass cup for more than a week before the experiment was performed. This might might had some degrading impact on the critical current of the tapes.

Figure 5-6. Displacement of the ring stack from its original position. Single stack showing an uplift of rings, expansion and pressure at the ends.

5.3.2 Double stack magnet

A double stack magnet with 100 rings was prepared. Each stack contained 50 rings. From the previous experiment with the single-stack ring magnet, it was concluded that the cup size should be according to the height of the ring magnet. As the height was 30 mm and the height of the double stack ring was around 27 mm, it was expected that it would not have any uplift from its position and it was decided to carry on the experiment. The modelling results were computed to estimate the trapped field for a double-stack magnet at the centre of the ring magnet. The modelling result for a double-stack ring magnet is shown in Figure 5-7. The modelling result shows that it can trap a field of 1.08 T.

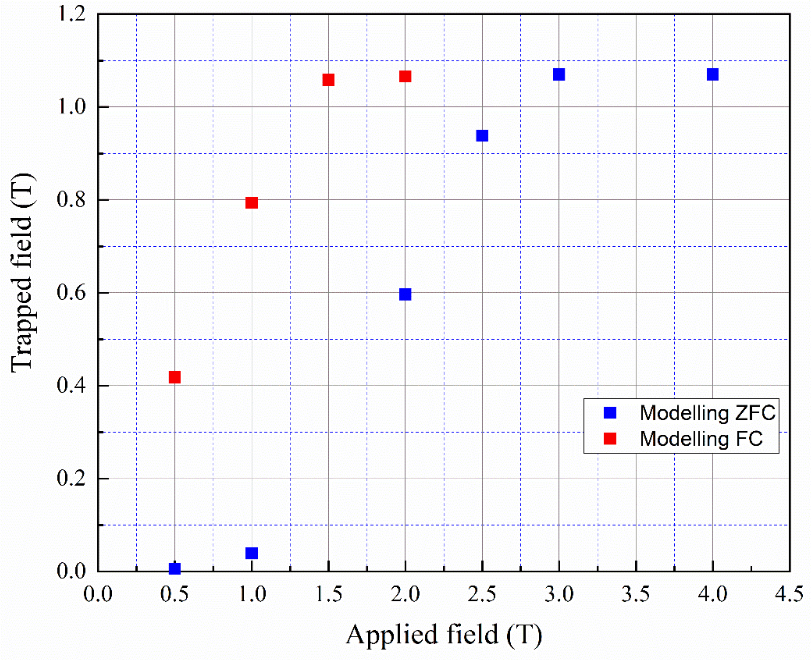

Figure 5-7. Modelling zero-field cooling and field cooling results for double-stack ring magnet. Modelling shows a trapped field of 1.06 T.

For validation of modelling results, a ZFC experiment was performed on a double-stack 100 rings magnet made from SuNAM tapes. The experiment result is shown in Figure 5-8. The applied field was 1 T, 2 T, 3 T, 4 T and 5 T. The duration between the two consecutive fields was 30 mins. In the double-stack configuration, the two ring stacks overlapped on one side, named as the closed side, while there is a separation on the opposite side termed as the opened side. The separation between the open side loops was approximately 12 mm, which is equal to the width of the tape. Here H4 was placed near the overlapping layer, and H2 was near the separated ends of the rings. Figure 5-8 (a) shows the experiment results for the double-stack ring magnet. Figure 5-8 (b) shows the expanded trapped field part.

It was noted that our magnet had an asymmetric trapped field distribution. The maximum trapped field was noted near the overlapping layers, and the lowest was recorded near the open side. The trapped field near the edges was approximately the same, as shown by sensors H1 and H3. During magnetization, a small movement was noticed near the edges, which made the trapped field values change. It was also noted that once the magnet was fully saturated further increasing the external field reduced the trapped field. The experiment result for the double-stack ring magnet did not match the modelling result. The experiment results showed that the trapped field in the middle was around 0.67 T, but the modelling result prediction was around 1.08 T. The difference is around 40%.

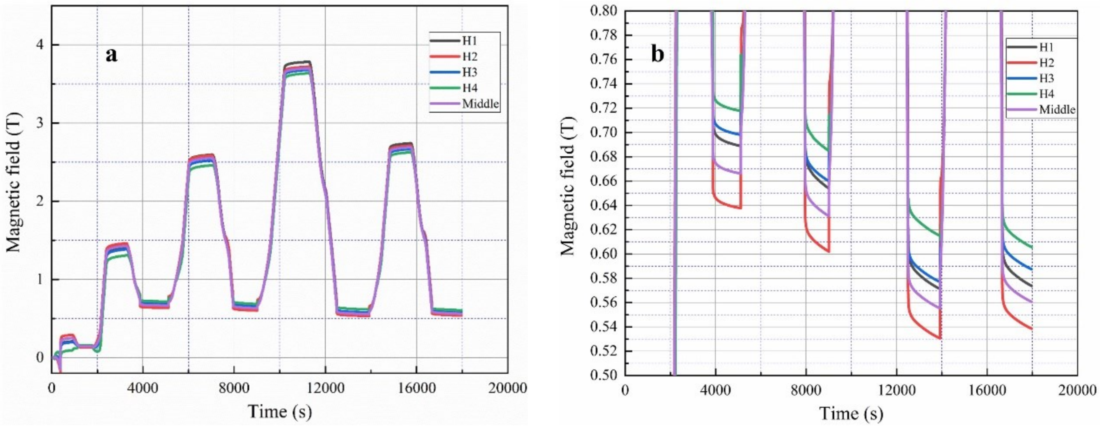

Figure 5-8. Experiment result for a SuNAM double stack ring magnet. The applied fields were 1 T, 2 T, 3 T, 4 T and 3 T. (a) shows the actual data for ZFC while (b) shows the expanded trapped field results.

This was the first experiment performed to measure the trapped field in the double-stack ring magnet, and although it did not match the model, it did predict the asymmetric field distribution in our new ring magnet. The primary purpose of the experiment was to validate the modelling with the experiment results. More than one sensor was used to predict the field distribution in the single stack and double stacked ring magnets so that the 3D model could be created according to the actual geometry of the ring magnet. Investigation showed that we need proper encapsulation or modified sample holder matching the dimensions of the rings. Also, the rings should be handled with care while opening the tapes, which should be done in a moisture-free environment. After the completion of the experiment, the rings were tested for critical current I_c ; the superconducting tapes were not superconducting anymore. The double-stack ring magnet results were improved because of the little vertical displacement area for the rings. The changing values at the edges show that it experienced some movement, and this needed to be fixed. As no encapsulation was being used, so the same brass cup was used for both samples. As already explained in section 2.2.1, the trapped field of the rings depends on the diameter of the rings. Larger diameters will have lower trapped fields. It was decided to reduce the cup middle tube diameter and to use epoxy to encapsulate the ring to restrict the displacement of the rings. The field cooling experiment was not possible because the rings were not superconducting after the experiment. From the literature, as I came to know, to avoid conductor movement, some impregnation should be used, which forms a kink in the conductor body [127]. For this purpose, it was decided to use Stycast 1250 FT epoxy with catalyst 23 for the impregnation of our next magnet sample.

5.4 Field and zero-field cooling of Shanghai Superconducting tapes

YBCO coated conductors of 10 mm width were used to make a magnet with persistent current rings. The maximum trapped of 1.5 T has been achieved, and flux creep was measured and was found to be logarithmic. This is the highest trapped field achieved in persistent current loop rings at 30 K by using zero-field cooling magnetization. Zero Field cooling shows three distinctive zones, which were explained by the COMSOL model based on the Bean model.

The full penetration field depends on the critical current density of the superconductor and the geometry of the sample. The origin lies at the geometrical centre of the ring, and an assumed uniform magnetic field was applied in a perpendicular direction so that the superconducting magnet did not affect the external field source. It was considered that the induced current would flow in an angular direction because of the cylindrical symmetry. During zero-field cooling, we observed several phases: a shielding phase, which is the Meissner phase and prevents any penetration of magnetic flux; a linear phase, in which there is a partial penetration of the magnetic flux along with the flow of shielding currents in the regions where no flux was penetrating; and finally, the saturated region, which is due to complete penetration of the magnetic flux in the superconducting sample. In ring magnets, the penetration of the magnetic field occurred simultaneously from the outer rings as well as from the inner rings.

The magnet made from Shanghai superconductor tapes is shown in Figure 4-10 (a) and (c) and the ring magnets after impregnation are shown in Figure 4-10 (b) and (d). A calibrated cryogenic hall sensor HHP-NP was used in the middle to measure the trapped field. The position of the hall sensor was in the middle of two layers, 10 mm from the bottom of the plate. The ring magnet sample made from copper-coated Shanghai superconducting tapes was named as magnet 1, and the magnet made from silver-coated Shanghai superconducting tape is named as magnet 2. First, the COMSOL 2D axis-symmetric model was created to estimate the trapped field in the ring magnet, as already explained in section 3.2. The modelling result showed that these magnets could trap approximately 1.7 T of the magnetic field. The modelling results for both field cooling and zero-field cooling are shown in Figure 5-9. As both the copper-coated and silver-coated tapes have the same critical current, so the expected trapped field for both magnet will be the same.

The first field cooling experiment was performed on a ring magnet made from copper-coated Shanghai superconductor. Field cooling of a ring magnet is similar to the bulk superconductor and stacks of tapes [92]. The field trapped by the magnet increases linearly with the changing amplitude of the applied field until the magnet is fully penetrated. Further increase in the applied field does not affect the trapped field, and the ring magnet has entered the saturation zone. So in field cooling, we can say there are two zones: linear and saturation. In theory, the HTS ring magnet trapped field is affected by both the inner diameter and the width of the tape. The larger the inner diameter, the smaller will be the trapped field. With wider tapes, the trapped field will also increase.

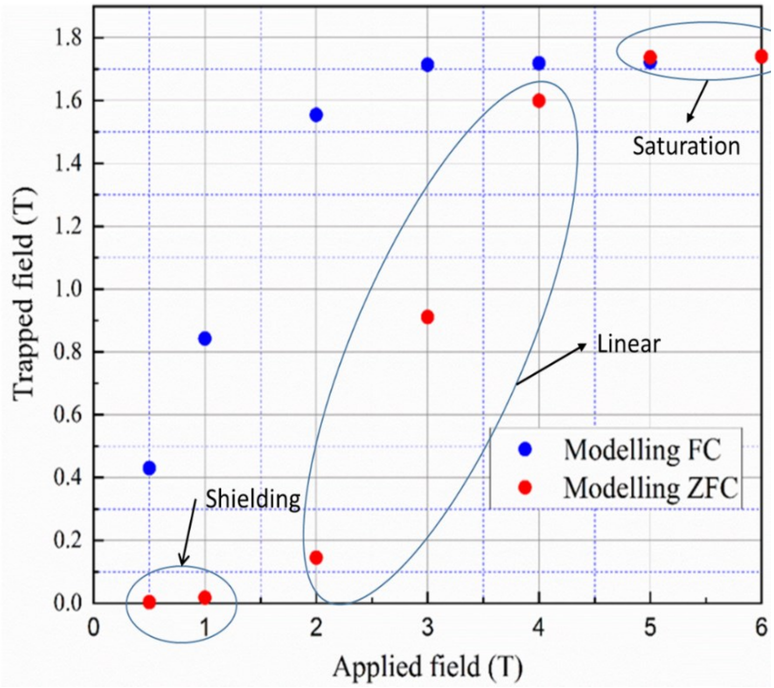

Figure 5-9. Modelling field cooling and zero-field cooling results for Shanghai superconducting tapes. Circles show the three zones: shielding, linear, and saturation zone. A final trapped field of 1.7 T was estimated from the model for both field cooling and zero-field cooling experiments.

During the field cooling, first, the temperature of the sample was reduced to 110 K without applying the external magnetic field. Further reduction in temperature was carried out in the presence of an external magnetic field of 6T. During cooling down of the magnet, it was noticed that further reduction in temperature beyond 40 K for the magnet was not allowed by the system, so the field cooling was performed at 40 K. Figure 5-10 also shows the temperature during the field cooling process along with the decreasing magnetic field, which clearly shows that the temperature was kept constant at 40 K during the whole field cooling process. The external field was decreased at a rate of 0.15 T/min.

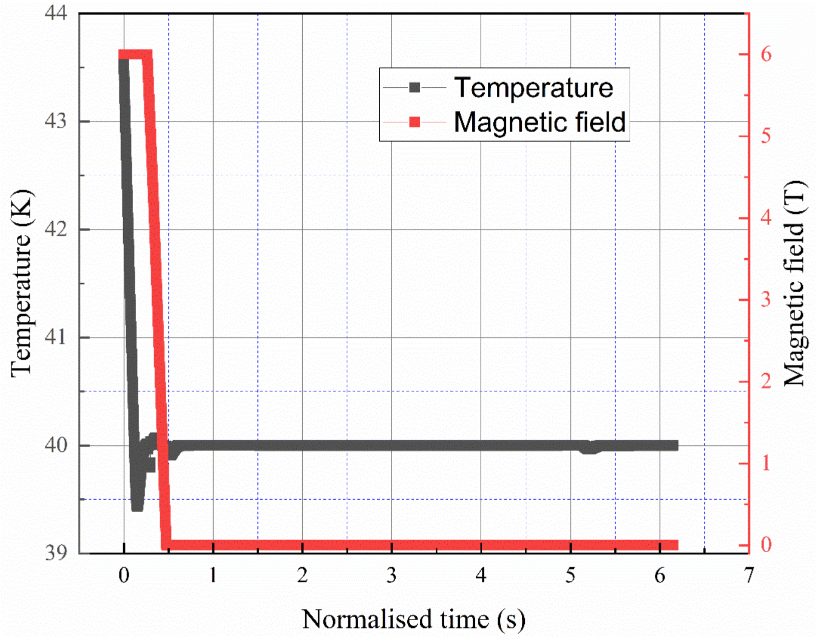

Figure 5-10.Temperature and changing magnetic field during the process of field cooling.

Figure 5-11 shows that the trapped field during the experiment was approximately 1.19 T. This mismatch was due to the temperature difference between the modelling and experiment. The modelling results were obtained for 30 K, while the field cooling was performed at 40 K. The model was redefined for 40 K by changing the critical current to the desired value. The desired value was obtained from the database [91] available online. The field cooling model results showed a trapped field of approximately 1.4 T. The difference was around 21 % between the modelling and the experimental results.

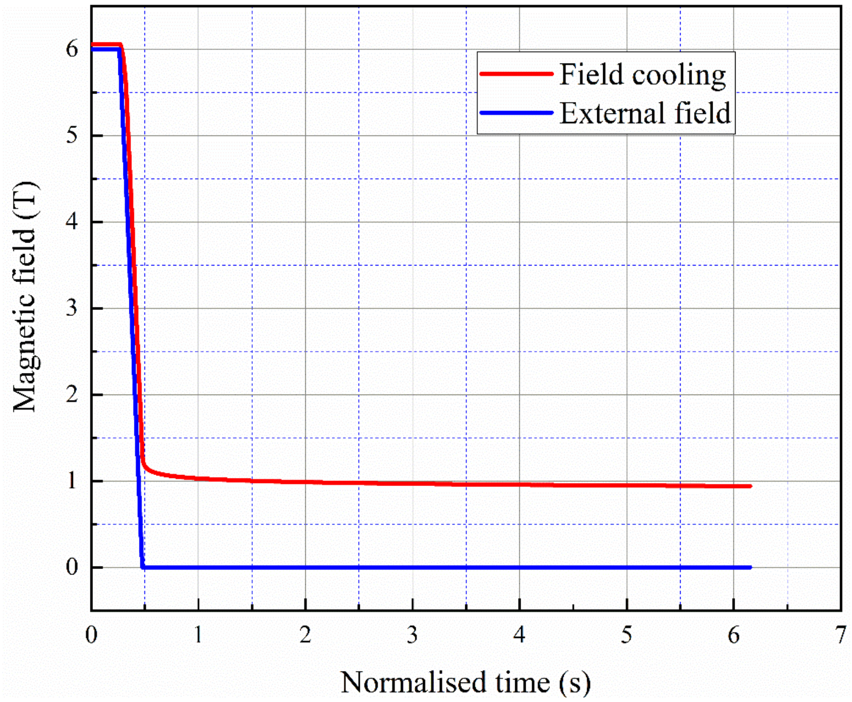

Figure 5-11. A trapped field during the process of field cooling of a magnet made from copper-coated Shanghai superconducting tapes.

5.4.1.1 Flux creep

Flux creep of the trapped field was noted for more than 14 hours and was found to be logarithmic. Flux creep of the magnet 1 after field cooling magnetization is shown in Figure 5-12. Flux creep is the relaxation of trapped magnetization in high-temperature superconductors and is an important factor which limits the current carrying capacity of these superconductors. Flux creep is due to the finite resistivity when the current density is lower than the critical current density of the superconductor $J < J_c$, caused by thermal fluxons jumping between the neighbouring pinning positions. Due to the Lorentz force, the magnetic flux experiences a directional movement and dissipation, which decays the induced magnetization currents. In the region $J < J_c$, a short time decay is universal and has two stages. The initial stage is non-logarithmic, and the second stage is logarithmic. During the first stage, magnetic flux transients redistribute over the cross-section of the magnet, their duration determined by macroscopic quantities such as sample size, flux creep rate, and magnetic ramp rate. The second stage, which is logarithmic, corresponds to the sample size, the time constant, and the relationship between the voltage and critical current density of the sample [132].

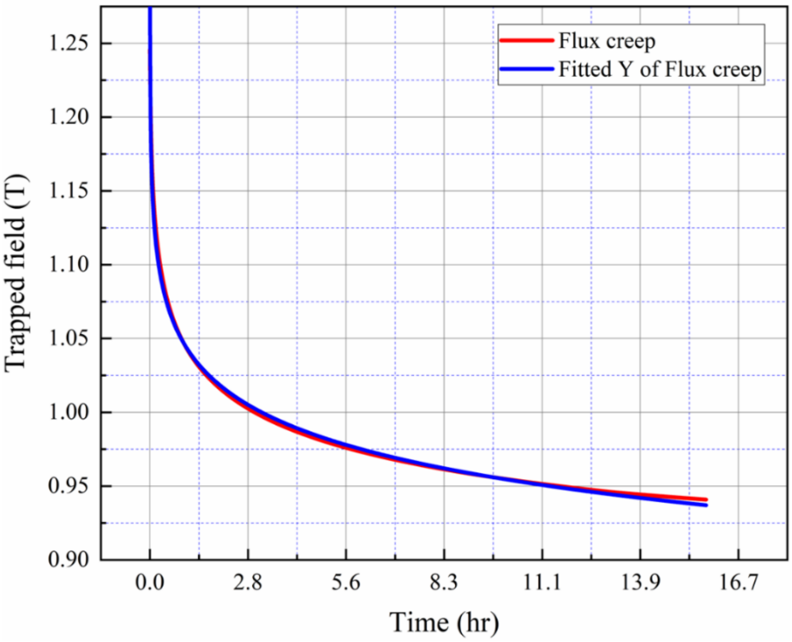

Figure 5-12. Flux creep of sample 1 after field cooling magnetization noted for more than 14 hours.

The flux creep expression was obtained by curve fitting the original data and defined in terms of coefficients a, b, and c, as also shown in Figure 5-12. The red line is the original flux creep obtained from the experiment while the curve filling obtains the blue curve. The fitted curve has an accuracy of up to 95%. The expression obtained is:

$$y = a - b^{*}\ln(x + c) \qquad 5\text{-}1$$

where a is 1.3663, b is 0.03924, and c is 7.61283. Here, x is the time and expressed in seconds. The adjustment for this curve is $\pm 2.18503e^{-5}$.

5.4.2 Zero field cooling of sample 1 and sample 2

As the temperature was not reduced to 30 K, it was decided to perform zero-field cooling. As in zero-field cooling, the temperature was decreased in the absence of the external field, so it was expected that the temperature of 30 K could be achieved. Before performing the zero-field cooling, six holes were drilled in the solid epoxy to make the cooling process a bit quicker. Figure 5-13 shows the sample holder after the drilling of holes. Zero field cooling was performed on both sample holders. For both samples, different external field profiles were selected.

Figure 5-13. Sample holder after drilling holes for cooling purposes. The holes were made to improve the heat dissipation during the cooling down period.

The zero-field cooling results showed three distinctive regions: shielding, linear, and saturation regions according to the applied field. The zero-field cooling explanation needs a theoretical model based on the Bean model, which can be used to build an electrical-circuit model for the rings magnetization. As we already know from the literature review presented in section 2.1:

$$L\frac{di}{dt} = -A\frac{d\phi_{ext}}{dt}$$

when the values of the current and external field are zero. When the applied field is below the penetration field B_p , the shielding zone has no trapped field. Within this zone, the external field was entirely shielded by the rings, and at the centre, no or very small field was trapped. When the applied field was higher than the penetration field B_p , the ring began trapping the field and entered the linear zone. When the applied field reached approximately four times of the penetration field B_p , it became the saturation zone and the final trapped field was equal to the penetration field B_p . Figure 5-9 shows the shielding, linear and saturation zones.

These zones in electrical circuit model can be expressed as:

Shielding zone

if $$\phi_{ext}(t_0) < I_c L \qquad 5\text{-}2$$

$$L\frac{di}{dt} = \frac{d\phi_{ext}}{dt} \qquad 5\text{-}3$$

for the explanation negative sign and area are neglected.

$$i(t_0) = \frac{\phi_{ext}(t_0)}{L} \qquad 5\text{-}4$$

$$i(t_1) = 0 \qquad 5\text{-}5$$

Linear zone

if $$\phi_{ext}(t_0) \geqslant I_c L \qquad 5\text{-}6$$

$$i(t_0) = i_c \qquad 5\text{-}7$$

$$i(t) = I_c + \frac{\phi_{ext} - \phi_{ext}(t_0)}{L} \qquad 5\text{-}8$$

until $$\phi_{ext}(t_0) < 2I_c L \qquad 5\text{-}9$$

$$i(t_1) = -\frac{\phi_{ext}(t_0)}{L} + I_c \tag{5-10}$$

Saturation zone

if
$$\phi_{ext}(t_0) > 2I_c L \tag{5-11}$$

$$i(t_1) = -I_c \tag{5-12}$$

Further increasing the external field will not increase the induced current, but it will start degrading it as the external magnetic field starts affecting the critical current of the tape. The negative sign shows this degradation.

During the experiment, field cooling could not attain the 30 K temperature and took 3 out of five days. Due to the shortage of time, it was not possible to apply all the fields, so the minimum field was selected as 2 T. Therefore, it was not possible to see the shielding zone in the experiment result. The external field profiles for both ZFC experiments are shown in Figure 5-14. The time has been normalised to fit both magnet profiles. The applied field sequence for magnet 1 was 2 T, 3 T, 3 T and 4 T and 5 T, and for magnet 2 the external field profile was 2 T, 3 T, 4 T and 5 T. The duration between the consecutive fields for magnet 1 was between 30 and 40 mins while for magnet 2 it was just 15 mins. After reaching the maximum field during each field iteration, it started decreasing immediately. The changing rate of the external field during ramping up and ramping down was kept constant at 0.15 T/min.

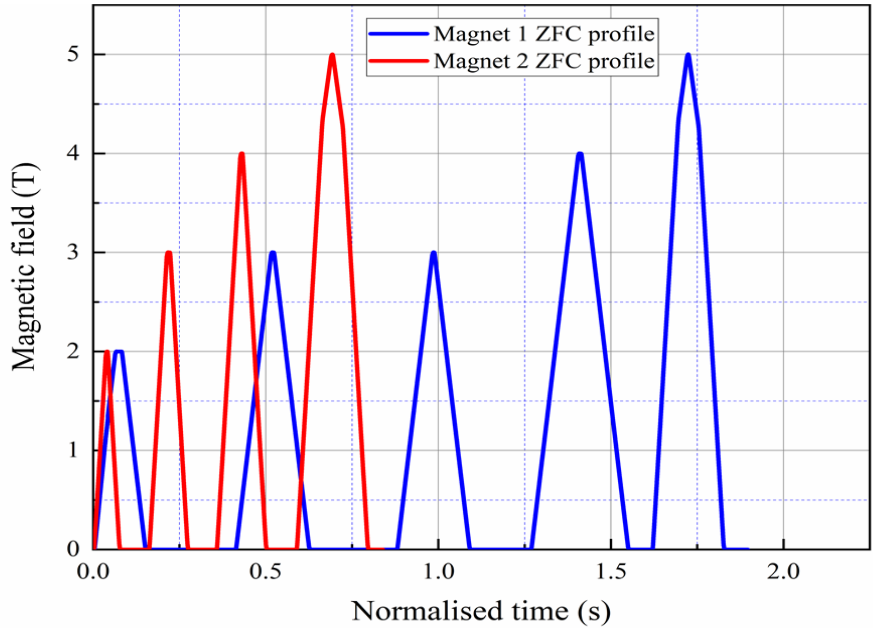

Figure 5-14. External field profiles for both Shanghai superconductor magnet samples.

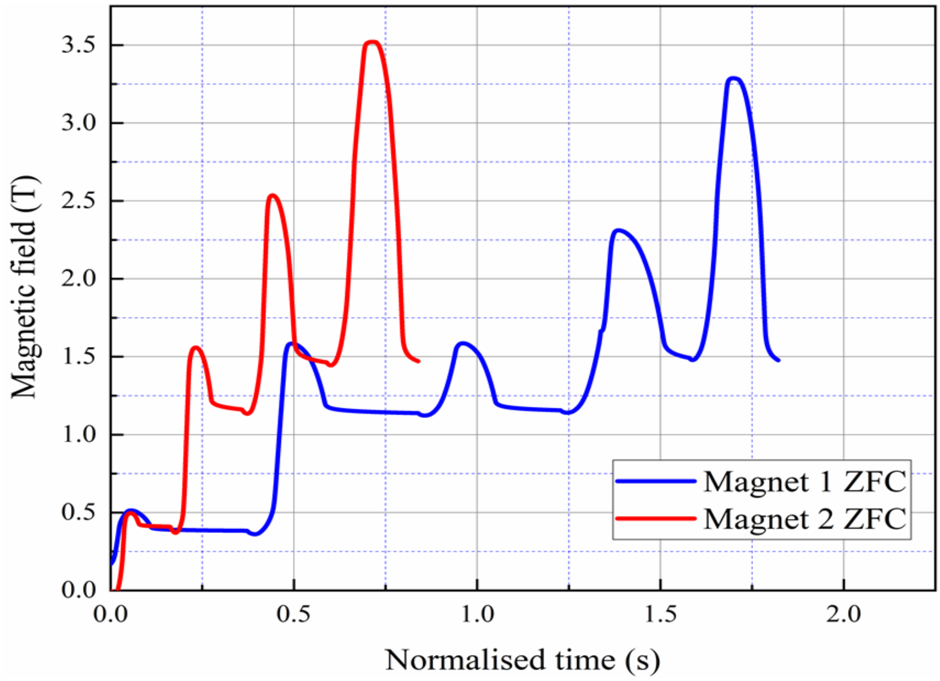

Figure 5-15. Zero field cooling experiment results for both Shanghai tape magnets. Both profiles differ in terms of the external field profile and the duration between the consecutive two fields. The external field profile of magnet 1 was 2 T, 3 T, 3 T, 4T and 5 T. while for magnet 2 it was 2 T, 3 T, 4 T and 5 T.

The external field profiles differed in terms of time as well as the fields. Magnet 1 was tested for the same field twice to see if there was any change in the trapped field. It was shown that repeating the same external sample field does not have any effect on the trapped field. The ramping rate of the external field was the same for every field, and the only difference was the period between the two consecutive fields. Both the magnets had a final trapped field of 1.49 T. Figure 5-15 shows the zero-field cooling experiment result for both samples. The modelling result predicted the trapped field of 1.71 T.

During field cooling, the mismatch was considered to be due to the temperature not reaching 30 K. This non-stable temperature was due to the high external magnetic field as the trapped saturation field was around 1.7 T, so the external field should be around 4 T. In our field cooling experiment, 6 T was applied as an external field which was very high. Due to the high external field, the temperature of the sample was destabilised, and it was not possible to reach 30 K. The thermal conductivity of the Stycast epoxy was very low, so heat removal from the magnet was prolonged. As the maximum sample space was 100 mm, out of which the magnet was occupying 90 mm as a solid mass. It was thus taking too much time to cool down the magnet. Around 40 K, it is was almost impossible to remove further heat from the magnet with available power from the system. The field cooling was performed at 40 K. From the experience of field cooling experiment, and it was decided to make holes in the magnet holder and then to perform zero-field cooling. This was quicker and made it possible to reach the temperature of 30 K. Secondly, during zero-field cooling, there was no external field, so there was no external source of heat production during the cooling process.

From the literature, it was concluded that epoxy has a degrading impact on the critical current of coated conductors. Epoxy has significant contractions which delaminate interlayer insulators which also damages the induced current capacity of the ring magnets [133]. Also, by heating the sample at a slower rate, it was noted that either the thermal conductivity was low or the position of the thermal sensor in the system was not enough to estimate the exact temperature of the epoxy impregnated ring magnets.

The heating profile after the field cooling experiment is shown in Figure 5-16. It shows that the trapped field of the magnet did not reduce zero until the temperature was 110 K. It should be zero around 92 K, which is the critical temperature of the YBCO superconductor. This can be attributed to two facts; first, the thermal sensor does not give the exact temperature of the sample due to its position. Secondly, the thermal conductivity of the epoxy is not good enough to remove the heat efficiently.

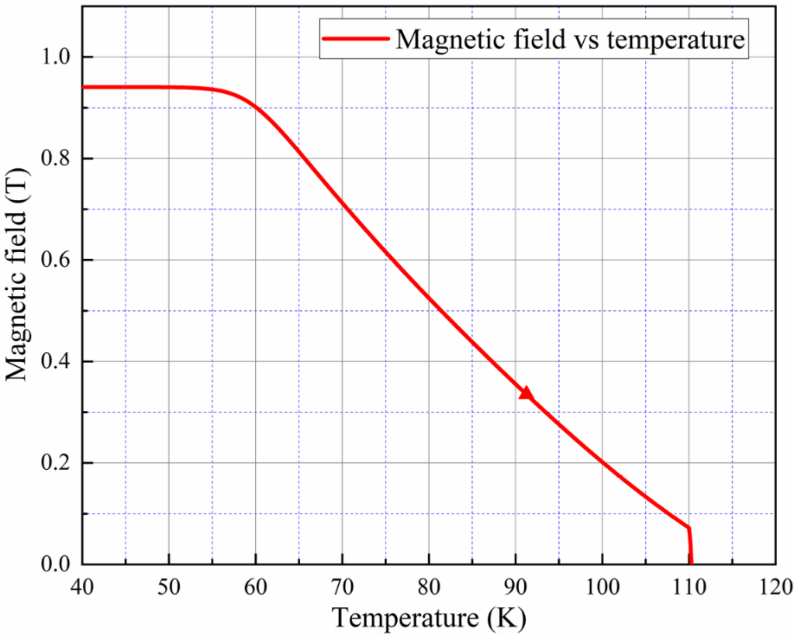

Figure 5-16. Trapped field vs temperature during the heating of the magnet after field cooling

5.5 Field cooling of SuperPower sample

The third magnet was created using superconducting tapes provided by SuperPower. It was a double stack 200 ring magnet. The inner tube diameter was 10 mm, and the tape width was 12 mm. The rings stacked in the holder are shown in Figure 4-14, while the final magnet after impregnation was shown in Figure 4-15. The ramp rate applied at the beginning of the experiment is 0.15 Tmin^{-1}, but during the experiment after 300 sec, it changed to 0.1 Tmin^{-1}. The reason for this change still not known. The background magnetic field was 5 T.

The results for the trapped field in the double-stack ring magnet at different positions from the centre are shown in Figure 5-17. The graph clearly shows a significant increase as we move towards the closed side. The blue curve is for the sensor near the closed end, the red is the middle sensor, and the black curve is for the sensor near to the open end. The trapped field of 4.6 T is the highest known field trapped in a ring magnet made from superconducting tapes. The hall sensor in the centre recorded 4.19 T and the sensor near the open end recorded 3.8T. This variation in the trapped field is due to the asymmetric geometry of the ring magnet. When the applied field begins to decrease, it induces a current in the jointless rings, which resists the change in the total flux within the magnet. The induced current in the loops near the closed end generates a higher internal field compared to the open side. Although the value is not as high as already recorded in bulks and stacks [134], [135], it is still remarkable, given the larger diameter of the rings possible by using tapes commercially available with average I_c values.

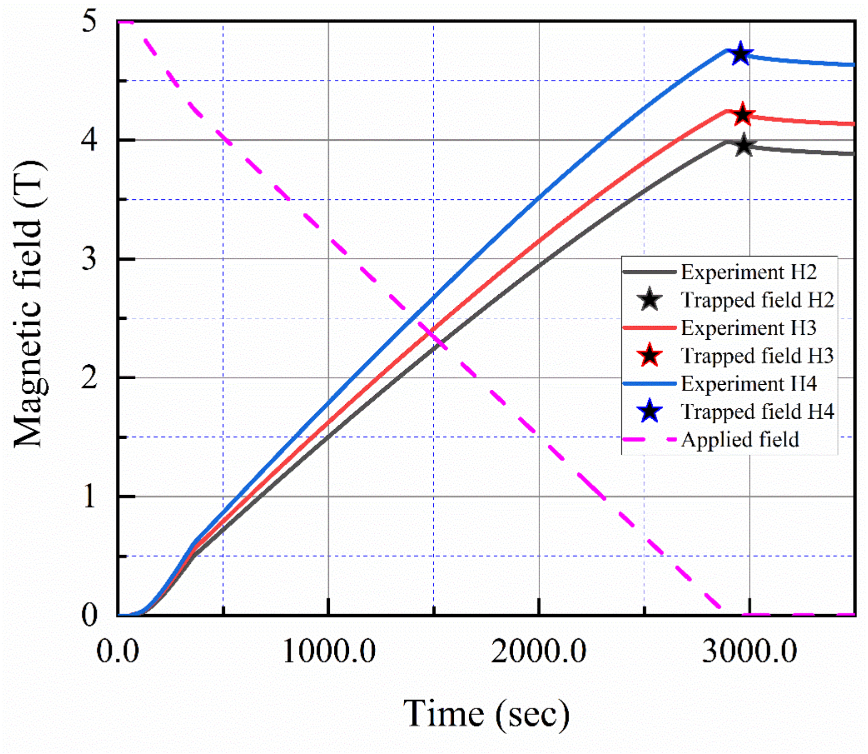

Figure 5-17. The trapped field at 25 K with the applied field for FC. The highest trapped field of 4.60 T was at 4.5 mm towards the closed ends from the centre. This $B_{tr} - B_{app}$ for the experimental trapped field results.

The temperature sensor attached to the cold plate monitored the temperature of the sensor during the magnetization. The temperature of the sample was constant during the whole experiment, as shown in Figure 5-18. The temperature profile clearly shows that there were no major temperature variations during the experiment. During the experiment, the heat generated within the stacked rings was removed efficiently via the paraffin wax mixture and the brass holder. It clearly shows that the performance of paraffin wax is much better than the epoxy used in the previous experiments. Also, the thermal conductivity of the wax has improved significantly with the addition of the aluminium nitride.

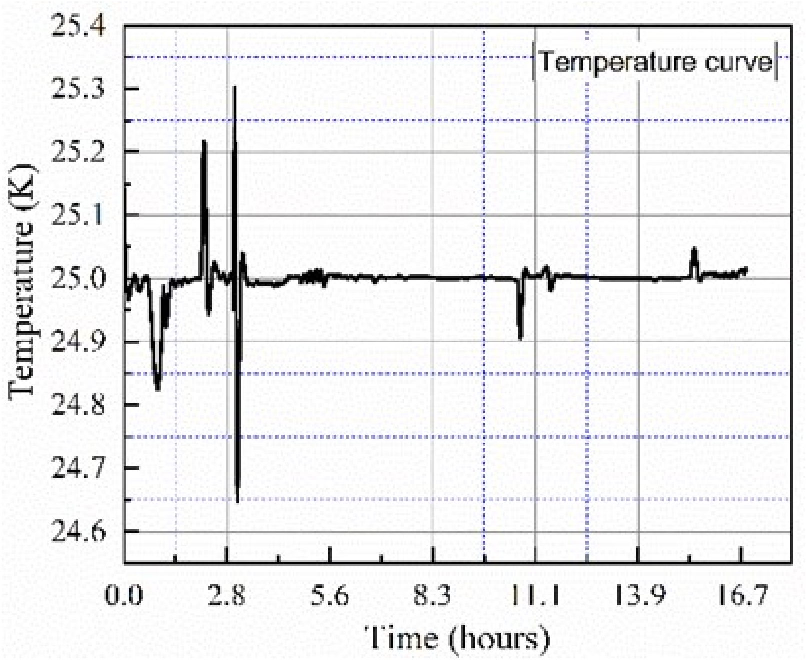

Figure 5-18. The temperature of the sample noted by a sensor attached to the cold head during the whole experiment, including flux creep part as well.

This graph clearly shows there were no flux jumps during magnetization. The maximum increase in temperature noticed by the temperature sensor was 0.3 K. When individual flux jumps occur in a superconductor, heat is generated, and this heat tends to increase the temperature of the magnet. If the removal of heat from the magnet is not quick enough or the heat capacity is low, then the temperature rise can result in global flux jumps and de-pinning. This is due to a sudden decrease in J_c because of the local temperature spike and results in de-pinning of neighbouring flux line and has an avalanche effect. This global flux jump results in a significant drop in the trapped field. In the case of a bulk, complete collapse is often observed for high fields and low temperatures [58].

5.5.1 Degradation of the trapped field after magnetization

In case of type-I superconductors, resistance is nearly zero at a critical temperature which makes the persistent current remain in the superconductor without measurable degradation. In type-II superconductors, a small resistance can appear due to flux creep and flux flow. This results in measurable degradation of the induced current and therefore decreases the trapped field [95]. Flux creep was measured for the trapped field up to 17 hours after the field cooling while maintaining the temperature at 25 K. The result shows that the trapped field decayed after the field cooling test. It shows the presence of superconducting resistance, and the decay rate shows that this resistance was very small, and this decay rate further dropped with time. The decay was logarithmic as expected. During the early stage, the decay was faster, and later it became logarithmic. There are many factors which make the flux measurement complicated [136], [137]. These include possible residual magnetization in the superconducting coil, which may take a few minutes to disappear completely, and also due to possible heating of the sample. The initial decay is similar to that obtained for the pulse field magnetization of a bulk [138], which suggests there may be some constant heating of the magnet during the field cooling process which was not measured by the temperature sensor, which was not in direct contact with the magnet. The measured time window was long enough to note the behaviour of flux creep, which became logarithmic once the heat was properly removed from the magnet. The normalised flux creep with respect to time is shown in Figure 5-19.

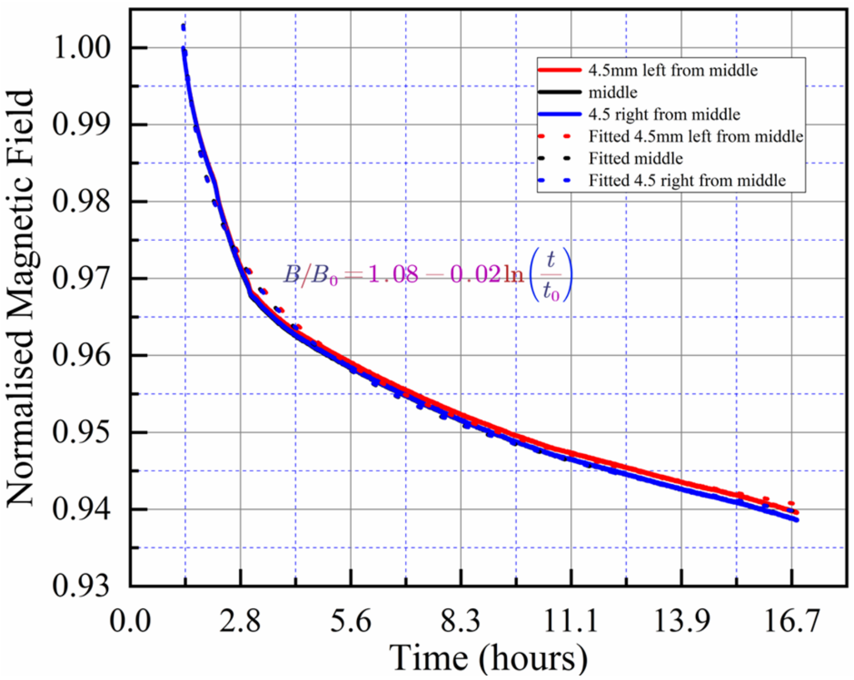

Figure 5-19. Normalised flux creep for different positions within the ring magnet and recorded for more than 16 hours. B_0 is the final trapped field as marked by the stars in Fig 5.6.

All superconductors experience flux creep, which is due to disturbances in the flux vortex and HTS experience higher flux creeps rates [40][139]. This flux creep causes the trapped field of the superconducting magnet to decrease. All three hall sensors measured the same decay rate. The time dependence of the decay was logarithmic and is calculated as:

$$B/B_0 = a + b\log\left(\frac{t}{t_0}\right) \qquad 5\text{-}13$$

where t_0 is the arbitrary unit of time in seconds. The fitted curve for the normalised data gives values $a = 1.08 \; and \; b = -0.02$. The values of B_0 were 4.60 T, 4.19 T and 3.8 T respectively. To understand how the flux creep will impact the trapped magnetic field over a period of time, it is a standard practice to calculate how much time it will take to decay by a certain percentage [95]. It was noted that during the first two hours, the flux creep was more prominent and reduced the trapped field value by 5.3% , while the overall decrease in the trapped field was 7.8 % after 16.7 hours.

5.5.2 Magnetic Shielding in a ring magnet

The fundamental properties of superconductors to dc signals are zero resistivity and the Meissner effect, as explained in chapter 1. The zero resistivity provides lossless paths for the current, which is why they can sustain the induced current once the external field is removed. The Meissner effect is the exclusion of a magnetic field from the interior of the superconductors and is also known as the shielding effect. In superconductors, an external magnetic field is cancelled out by the shielding current which flows at the outer perimeter of the superconductor surface. The shielding effect has been extensively studied in bulks [140] [141] [142], Compared to an HTS bulk, shields made from coated conductors have the advantage of size, diameter, low cost, and large scale availability. Magnetic shield performance depends on two factors: the axial shielding factor and the shielding threshold beyond which shielding is no longer effective [143]. The shielding factor is defined as:

$$SF = \frac{B_{app} - B_{trp}}{B_{app}} \times 100 \qquad 5\text{-}14$$

where B_{app} is the externally applied magnetic field and B_{trp} is the field trapped by the superconducting magnet.

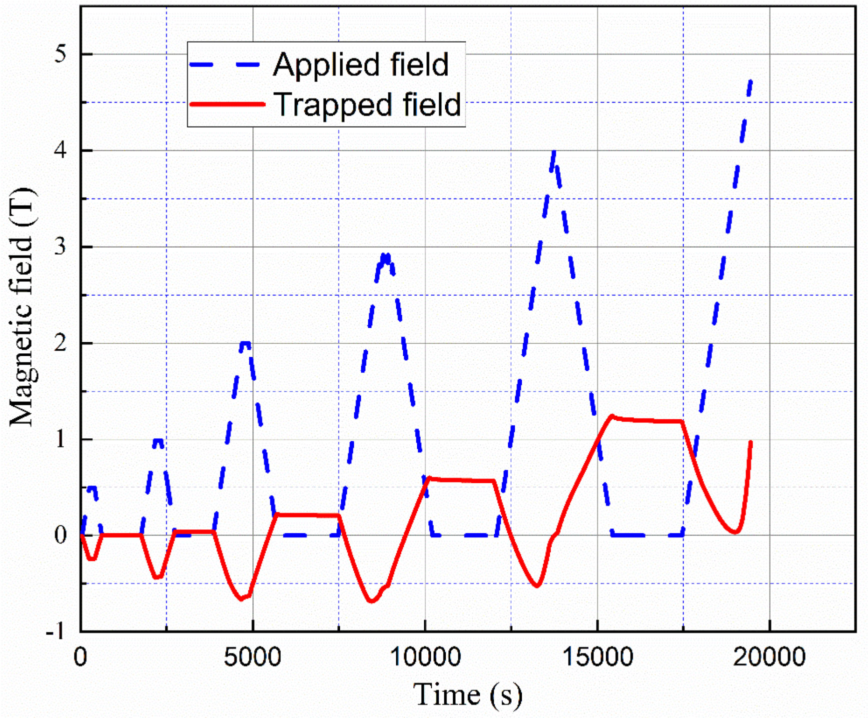

Figure 5-20. Applied vs trapped field during ZFC cooling experiment of the ring magnet.

Figure 5-20 shows the experiment results for the zero-field cooling experiment at Cambridge University. The ramping rate for the external field was $9.251\ T\mathrm{min}^{-1}$. The magnetic field B_{trp}, at the centre, was measured by using a single calibrated cryogenic hall sensor HNP-NP. The hall sensor was placed in the middle of the double-layered HTS ring, with an offset of 3 mm towards the closed side of the ring magnet. The triangle waveform is the applied field with 0.5 T, 1 T, 2T , 3 T, 4 T and 5T peak magnitude applied sequence.

Zero field cooling was performed by the 3D COMSOL model to validate the experimental results. It was noticed that as the sensor position was moved towards the open end, the negative part vanished, and all the waveform was positive. This is because some external field lines pass through the middle of the rings. At the middle, the positive and negative waves tend to cancel each other. As we move towards the closed end, the overlapping ends resist the external field, and the curve becomes negative, and it acts as perfect shielding. Figure 5-21 shows the modelling result for the zero-field cooling. The blue dotted lines are for the external field, while three solid lines are for different positions of the sensors. The black line is reading at 3 mm distance towards the open end; red was the middle of the ring while light blue was at 3 mm towards the closed end. The modelling result was very close to the experimental results.

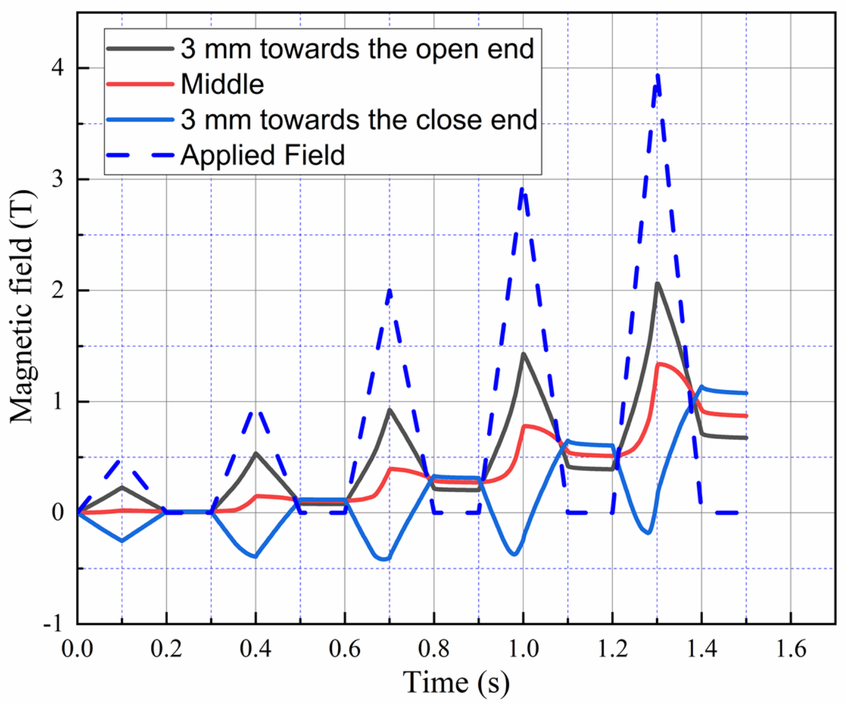

Figure 5-21. Modelling results showing the impact of sensor placement during zero-field cooling.

The trapped field sequence was the same as already obtained during the field cooling experiment. The maximum field was recoded near the closed end. The shielding result was only possible up to 4 T, and unfortunately, during 5 T cycle, the ring magnet fell off. It broke the probe because of the self-weight and strong electromagnetic forces between the LTS magnet and the ring magnet. Figure 5-22 shows the broken probe during the experiment.

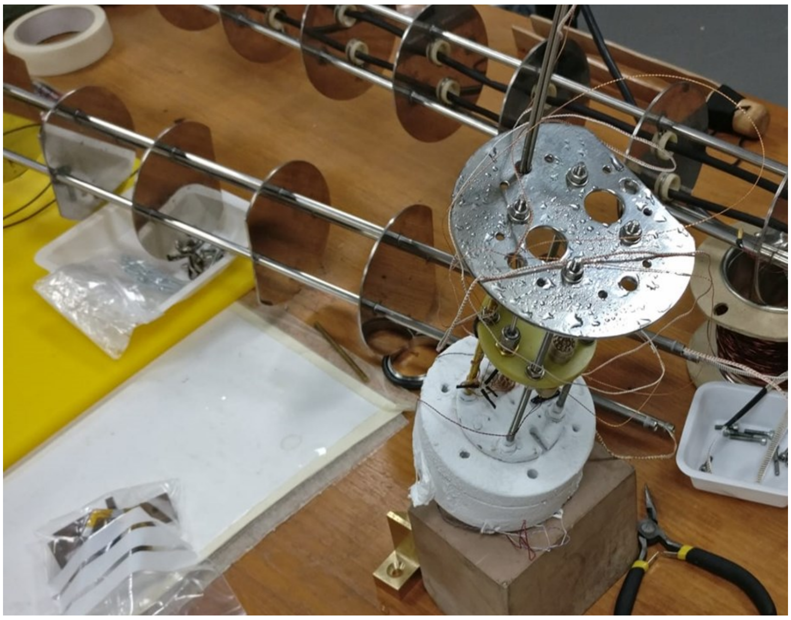

Figure 5-22. Broken probe during the 5 T cycle of the zero-field cooling experiment.

Figure 5-23 shows the shielding factor in the axial direction measured at 3 mm off centre towards the closed end as a function of the externally applied field B_{app}. The inset shows the trapped field induced in the magnet as a function of an externally applied field. As the experiment was aborted in the middle, the limit of the shielding cannot be calculated. Also, due to the asymmetric distribution of the magnetic field of the magnet, as already shown in section 5.2, the shielding will be more significant near the closed end and lowest near the open end. The impact of the air gap between the layers have been studied [144]; shield performance decreases with an increase in the air gap.

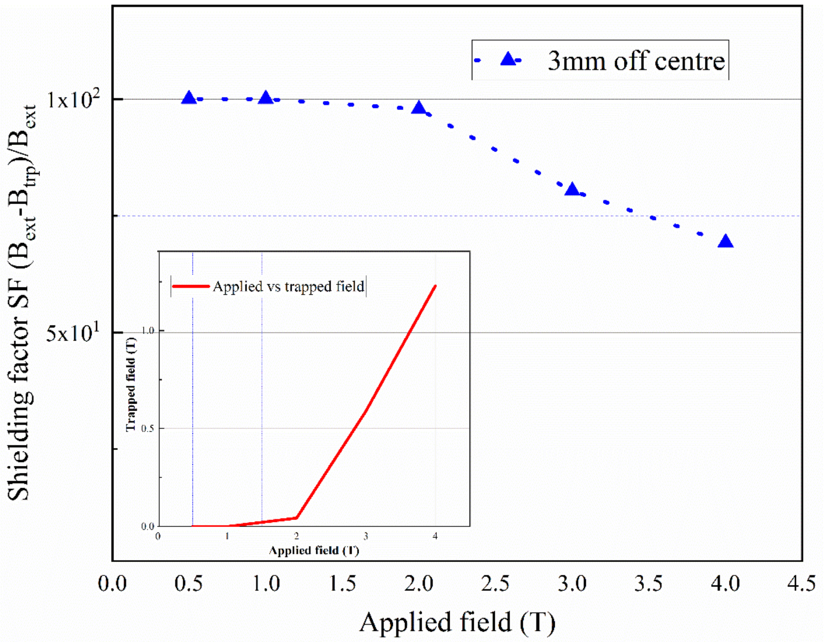

Figure 5-23. Shielding factor SF measured at 3 mm off centre towards the closed end for the applied field. Inset: dependence of the trapped field vs applied field.

5.5.3 Paraffin wax impregnation improvement

The impact of paraffin wax mixed with ceramic fillers on the magnet thermal conductivity was tested by heating it to discharge the magnet completely. It showed results very near to the actual behaviour of the YBCO superconductor. The transition temperature of YBCO is 92 K. Above this temperature it becomes non-superconducting and acts like a regular conductor. Figure 5-24 shows the heating profile of the sample after magnetization and flux creep behaviour. It clearly shows that the thermal conductivity of the paraffin wax mixture was much better than that of the Stycast 1250 FT, which was shown in Figure 5-16. The trapped field of the ring magnet become zero around 95 K as compared to 110 K in the case of epoxy impregnation. It explains that there is a very minute difference in reading between the sensor and the sample. Previously, it was one of the assumptions for the mismatch of results that the sensor position has an impact on the temperature reading of the magnet. However, this profile indicates the degradation in previous results was entirely due to the impact of the epoxy.

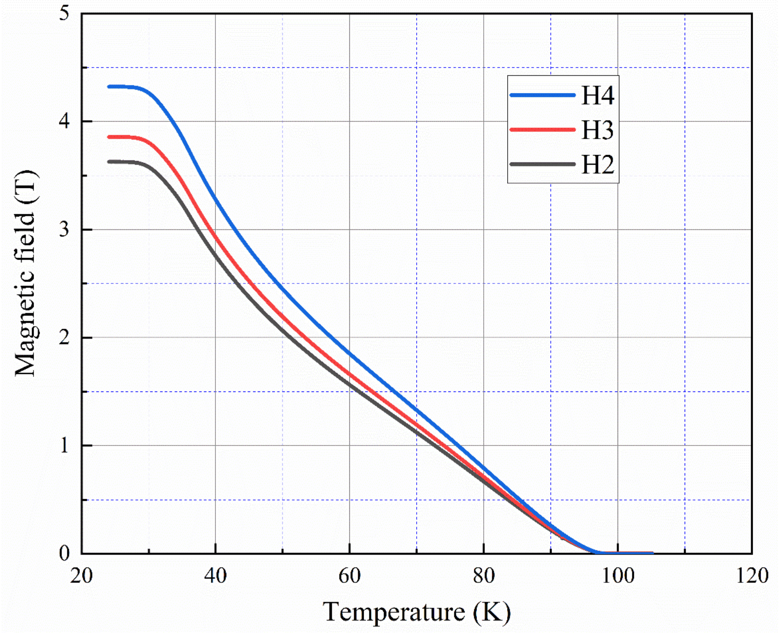

Figure 5-24. Magnetic field vs temperature. Impact of heating the sample on the trapped magnetic field.

5.6 Conclusion

This chapter discusses the experimental results for the samples created in chapter 4. The first sample was not successful due to the larger sample holder and no proper impregnation usage, which suggested the use of impregnation to limit the movement of the ring magnet during magnetization. The second sample used an epoxy type impregnation which made cooling difficult during field cooling magnetization, and it was performed at 40 K instead of 30 K, which was the actual desired temperature. Zero field cooling magnetization was performed. The results showed greater than 20% mismatch between the modelling and experiment result. This mismatch of the result was attributed to the impact of the epoxy, which decreased the performance of the rings or due to imbalanced thermal conductivity of the sample. The SuperPower tape magnet was impregnated with paraffin wax and aluminium nitride powder mixture. The maximum field of 4.6 T was recorded, and flux creep behaviour was observed. The shielding experiment was not successful because of the force mismatch during magnetization, which caused damage to the probe. The heating profile of the magnet after magnetization and flux creep provided a good match between the temperature sensor reading and the sample superconducting behaviour.

6 CURRENT AND MAGNETIC FIELD DISTRIBUTION

The record for the trapped field has exceeded 17 T for a single grain YBCO bulk [134]. More recently, with the maturing of YBCO-coated conductor technology, stacks of YBCO tapes have been proposed as a new type of permanent superconducting magnet with a maximum reported trapped field of 17.7 T [63]. Using permanent superconducting magnets for the development of advanced superconducting machines has been studied extensively worldwide. The ultimate aim is to use the high-field capability of permanent superconducting magnets to improve machine magnetic loading and power density.

Although the magnetic fields provided by these two superconducting permanent magnets are more than 10 times higher than rare earth permanent magnets, their limited size has become a significant factor hindering large-scale applications. Manufacturing processes limit the sizes of existing superconducting permanent magnets. For example, the size of the YBCO bulks is limited by the crystal growth process, so a single bulk is usually up to 65 mm in diameter [134]. The size of YBCO stacks is limited by the width of a commercial YBCO-coated conductor (46 mm) [145].

6.1 Experimental validation of modelling results

To help understand the physics of HTS ring magnets, three dimensional finite element modelling was performed using the homogenised H formulation which is already explained in section 3.4.2. The governing equations already explained in 3.4.1 used in the model can be summarised by the general form:

$$\mu_0\mu_r\frac{\partial H}{\partial t} + \nabla\times(\rho\nabla\times H) \qquad 6\text{-}1$$

where $H = [H_x, H_y, H_z]^T$ and $\rho = [\rho_x, \rho_y, \rho_z]^T$ is the resistivity. For HTS domains, ρ is governed by the E-J power law[146]. The magnetic field dependence of the critical current density $J_c(B)$ is considered in the model using direct interpolation of measurements of $J_c(B)$ at 25 K. The HTS ring magnet has 200 rings with a 3D asymmetric geometry, and the previously established H formulation homogenisation [101] is modified by taking into account two assumptions which were discussed in section 3.4.2. Each set of ten rings is represented by one single domain and separated by an air domain. In total, 20 domains represent the 200 rings, and have the same critical current penetration depth as that of 200 individual rings.

The magnetization process simulated by the model is field cooling. The magnetic field at the coil centre follows the external field linearly. As the background field decreases, it induces a current in the rings, which shows the trapped field once the external field reduces to zero.

Figure 6-1 shows the comparison between modelling and the experiment result. Due to the longer computational time, faster ramping current of the external magnetic field was employed. This graph shows the magnetic field response against a normalised time. The solid lines are the experiment results, while the dotted lines with symbols are for the modelling results. The modelling result gave a good match with the experiment result, and the difference is less than 7%. The labelled points a-e and e' are the time steps during the ramping down of the external field from 4 T to 0 T respectively. The modelling results are a good approximation of the experiment results. So this model can be used to predict the behaviour of the actual ring magnet at different external fields.

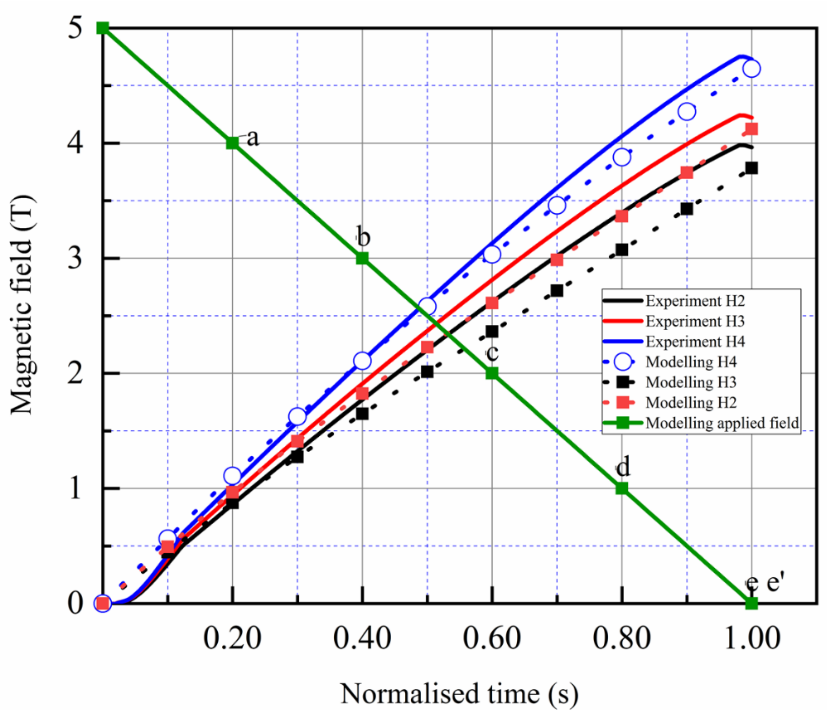

Figure 6-1. Simulation result with experiment results. Points (a) and (e') shows the time steps used to show the normalised current distribution. The calculation uses a 10-sec ramping rate for the magnetic field.

6.1.1 Current distribution in the ring magnet

The current distribution during the field cooling process for the ring magnet is shown in Figure 6-2. The time steps a-e and e' mentioned in Fig 5.9 correspond accordingly to the current distribution in the ring magnet. It clearly explains that the current distribution in the rings is not uniform. This non-uniformity is due to the critical current distribution and the magnetic field distribution. The current is induced simultaneously from the innermost and the outermost HTS domains when the magnetization starts. This induced current generates the field to prevent the reduction of the flux. As the external field reduces further the induced current increases. This increase is almost linear with the decrease in the external field. Since the rings are superconducting, the direct current can flow in the rings without any resistance and will be exactly equal to the trapped field measured in the experiment.

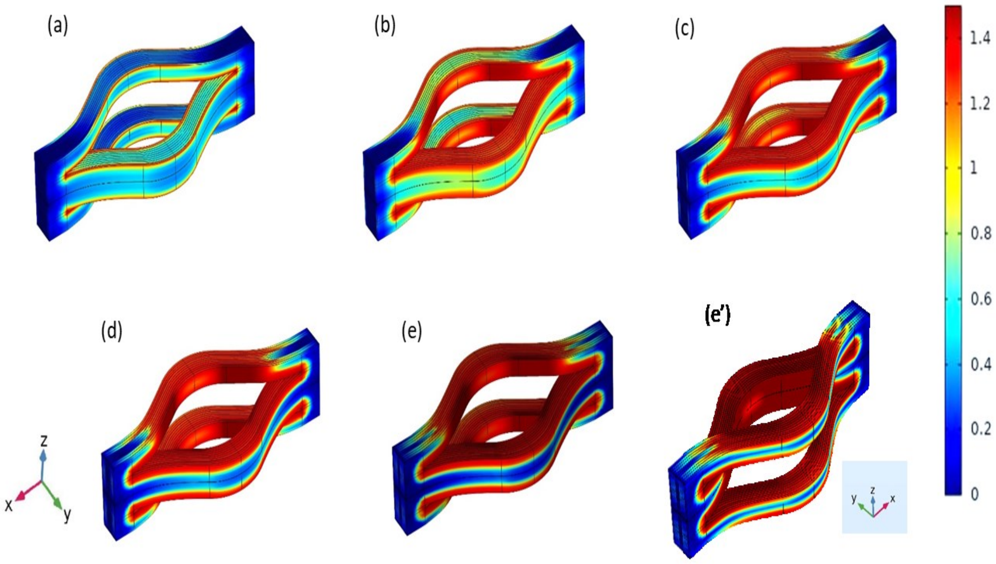

Figure 6-2. The distribution of the normalised current density J/J_c in the ring magnet during the down ramping process. Each figure labelled from a-e and e'. were (a) applied field 4 T, (b) applied field 3 T, (c) applied field 2 T, (d) applied field 1 T, (e) applied field for 0 T on the closed side and (e') applied field on the open side.

Figure 6-3 shows the induced current in each homogenised ring and the total current induced in all turns. The distribution of the persistent current in the rings is non-uniform. Ring 1-10 indicates the innermost turns, while rings 91-100 indicate the outermost domain. When the external field starts to decrease, the innermost and the outermost rings have induced current to compensate for the field reduction from the applied field, and the neighbouring rings follow up. The current in the inner and outer domains reaches its peak value of 20% of the applied field reduction. The innermost and outermost rings have the lowest critical current [89]. As the inner and outer rings becomes saturated, the remaining rings have limited currents induced in them. This saturation of induced current in the inner and outer rings increases the resistance of these rings, forcing the next rings to have induced currents which have no or limited induced current. This process continues as all the rings becomes saturated.

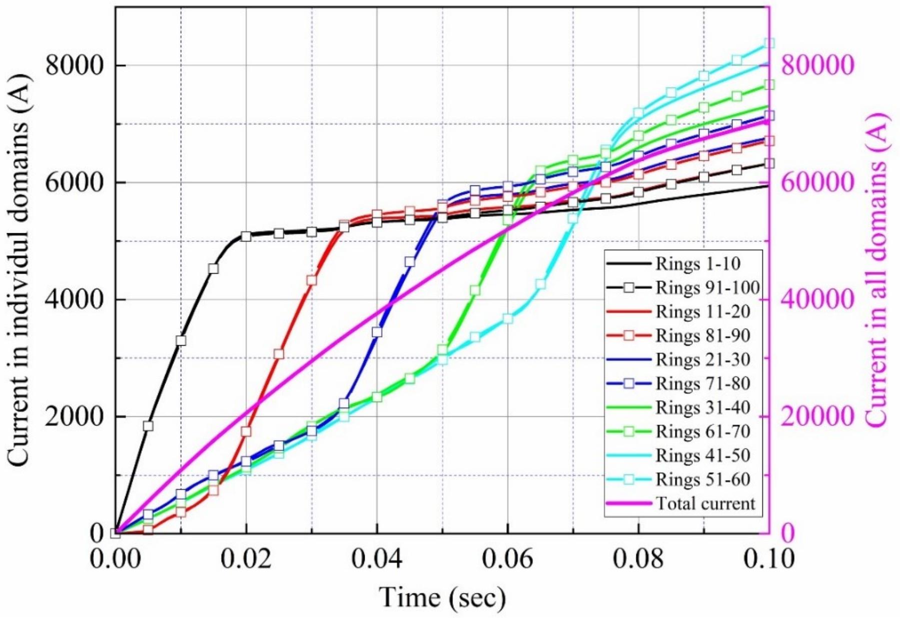

Figure 6-3. Calculated induced current in the 10 HTS homogenised domains during 5T field cooling.

As the total induced current increases the trapped field by the rings also increases. The middle domains with rings 41-60 have the highest induced currents flowing in them after the magnetization.

6.1.2 Temperature and ramping rate effect on the magnetic field

The modelling results for the trapped field in the double-stack ring magnet for different field cooling temperatures are shown in Figure 6-4. The graph clearly shows a significant increase in the trapped field as the temperature decreased. The asymmetric distribution of the magnetic field was due to the geometry of the ring magnet. The higher the temperature, the lower will be the trapped field, which is due to a reduction in critical current. In the models, the critical current value was taken from the graphs shown in Figure 2-6. As the critical current of the superconductor is temperature-dependent, so its value changes. The model showed a very good match with the experiment result at 25 K, so the same technique was applied to estimate the trapped field at lower temperatures.

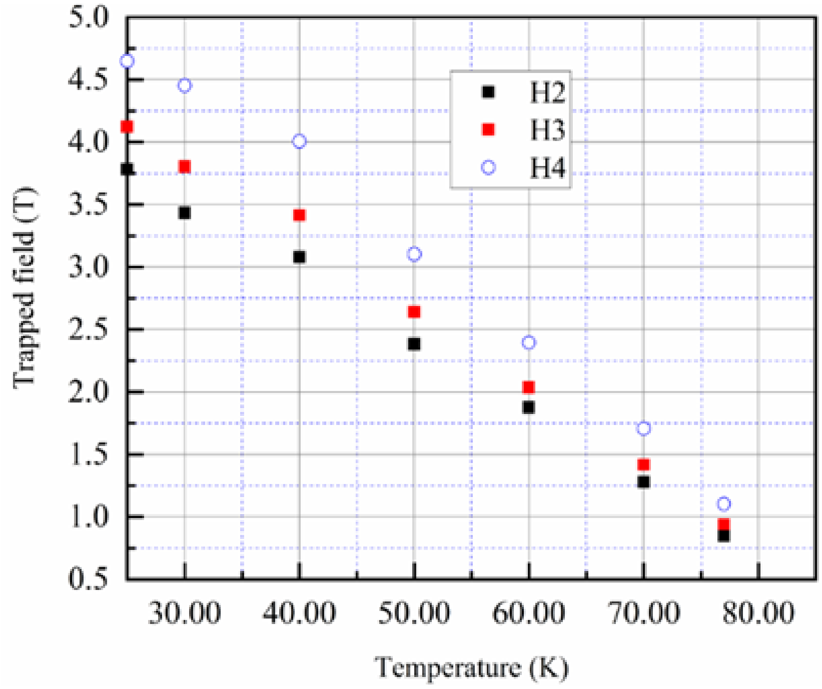

Figure 6-4. Trapped field of the ring magnet using the field cooling method at various temperatures. The trapped field increased approximately linearly as the temperature decreased. H2, H3 and H4 are the sensors at different positions from the centre as already mentioned above.

Superconducting loops can trap the magnetic field when they are placed in changing magnetic fields, and the temperature of the sample is below its critical temperature. It induces the current in superconducting loops to compensate for the change of total magnetic field inside the ring. The trapped field also depends on the ramping rate of the external field. Figure 6-5 shows the impact of the ramping rate of external magnetic fields on the trapped field of the ring magnet. In this figure, values for the sensor near the closed ends are considered. As all the ramping rates have different computation times, the normalised time scale is used in the graph to give all the curves the same time units.

According to Faraday’s Law [76], we have:

$$L\frac{di(t)}{dt}+V_0\left(\frac{i(t)}{I_c}\right)^n=\frac{d\phi}{dt} \qquad 6\text{-}2$$

where L is the inductance, ϕ is the total flux, $i(t)$ is the induced current, $V_0 = E_0 l = 1\mu V cm^{-1}$ is the criterion for measuring the I_c, l is the total length of the ring, and n is the E-J power-law index.

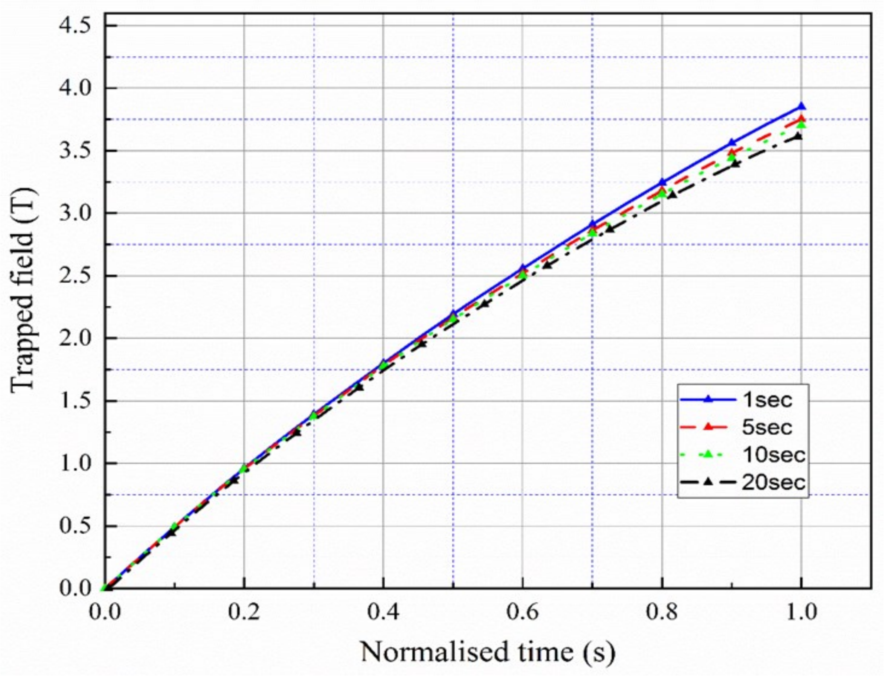

Figure 6-5. Comparison of the trapped field for four different ramping rates. The curves are for the sensor H3, which is in the middle of the ring magnet.

When the changing rate is very slow, the heat dissipation during the field cooling inside the sample holder is also very small, so the temperature of the rings remains constant as does the critical current I_c of the HTS rings. As mentioned in equation 5.3, the changing rate of the induced current is not directly proportional to the external field. When the ramping rate of the external magnetic field is increased, the changing rate of the current $i(t)$ also increases. However, once $i(t) > I_c$, the E-J power term limits the peak value of the current $i(t)$. In other words, a current greater than the critical current limits the induced current and the rings current is dominated by the in field critical current of the rings. This behaviour is very much clear from the graph, where there is a slight decrease in the trapped field once the ramping rate decreases. Suppose the period of the externally applied field is greater. In that case, the induced current will experience flux creep during the magnetization, and the final trapped field will also decrease due to this flux creep.

6.2 Conclusion

A maximum trapped field of 4.60 T was recorded for ring magnet, which is the highest achieved for this type of magnet. The ring magnet is flexible in size, which is one of the limitations in bulk and stack superconducting magnets. This ring magnet technology is promising for the creation of large size magnets. The unique geometry of the double stacked ring magnet causes the asymmetric distribution of the magnetic field. The magnetic field decreases with the increase in temperature. The ramping rate also affects the trapped field as the decreased ramping rate slightly decreases the trapped field. To improve magnetic field homogenization, there is a need to investigate a new stacking method so that this magnet can be used for practical applications.

7 OPTIMISED RING MAGNET DESIGN

The geometry presented in chapter 6 shows that its magnetic field distribution is not symmetrical. The new design is proposed to have increased and better magnetic field distribution from the ring magnet. This chapter will explain the difference between the new design and the previous design and will present the modelling results for the new design.

7.1 Asymmetric field distribution

As discussed in chapter 4, the ring magnet is composed of stacks of rings made by slitting the superconducting coated conductors. The process of making the rings is comparatively simple and can be made with arbitrary inner diameters. The disadvantage of the ring magnet is the asymmetric geometry in an axial direction. This asymmetry of geometry was responsible for the angle deflection in the trapped magnetic field. Figure 7-1 (a) shows the orientation of the asymmetric ring magnet, obtained by taking the cut plane in the YZ direction, with the X coordinate being taken as zero. Figure 7-1 (b) shows the field distribution after the field cooling magnetization of the ring magnet. The arrows show the direction of the magnetic field. The bar shows the strength of the trapped field at different positions in the centre of the magnet.

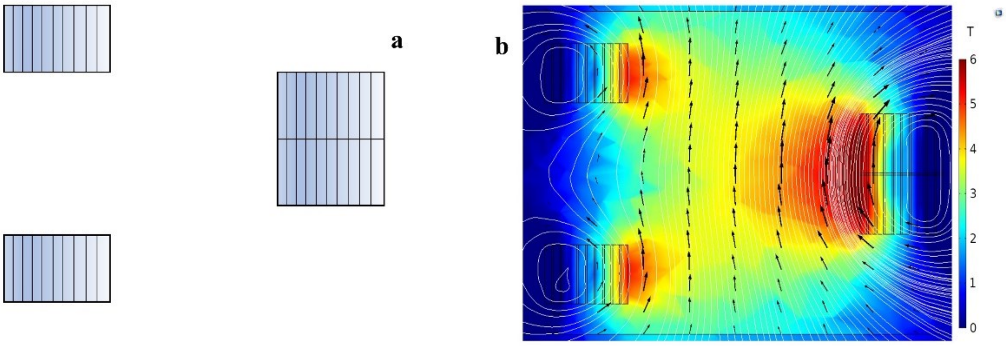

Figure 7-1. (a) The 2D configuration of an asymmetric ring magnet as discussed in chapter 4 showing angle deflection of the magnetic field. (b) shows the magnetic field distribution of the ring magnet.

This is the same homogenised model built in COMSOL as discussed in chapter 3. The modelling was performed by using the H-formulation as described in section 3.4.1. It can be seen that the magnetic field distribution was angled towards the closed ends while the magnetic field was lowest near the open end in the middle. Although the ring magnet is very robust, this angle deflection leads to an asymmetric field distribution in a vertical direction. The asymmetric/inhomogeneous magnetic field distribution of the trapped field results in lateral force without experiencing any lateral movement [147].

7.2 Fabrication of optimised ring magnet

A new ring magnet design has been proposed to overcome the asymmetry in the trapped magnetic field. This section describes a novel HTS ring magnet design made from coated conductors with symmetrical field distribution at the centre. The trapping field capacity of the new magnet will also be much better than the one discussed in previous sections. The new design will be investigated in terms of the vertical trapped field at the centre of the magnet. Finite element modelling (FEM) in COMSOL is used to predict the magnetic field of the new magnet. The new design has the same construction as previously defined, but the stacking pattern and the slitting lengths are different. It is done by placing the two different size rings in mirrored directions.

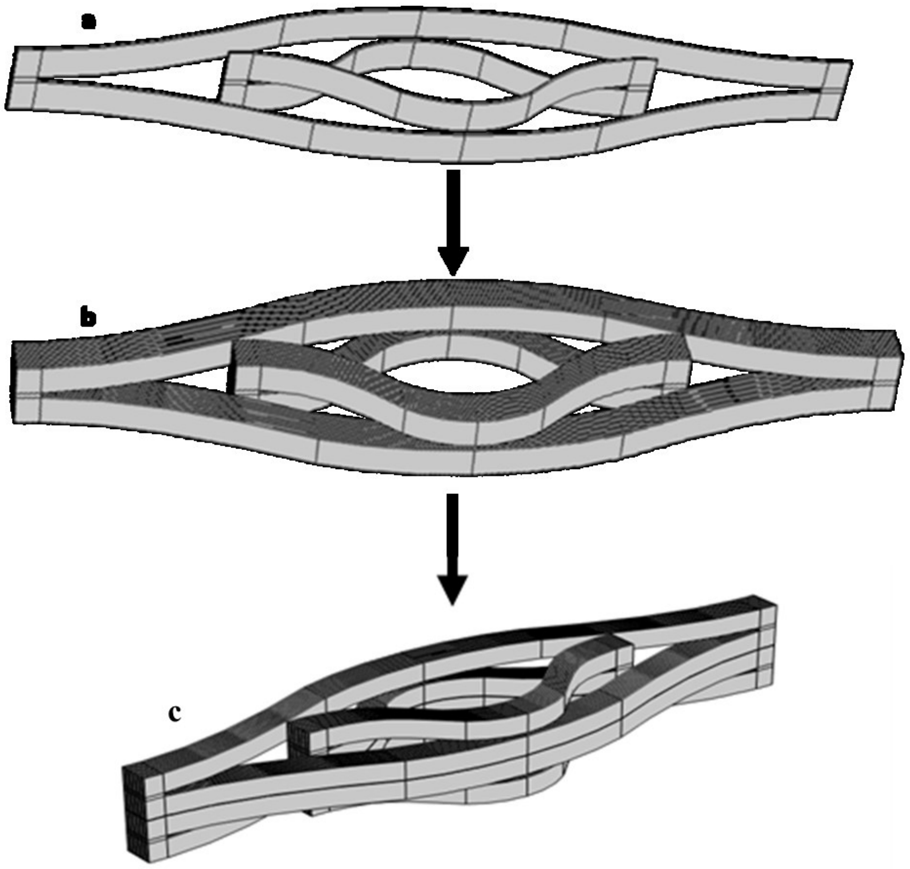

Figure 7-2. Optimised ring magnet composed from mirrored or offset stacking of two partially slitted rings. (a) two individual rings. (b) stacking of the rings. (c) Final optimised ring magnet.

Figure 7-2 shows the new ring magnet design. The length of the inner ring is smaller than the outer ring. The outer ring length is adjusted to properly fit the inner ring without having stress on the edges of the ring stacks. These rings were named according to their length: smaller ring and larger rings. The fabrication process of the new optimised design is the same as the previous design already explained in section 4.2. This design differs only in the stacking structure. The two rings are shown in Figure 7-2 (a) placed flipped to each other. This flipping makes the opposite loops of two rings face each other. The rings are then stacked to form a magnet. It can be termed as mirrored or offset stacking of the rings. Figure 7-2 (b) shows the offset stacking of the rings. After stacking them, they are doubled to form the new magnet shown in Figure 7-2 (c).

7.3 Field distribution of the new design

The optimised design is more symmetrical than the previous design in terms of the field distribution in the centre of the trapped magnetic field. Figure 7-3 (a) shows the orientation of the symmetrical ring magnet. It is obtained by taking the cut plane in the YZ direction, where the X coordinate is taken as zero. As can be seen in Figure 7-3 (b) the magnetic field distribution is symmetrical in the vertical direction. The arrows show the direction of the magnetic field. The bar shows the strength of the trapped field at different positions in the centre of the new magnet.

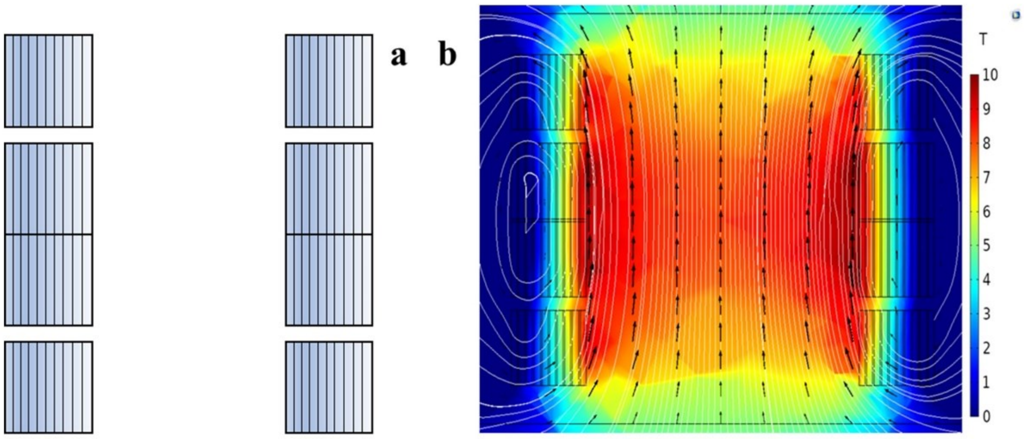

Figure 7-3. (a) Orientation of the symmetric new ring magnet which has avoided angle deflection of the trapped magnetic field. (b) The trapped magnetic field distribution of the ring magnet.

It can be seen that both stacks of smaller and larger rings show similar behaviour in terms of the field distribution. The gap between the two sides shows the length difference between the two stacks.

7.4 COMSOL model

The COMSOL model was implemented to estimate the trapped magnetic field and its distribution inside the magnet. All the settings are the same as explained in section 3.4.1, but instead of implementing two stacks of HTS rings, four stacks were implemented. The main difference is the new critical current model which was implemented in the new model to estimate the trapped field at 4.2 K.

7.4.1 A critical current mathematical model

The modelling explained in section 3.4.1 was first applied to estimate the trapped field of the new ring magnet, but it was noted that the external field profile was not sufficient to saturate the ring magnet fully. The data available for the 2G HTS coated conductor was only up to 7 T, but the saturation field requirement was higher than 9 T. For this purpose, a mathematical model for coated conductors made from (RE)BCO material describing the angular dependence of the transport critical current in the presence of the external magnetic field at a fixed temperature was used whose uncertainty is less than 10% [148]. This model accurately predicts the performance of coated conductors under high magnetic fields and is based on experimental data analysis of different published sources. The aspects considered depends on superconductor characterization, design of tapes or coils, and their quality and performance.

The Levenberg–Marquardt algorithm was used to estimate the critical current of the tapes under the influence of an external magnetic field and at the fixed temperature of 4.2 K. The desired equation of the critical current is given as:

$$I_c(B,\theta) = \frac{k_0}{(B+\beta_0)^{\alpha_0}} + \frac{k_1}{(B+\beta_1)^{\alpha_1}} \times \left[\omega_1^2(B)\cos^2(\theta-\varphi_1) + \sin^2(\theta-\varphi_1)\right]^{-\frac{1}{2}} \quad 7\text{-}1$$

where $\omega(B)$ is given by the relationship:

$$\omega(B) = c\left[B + \left(\frac{1}{c}\right)^{\frac{5}{3}}\right]^{\frac{3}{5}} \quad 7\text{-}2$$

Equation 7-1 provides a non-linear fit for the critical current I_c, which is defined in terms of the magnetic field B, angle θ, and the required parameter values listed in Table 7-1.

Table 7-1. Parameter values for the non-linear fit defined by equation 7-1 [148]

Parameter	**Value**
k_0	8870
k_1	18500
α_0	1.30
α_1	0.809
$\boldsymbol{\beta}_0$	13.8
$\boldsymbol{\beta}_1$	13.8
φ_1	-0.180^0
c	2.15

7.4.2 Final COMSOL model

In this new model, there were greater numbers of faces, domains, and distribution edges, so to make our work easier and quicker, each selection was defined by explicits in definitions. Each explicit was named according to the part for which it was defined. These explicits were used for meshing rather than selecting the domains. They helped to define the number of elements for each segment separately. In this model, the length of the stacks awere different for the inner rings and the outer rings, so homogenization of both stacks was needed to be given a different number of elements according to the lengths. The critical current obtained from equation 7-1, was used in equation 3.28 to obtain the critical current density of the tape and further substituted in the E-J power law for superconducting domains. The I_c profile used in the previous 3D model was replaced by the mathematical expression for this new model. A refinement area was also created around the stacked rings with finer meshing to decreases the computing time as shown in

Figure 7-4. Still, this model took more than 4 hours to run a single model as compared to the previous model which took approximately 2 hours or less.

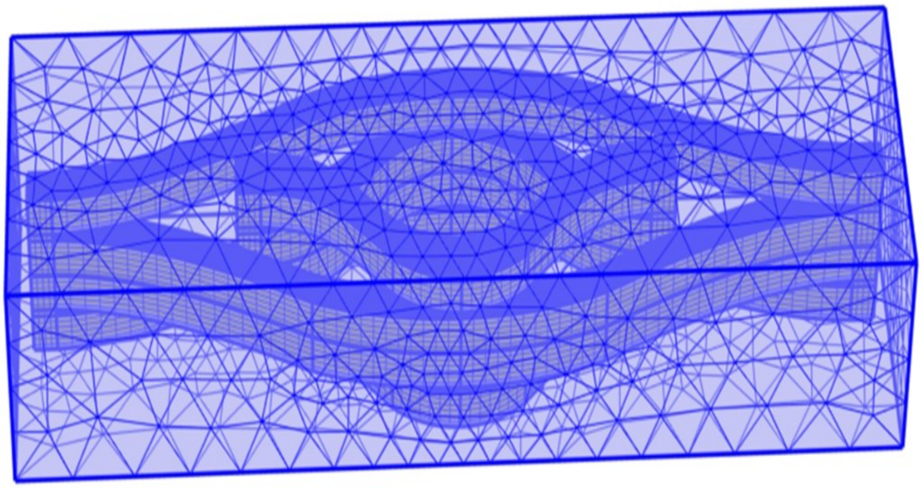

Figure 7-4. Optimised ring magnet after meshing, making it a homogenised model.

7.5 Trapped field results

The different configurations for this optimised ring magnet model have been created to predict its behaviour when it was subjected to an external magnetic field. The initially applied field was 12 T, which ramped down to zero by 0.1 sec, after which there was an additional 0.1 sec after magnetization to note the flux creep. The total applied magnetic field time was 0.2 sec. Here, three sensors were placed 6 mm apart from each other. The total middle diameter of the tube was 23 mm. The three sensors were named as H1, H2 and H3 respectively. H1 lay near to the closed side of small ring stack, with H2 in the middle, and H3 near to the closed end of the large ring stack. H1 lies 6 mm towards the closed side of the small ring from the middle while H3 lay 6 mm towards the closed side of the large ring. Figure 7-5 shows the position of the sensors at which trapped field readings were taken from the model.

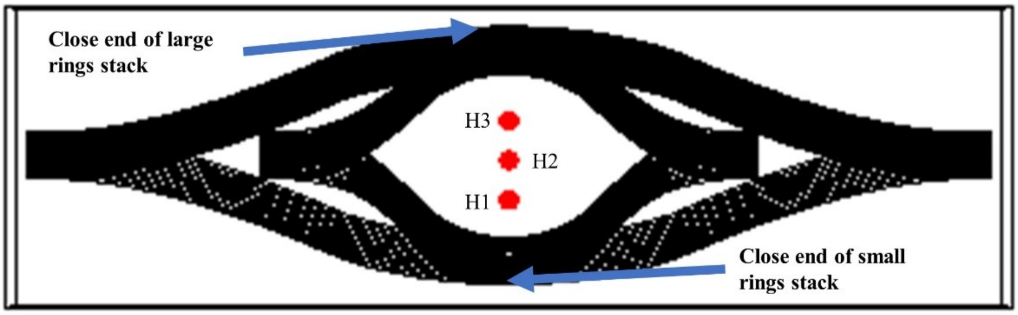

Figure 7-5. Sensor positions in the overall configuration of the optimised ring design

In the first configuration, both the small ring stacks and large ring stacks have the same number of rings. The total count of the rings was 400, which was homogenised as 40 rings in the model. Each ring in the model has the critical current distribution of 10 original rings. 20 homogenised rings were created for the small stacks and 20 homogenised rings for thelarge stacks. Figure 7-6 (a) shows the actual external field applied during the field cooling experiment. It shows that the external field became zero at 0.1 sec and from 0.1 sec to 0.2 sec it was kept zero. Figure 7-6 (b) shows the results for this configuration. The trapped field is 9.4 T near the small ring closed ends. The remaining two trapped fields differed minutely, and their value is approximately 9 T. This clearly shows that this optimised design has improved the field distribution and increased trapped field. Figure 7-6 (c) shows the result of the configuration when the larger stack rings number decreases to 70 instead of 100, but the smaller stack rings remains constant at 100. It shows that the trapped field decreases to 8.5 T and 7.9 T, respectively. Figure 7-6 (d) shows the outer rings number decreasing by half; this shows that the difference in the trapped fields values started to increase and the field symmetricity started to decrease along with the further decrease in the maximum trapped field. Figure 7-6 (e) shows the last modelled configuration, in which the effect of the small stacks of rings was examined. It gives the lowest trapped field, but the field distribution was symmetrical.

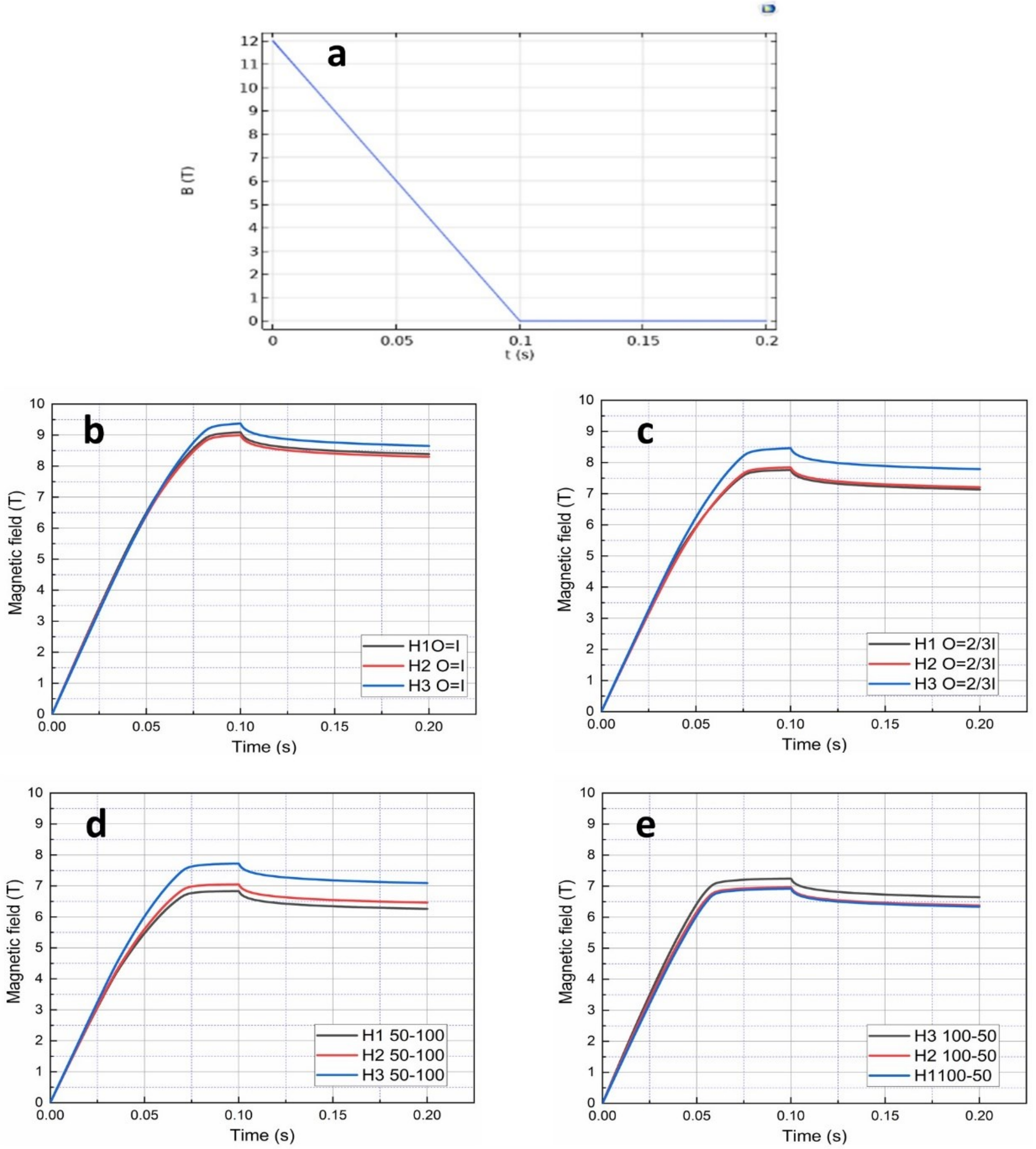

Figure 7-6. Modelling result for four different configurations. (a) the actual external field profile applied during field cooling (b) outer and inner stacks are equal. (c) outer is 2/3 of inner stack in number. (d) inner is one half of outer. (e) outer is one half of inner.

These different configurations for the optimised ring magnet design explain the behaviour of two stacks of rings (large and small stacks). It explains that the smaller size stacked rings have a greater impact on the trapped field of the magnet while the larger size stacked rings have more contribution towards the symmetricity of the field distribution. It was also noted that decreasing the larger stacked rings also decreased the trapped field, but the impact was less than that noticed by a decrease of smaller stacked rings. The best configuration was to use an equal number of stacked rings for a maximum trapped field and better field distribution. The difference between the trapped fields was due to the length of the rings. The smaller ring stack is more or less circular while the larger rings are elongated at the ends.

In the original model, the field distribution was not symmetrical. Near to the closed end, the trapped field was at a maximum, and a reduction in the trapped field was noticed as the sensor moved toward the open end. However, in this optimised design, this imbalanced field distribution greatly improved. For comparison of the two ring stacks, the original magnet position pattern was followed. The closed-end was assigned to the overlapping stack of smaller rings, and the open-end was located near the overlapping stack of larger rings.

Table 7-2. Trapped field values at different positions for the original design and optimised design

Field position	**Original design**	**Optimised design**
Field near the closed end	4.6 T	9.4 T
Field in the middle	4.19 T	9.1 T
Field near the open end	3.8 T	9 T

The difference in the trapped field values clearly shows that the optimised design has better homogenization of the trapped field in the middle. Here, the difference of the inner diameter is ignored. For the original design, it was 10 mm while for optimised design it was 23 mm.

Table 7-3. Percentage field discrepancy from the centre between the original design and optimised design

Field discrepancy	**Original design**	**Optimised design**
Between open side and centre	9 %	1 %
Between closed side and centre	8 %	3 %

As mentioned in the table, the field distribution discrepancy in the middle of the magnet improved significantly. Table 7-2 and Table 7-3 explains that in the original design, the field discrepancy was 17% between the two ends while in the optimised design, it is only 4 % between the two ends.

7.6 Field and current distribution

As already mentioned, the stack of smaller rings contributes more towards the overall trapped field, and the stack of larger rings contributes more towards the field homogenization. To prove this, the trapped fields were compared for smaller and larger rings separately, as shown in Figure 7-7. Figure 7-7(a) shows the trapped field for the larger rings, while Figure 7-7 (b) shows the trapped field results for the smaller rings. These results clearly show that the smaller rings trap more field than the larger rings. These field values were measured in the middle of the two ring stacks in the same position. The inner diameter was also kept the same for both configurations, at 23 mm. It was also noted that the field distribution was also the same as already explained in section 6. The outer magnet trapped a maximum trapped field of 4.9 T while a smaller ring stack trapped a field of 5.9 T. This field was near the overlapping layer.

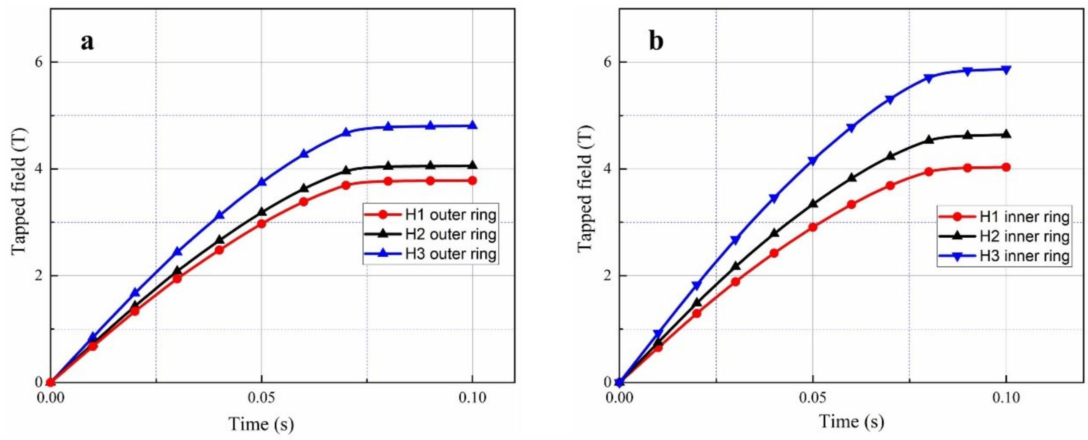

Figure 7-7. Trapped field results for larger and smaller rings stacks separately. (a) Trapped field of larger ring stacks with a peak field of 4.9 T; (b) Trapped field of the smaller ring stacks with the peak trap field of 5.9 T.

The current distribution of the smaller rings and larger rings was also examined. It was noted that the induced current value in the smaller rings was lower than that of the larger rings. The field distribution was the same. Also, the penetration pattern for both the stacks was the same. The penetration of the domains was from both the inner and outer side of the stack. For both stacks, Rings 1-0 and Ring 91-100, which are the innermost and outermost rings respectively, become saturated first, followed by the next innermost and outermost rings as shown in Figure 7-8. Figure 7-8 (a) is the induced current in the superconducting domains for larger rings. Figure 7-8 (b) is the superconducting domains induced currents for smaller rings.

The smaller rings have a higher trapped field than the larger rings, and even the induced current values is less than that of the larger rings. This is due to the geometry difference between the two different size rings. The circular shape has more impact on the trapped field while the elongated shape contributes more towards the homogenization of the field.

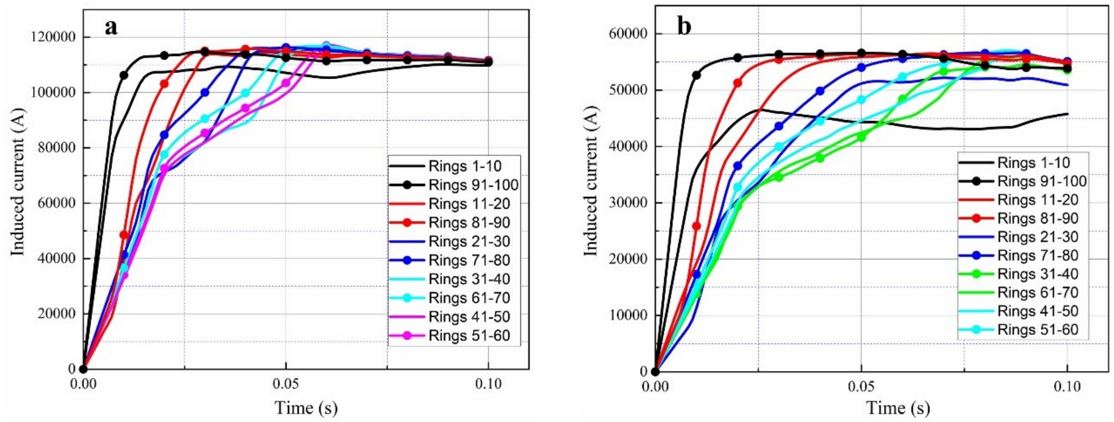

Figure 7-8. The induced current in superconducting domains. (a) Induced current for larger rings. (b) Induced current for smaller rings

7.7 Proposed Sample design

The sample design has been finalised. The sample will be created using Superpower tapes. The detail of the sample is the same as that explained in section 4.5, but instead of single cut length rings, two different cut length rings are created. For smaller rings, the cut length is 75 mm while for the larger rings, the cut length is approximately 140 mm. The tape width is 12 mm and the sides are 4 mm for both rings. Figure 7-9 a) and b) shows the schematic of the slitted tape for smaller and larger rings, respectively. Figure 7-9 c) shows the new sample holder with labelled dimensions.

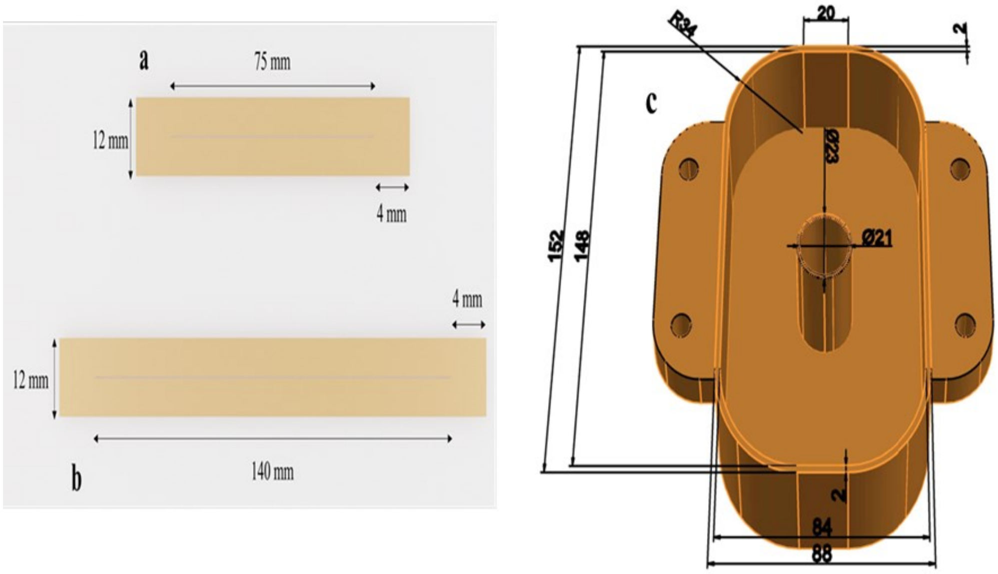

Figure 7-9. Schematic of slitted tapes for smaller and larger rings. (a) inner smaller rings dimensions. (b) outer larger rings dimensions. (c) the proposed holder design with labelled dimensions.

7.8 Conclusion

This chapter explains a new optimised ring magnet design which provides homogenised field distribution and can trap a higher magnetic field. The trapped field distribution discrepancy has decreased from 17% to 4% in the middle of the magnet. The magnet design has two different stacks of different length rings, and their impact on the trapped field at the centre was examined. The smaller rings have a greater impact on the trapped field while the larger rings contribute more towards the field homogenization. The induced current pattern for the two different sizes of rings was also examined. The current pattern is similar to the original magnet design so that the innermost and the outermost ring currents penetrate simultaneously.

8 CONCLUSION AND FUTURE WORK

In this thesis, a new superconducting ring magnet has been designed and tested by both experimental and numerical methods. 2G HTS tapes commercially available in 12 mm width were used to create superconducting rings that provide a new approach to trapped field magnets. These ring magnets can achieve higher magnetic fields with a larger diameter. The ring magnet was magnetized using the field cooling method. The new record trapped field for this magnet was 4.9 T at 25 K, measured in the middle of the magnet. The field distribution in the centre and current distribution within the rings were discussed. Also, the flux creep behaviour of the magnet was observed, which was logarithmic. The original design had a non-symmetrical field and current distribution. To homogenise the field distribution, a new optimised ring magnet design was created and discussed. The new design has an improved field distribution in the middle.

A finite element method was implemented using the COMSOL Multiphysics software and discussed in chapter 3. The Maxwell equations were implemented on HTS rings by using H-formulation and the E-J power law. Both 2D and 3D homogenised models were created and compared. The 2D model was axis-symmetric and in the 3D model, the actual dimensions of the ring magnet were taken into account. In the 3D homogenised model, ten HTS rings were replaced by one single domain having the same critical current penetration equals to 10 HTS rings.

In order to validate the modelling results, practical samples were created. In chapter 4, different sample preparations were discussed. This chapter explained the overall fabrication process of making the superconducting rings from 2G HTS coated conductors. Specific details for each magnet sample were also discussed. The positions of the hall sensors and their configuration were explained. The process of impregnation for each magnet was also discussed.

In chapter 5, the experimental setup used to magnetize the ring magnets was explained and results obtained during these experiments were also discussed. The experimental results for different samples were compared with the modelling results. The reasons for the mismatch between the modelling and experiment results were also discussed. The measured critical currents for different tapes after splitting were also presented in chapter 5. It was noted that these ring magnets could achieve higher trapped fields, and their fabrication process is very simple.

Chapter 6 discussed the field distribution and induced current penetration into the superconducting domains of the ring magnet. The field distribution of the original ring magnet design was non-symmetrical which was due to the geometry of the rings. The 3D model was used to predict the trapped field of the ring magnet at different temperatures. Different ramping rates were implemented, which slightly decreased the trapped field in the middle of the ring magnet.

Chapter 7 demonstrated the new optimised design to improve the field homogenization. A comparison of two ring magnet designs was made, the new design showing significant improvement in the field distribution in the middle. The new ring magnet was also examined for different configurations and the impact of each configuration on the result was discussed.

In conclusion, this thesis is the comprehensive study of the ring magnets created from 2G HTS coated conductors. It explains how to practically create the ring magnet and to understand their performance both practically and mathematically.

The outlook for ring magnets made from 2G HTS coated conductors provides potential prospects for practical application such as in motors and generators. They can be used in the rotors for fully superconducting machines, but proper research is required to devise a mechanism for magnetizing them. They can also be used as magnetic bearings for levitation applications, but the interaction between levitational forces and ring magnet geometry needs careful attention. These ring magnets can be used as strong magnetic shields to provide a high aspect ratio and flexibility of layers with a minimum air gap. The shielding factor of the ring magnet should be adequately investigated along the axis for better understanding of structural non-uniformities. The 2G HTS CC’s critical current I_c is easily measurable which makes predicting the trapped field simple. The challenges related to this new magnet need to be properly investigated before using them for practical applications. This thesis focuses on the trapped field in the middle and its homogenization for this new ring magnet, but the impact of the elongated ends of the rings should be adequately investigated in a rotating environment. The non-uniformities in the geometry of the rings should be minimised to enhance the application scope of this new magnet. The maximum stress limit of the tapes while opening the slit and adjusting the inner diameter requires more detailed study so that ends of the lengths of the optimised ring magnet can be improved. A deeper study for current induction in multiple rings is required to improve the robustness of these rings magnets. The HTS ring magnet behaviour during ZFC should be properly investigated, and more experiments should be performed in terms of the critical current density J_c dependence with the magnetic field B . Different magnetization processes, including flux pumping and pulse-field magnetization (PFM), should be tested to achieve the best temporal stability of the field for practical applications.

9 REFERENCES

[1] EIA, “International Energy Outlook 2019 (USEFUL TABLES),” 2019.

[2] E. Indd, “The ABB energy efficiency & productivity improvement plan Efficient control of motor-driven applications.”

[3] C. McNaught, “Running smoothly: making motors more efficient,” *IEE Rev.*, vol. 39, no. 2, p. 89, 1993.

[4] D. Zhou, M. Izumi, M. Miki, B. Felder, T. Ida, and M. Kitano, “An overview of rotating machine systems with high-temperature bulk superconductors,” *Supercond. Sci. Technol.*, vol. 25, no. 10, p. 103001, Aug. 2012.

[5] H. K. Onnes, “The resistance of pure mercury at helium temperatures,” *Commun. Phys. Lab. Univ. Leiden*, vol. 12, p. 1911, 1911.

[6] J. G. Bednorz and K. A. Müller, “Possible high Tc superconductivity in the Ba-La-Cu-O system,” *Zeitschrift für Phys. B Condens. Matter*, vol. 64, no. 2, pp. 189–193, Jun. 1986.

[7] M. K. Wu *et al.*, “Superconductivity at 93 K in a new mixed-phase Yb-Ba-Cu-O compound system at ambient pressure,” *Phys. Rev. Lett.*, vol. 58, no. 9, pp. 908–910, 1987.

[8] A. C. Rose-Innes and E. H. Rhoderick., *Introduction to superconductivity*, 1st ed. Oxford ; New York : Pergamon Press, 1978.

[9] C. M. Rey and A. P. Malozemoff, “Fundamentals of superconductivity,” in *Superconductors in the Power Grid: Materials and Applications*, Elsevier Ltd, 2015, pp. 29–73.

[10] Coalition for the Commercial Application of Superconductors, “CCAS - Coalition for the Commercial Application of Superconductors.” [Online]. Available: http://www.ccas-web.org/superconductivity/#image1. [Accessed: 07-Apr-2020].

[11] F. N. Werfel, U. Floegel-Delor, R. Rothfeld, B. Goebel, D. Wippich, and T. Riedel, “Modelling and construction of a compact 500 kg HTS magnetic bearing,” *Supercond. Sci. Technol.*, vol. 18, no. 2, p. S19, Dec. 2005.

[12] T. A. Coombs, A. Cansiz, and A. M. Campbell, “A superconducting thrust-bearing system for an energy storage flywheel,” *Supercond. Sci. Technol.*, vol. 15, no. 5, pp. 831–835, Apr. 2002.

[13] T. Oka *et al.*, “Application of HTS bulk magnet system to the magnetic separation techniques for water purification,” *Phys. C Supercond. its Appl.*, vol. 468, no. 15–20, pp. 2128–2132, 2008.

[14] J. Wang *et al.*, “The first man-loading high temperature superconducting Maglev test vehicle in the world,” *Phys. C Supercond. its Appl.*, vol. 378–381, no. PART 1, pp. 809–814, 2002.

[15] D. W. Hazelton *et al.*, “Recent developments in 2G HTS coil technology,” in *IEEE Transactions on Applied Superconductivity*, 2009, vol. 19, no. 3, pp. 2218–2222.

[16] M. Noe and M. Steurer, “High-temperature superconductor fault current limiters: Concepts, applications, and development status,” *Supercond. Sci. Technol.*, vol. 20, no. 3, p. R15, Jan. 2007.

[17] C. S. Weber, C. T. Reis, A. Dada, T. Masuda, and J. Moscovic, “Overview of the underground 34.5 kV HTS power cable program in Albany, NY,” in *IEEE Transactions on Applied Superconductivity*, 2005, vol. 15, no. 2 PART II, pp. 1793–1797.

[18] L. Masur *et al.*, “Long length manufacturing of high performance BSCCO-2223 tape for the Detroit Edison Power Cable Project,” in *IEEE Transactions on Applied Superconductivity*, 2001, vol. 11, no. 1 III, pp. 3256–3260.

[19] M. W. Rupich *et al.*, “Advances in second generation high temperature superconducting wire manufacturing and R&D at American Superconductor Corporation,” *Supercond. Sci. Technol.*, vol. 23, no. 1, p. 014015, Dec. 2010.

[20] M. W. Rupich *et al.*, “The development of second generation HTS wire at American superconductor,” in *IEEE Transactions on Applied Superconductivity*, 2007, vol. 17, no. 2, pp. 3379–3382.

[21] D. Larbalestier, A. Gurevich, D. Matthew Feldmann, and A. Polyanskii, “High-Tcsuperconducting materials for electric power applications,” in *Materials for Sustainable Energy: A Collection of Peer-Reviewed Research and Review Articles from Nature Publishing Group*, World Scientific Publishing Co., 2010, pp. 311–320.

[22] H. L. and F. A. L. F. London, “The electromagnetic equations of the supraconductor,” *Proc. R. Soc. London. Ser. A - Math. Phys. Sci.*, vol. 149, no. 866, pp. 71–88, Mar. 1935.

[23] J. Bardeen, L. N. Cooper, and J. R. Schrieffer, “Theory of superconductivity,” *Phys. Rev.*, vol. 108, no. 5, pp. 1175–1204, Dec. 1957.

[24] P. R. M. Fernandes, “Lecture Notes : BCS theory of superconductivity,” 1911.

[25] M. Cyrot, “Ginzburg-Landau theory for superconductors,” *Reports on Progress in Physics*, vol. 36, no. 2. IOP Publishing, pp. 103–158, 01-Feb-1973.

[26] K. Fossheim and A. Sudbø, *Superconductivity Physics and Applications*. Chichester: John Wiley & Sons, Ltd., 2004.

[27] C. P. J. Poole, H. A. Farach, R. J. Creswick, and R. Prozorov, *Superconductivity, Second Edition*. Academic Press, 2007.

[28] A. Patel, “Pulsed Field Magnetization of Composite Superconducting Bulks for Magnetic Bearing Applications,” 2013. [Online]. Available: https://www.repository.cam.ac.uk/handle/1810/256579. [Accessed: 13-Apr-2020].

[29] H. F. Hess, R. B. Robinson, R. C. Dynes, J. M. Valles, and J. V. Waszczak, “Scanning-Tunneling-Microscope Observation of the Abrikosov Flux Lattice and the Density of States near and inside a Fluxoid,” *Phys. Rev. Lett.*, vol. 62, no. 2, pp. 214–216, Jan. 1989.

[30] W. Wang, “An Investigation Into High Temperature Superconducting Flux Pump Technology With The Circular Type Magnetic Flux Pump,” 2014. [Online]. Available: https://www.repository.cam.ac.uk/handle/1810/245420. [Accessed: 14-Apr-2020].

[31] S. R. Foltyn *et al.*, “Materials science challenges for high-temperature superconducting wire,” *Nat. Mater.*, vol. 6, no. 9, pp. 631–642, Sep. 2007.

[32] C. P. BEAN, “Magnetization of High-Field Superconductors,” *Rev. Mod. Phys.*, vol. 36, no. 1, pp. 31–39, Jan. 1964.

[33] Y. B. Kim, C. F. Hempstead, and A. R. Strnad, “Magnetization and critical supercurrents,” 1963.

[34] Y. B. Kim, C. F. Hempstead, and A. R. Strnad, “Critical persistent currents in hard superconductors,” *Phys. Rev. Lett.*, vol. 9, no. 7, pp. 306–309, Oct. 1962.

[35] D. X. Chen and R. B. Goldfarb, “Kim model for magnetization of type-II superconductors,” *J. Appl. Phys.*, vol. 66, no. 6, pp. 2489–2500, Sep. 1989.

[36] G. Denis M., “Analysis of Superconductor Magnetization Hysteresis,” *J. Sib. Fed. Univ. Math. Phys.*, vol. 11, no. 2, pp. 219–221, May 2018.

[37] D. A. Balaev *et al.*, “Increase in the magnetization loop width in the Ba0.6K 0.4BiO3 superconductor: Possible manifestation of phase separation,” *J. Exp. Theor. Phys.*, vol. 118, no. 1, pp. 104–110, Jan. 2014.

[38] A. P. Malozemoff, “Flux creep in high temperature superconductors,” *Phys. C Supercond.*, vol. 185–189, no. PART 1, pp. 264–269, Dec. 1991.

[39] J. Bardeen and M. J. Stephen, “Theory of the motion of vortices in superconductors,” *Phys. Rev.*, vol. 140, no. 4A, p. A1197, Nov. 1965.

[40] P. W. Anderson, “Theory of Flux Creep in Hard Superconductors,” *Phys. Rev. Lett.*, vol. 9, no. 7, pp. 309–311, Oct. 1962.

[41] M. R. Beasley, R. Labusch, and W. W. Webb, “Flux creep in type-II superconductors,” *Phys. Rev.*, vol. 181, no. 2, pp. 682–700, May 1969.

[42] F. M. Smits, “Measurement of Sheet Resistivities with the Four-Point Probe,” *Bell Syst. Tech. J.*, vol. 37, no. 3, pp. 711–718, 1958.

[43] A. Gladun, G. Fuchs, K. Fischer, D. Busch, R. Eujen, and J. Huedepohl, “Critical Current Densities and Activation Energy of BiPbSrCaCuO Tapes,” *IEEE Transactions on Applied Superconductivity*, vol. 3, no. 1. pp. 1390–1393, 1993.

[44] "45 Tesla, 32 mm Bore Hybrid Magnet (Cell 15) - MagLab." [Online]. Available: https://nationalmaglab.org/user-facilities/dc-field/instruments-dcfield/hybrid-magnets/45-tesla-2. [Accessed: 24-Apr-2020].

[45] M. Strasik *et al.*, "A trapped field of 17.6 T in melt-processed, bulk Gd-Ba-Cu-O reinforced with shrink-fit steel," *Supercond. Sci. Technol.*, vol. 27, no. 8, p. 082001, Aug. 2014.

[46] M. Tomita and M. Murakami, "High-temperature superconductor bulk magnets that can trap magnetic fields of over 17 tesla at 29 K," *Nature*, vol. 421, no. 6922, pp. 517–520, Jan. 2003.

[47] M. Murakami, "Properties of melt-textured superconductors," *Jom*, vol. 52, no. 6, pp. 22–24, 2000.

[48] D. A. Cardwell, "Processing and properties of large grain (RE)BCO," *Mater. Sci. Eng. B*, vol. 53, no. 1–2, pp. 1–10, May 1998.

[49] D. R. Harshman and A. P. Mills, "Concerning the nature of high-Tc superconductivity: Survey of experimental properties and implications for interlayer coupling," *Phys. Rev. B*, vol. 45, no. 18, pp. 10684–10712, May 1992.

[50] R. Hott, R. Kleiner, T. Wolf, and G. Zwicknagl, "Review on Superconducting Materials," in *digital Encyclopedia of Applied Physics*, Weinheim, Germany: Wiley-VCH Verlag GmbH & Co. KGaA, 2016, pp. 1–55.

[51] H. Fujishiro, T. Naito, and M. Oyama, "Three-dimensional simulation of magnetic flux dynamics and temperature rise in HTSC bulk during pulsed field magnetization," in *Physics Procedia*, 2012, vol. 36, pp. 687–692.

[52] G. P. Lousberg *et al.*, "Pulsed-field magnetization of drilled bulk high-temperature superconductors: Flux front propagation in the volume and on the surface," *Supercond. Sci. Technol.*, vol. 22, no. 12, p. 125026, Oct. 2009.

[53] X. Chaud *et al.*, "Flux mapping at 77 K and local measurement at lower temperature of thin-wall YBaCuO single-domain samples oxygenated under high pressure," *Phys. C Supercond. its Appl.*, vol. 469, no. 15–20, pp. 1200–1206, Oct. 2009.

[54] Y. L. Jiao, L. Xiao, H. T. Ren, M. H. Zheng, and Y. X. Chen, “Jc-B characteristics for bulk single domain YBCO superconductors,” in *Physica C: Superconductivity and its Applications*, 2003, vol. 386, pp. 266–270.

[55] R. Gonzalez-Arrabal, M. Eisterer, and H. W. Weber, “Study of inhomogeneities in the flux density distribution of big monolithic (RE)Ba2Cu3O7−δ melt-textured superconductors,” *J. Appl. Phys.*, vol. 93, no. 8, pp. 4734–4738, Apr. 2003.

[56] A. B. Surzhenko, S. Schauroth, D. Litzkendorf, M. Zeisberger, T. Habisreuther, and W. Gawalek, “Growth-related profiles of remanent flux in bulk melt-textured YBaCuO crystal magnetized by pulsed fields,” *Supercond. Sci. Technol.*, vol. 14, no. 9, pp. 770–774, Aug. 2001.

[57] M. Sekino, H. Yasuda, A. Miyazoe, and H. Ohsaki, “Concentric slitting of a ring-shaped bulk superconductor for a reduction in circumferential inhomogeneity of the trapped magnetic field,” *IEEE Trans. Appl. Supercond.*, vol. 21, no. 3 PART 2, pp. 1588–1591, Jun. 2011.

[58] M. K. H. Fuchs G, Wenger C, Gladun A, Gruss S, Krabbes G, Schatzle P, “Different limitations of trapped fields in melt-textured BCO,” *inst. phys. Conf. Ser, 167*, vol. 1, pp. 111–114, 1999.

[59] A. Patel, S. C. Hopkins, and B. A. Glowacki, “Trapped fields up to 2 T in a 12 mm square stack of commercial superconducting tape using pulsed field magnetization,” *Supercond. Sci. Technol.*, vol. 26, no. 3, p. 032001, Mar. 2013.

[60] S. Hahn, S. B. Kim, M. C. Ahn, J. Voccio, J. Bascunan, and Y. Iwasa, “Trapped field characteristics of stacked YBCO thin plates for compact NMR magnets: Spatial field distribution and temporal stability,” in *IEEE Transactions on Applied Superconductivity*, 2010, vol. 20, no. 3, pp. 1037–1040.

[61] K. Selva and G. Majkic, “Trapped magnetic field profiles of arrays of (Gd,Y)Ba2Cu 3Ox superconductor tape in different stacking configurations,” *Supercond. Sci. Technol.*, vol. 26, no. 11, Nov. 2013.

[62] A. G. Page *et al.*, “The effect of stabilizer on the trapped field of stacks of superconducting tape magnetized by a pulsed field,” *Supercond. Sci. Technol.*, vol. 28, no. 8, Aug. 2015.

[63] B. A. Glowacki *et al.*, “A trapped field of 17.7 T in a stack of high temperature superconducting tape,” *Supercond. Sci. Technol.*, vol. 31, no. 9, p. 09LT01, Sep. 2018.

[64] T. Tamegai, T. Hirai, Y. Sun, and S. Pyon, “Trapping a magnetic field of 7.9 T using a bulk magnet fabricated from stack of coated conductors,” *Phys. C Supercond. its Appl.*, vol. 530, pp. 20–23, Nov. 2016.

[65] G. Krabbes, G. Fuchs, W.-R. Canders, H. May, and R. Palka, “Applications in Magnet Technologies and Power Supplies,” in *High Temperature Superconductor Bulk Materials*, Weinheim, FRG: Wiley-VCH Verlag GmbH & Co. KGaA, 2006, pp. 279–292.

[66] R. L. Fagaly, “Superconducting quantum interference device instruments and applications,” *Rev. Sci. Instrum.*, vol. 77, no. 10, p. 101101, Oct. 2006.

[67] C. Navau *et al.*, “Critical state in finite type-II superconducting rings,” *Phys. Rev. B - Condens. Matter Mater. Phys.*, vol. 71, no. 21, p. 214507, Jun. 2005.

[68] J. R. Hull, “Superconducting bearings,” *Supercond. Sci. Technol.*, vol. 13, no. 2, pp. R1–R15, Feb. 2000.

[69] B. Surzhenko, M. Zeisberger, T. Habisreuther, W. Gawalek, and S. Uspenskaya, “Intergrain and intragrain currents in bulk melt-grown YBa2Cu3O7−δ rings,” *Phys. Rev. B - Condens. Matter Mater. Phys.*, vol. 68, no. 6, p. 064504, Aug. 2003.

[70] A. P. Paulikas *et al.*, “Critical current across grain boundaries in melt-textured (formula presented) rings,” *Phys. Rev. B - Condens. Matter Mater. Phys.*, vol. 64, no. 14, p. 144507, Sep. 2001.

[71] H. Ohsaki, T. Shimosaki, and N. Nozawa, “Pulse field magnetization of a ring-shaped bulk superconductor,” *Supercond. Sci. Technol.*, vol. 15, no. 5, p. 322, May 2002.

[72] H. Teshima, T. Tawara, J. Kobuchi, T. Suzuki, and R. Shimada, “Ring-shaped flywheel energy storage systems with superconducting levitation,” in *Proceedings of Power Conversion Conference - PCC ’97*, 1997, vol. 2, pp. 701–706.

[73] T. Herzog, H. Radovan, P. Ziemann, and E. Brandt, “Experimental test of theories

describing the magnetic ac susceptibility of differently shaped superconducting films: Rectangles, squares, disks, and rings patterned from films," *Phys. Rev. B - Condens. Matter Mater. Phys.*, vol. 56, no. 5, pp. 2871–2881, Aug. 1997.

[74] L. D. Landau, E. M. Lifshitz, and A. L. King, "Electrodynamics of Continuous Media," *American Journal of Physics*, 1961. [Online]. Available: https://archive.org/details/ElectrodynamicsOfContinuousMedia/page/n7. [Accessed: 04-May-2020].

[75] E. H. Brandt and M. Indenbom, "Type-II-superconductor strip with current in a perpendicular magnetic field," *Phys. Rev. B*, vol. 48, no. 17, pp. 12893–12906, Nov. 1993.

[76] V. S. da Cruz, G. T. Telles, B. M. O. Santos, A. C. Ferreira, and R. De Andrade Junior, "Study of the Voltage Behavior of Jointless Superconducting 2G Loops during Pulse Magnetization," *IEEE Trans. Appl. Supercond.*, pp. 1–1, Jan. 2020.

[77] H. G. Lee *et al.*, "Design and fabrication of permanent mode magnet by using coated conductor," *Phys. C Supercond. its Appl.*, vol. 445–448, no. 1–2, pp. 1099–1102, Oct. 2006.

[78] Woo-Seok Kim *et al.*, "Magnetic Field Stability of a Small YBCO Magnet in Persistent Current Mode," *IEEE Trans. Appl. Supercond.*, vol. 19, no. 3, pp. 2194–2197, 2009.

[79] Woo-Seok Kim *et al.*, "Thermal Analysis of PCS for an HTS Pancake Coil in Persistent Current Mode," *IEEE Trans. Appl. Supercond.*, vol. 20, no. 3, pp. 1009–1012, Jun. 2010.

[80] G. A. Levin *et al.*, "Persistent current in coils made out of second generation high temperature superconductor wire.," *Appl. Phys. Lett.*, vol. 93, no. 6, p. 062504, Aug. 2008.

[81] V. S. Da Cruz, G. T. Telles, A. C. Ferreira, and R. De Andrade, "Pulse Magnetization of Jointless Superconducting Loops for Magnetic Bearings Height Control," *IEEE Trans. Appl. Supercond.*, vol. 28, no. 4, pp. 4–7, 2018.

[82] F. G. R. Martins, F. Sass, A. C. Ferreira, and R. de Andrade, "A Novel Magnetic Bearing Using REBCO Double Crossed Loop Coils," *IEEE Trans. Appl.*

Supercond., vol. 28, no. 4, pp. 1–5, Jun. 2018.

[83] F. Sass, A. Ramos de Castro, G. Gonçalves Sotelo, and R. de Andrade, “Persistent currents in a magnetic bearing with coated conductors,” *J. Appl. Phys.*, vol. 118, no. 20, p. 203901, Nov. 2015.

[84] J. Kosa, “Qualification of YBCO rings and 100% YBCO wire loops with the transformation of the DC magnetic field,” *Mater. Sci. Forum*, vol. 670, pp. 11–20, 2011.

[85] J. Kosa, I. Vajda, and A. Gyore, “Application possibilities with continuous YBCO loops made of HTS wire,” *J. Phys. Conf. Ser.*, vol. 234, no. PART 3, 2010.

[86] J. Kosa, I. Vajda, and L. Kovacs, “Novel self-limiting transformer with active magnetic short circuit using perfect YBCO wire loops,” *IEEE Trans. Appl. Supercond.*, vol. 21, no. 3 PART 2, pp. 1417–1421, Jun. 2011.

[87] J. Kosa, I. Vajda, A. Gyore, and Z. Kohari, “Fault current limiter with novel arrangement of perfect YBCO loops made of HTS wire,” in *Proceedings of EPE-PEMC 2010 - 14th International Power Electronics and Motion Control Conference*, 2010.

[88] L. Wéra, J. F. Fagnard, G. A. Levin, B. Vanderheyden, and P. Vanderbemden, “A comparative study of triaxial and uniaxial magnetic shields made out of YBCO coated conductors,” *Supercond. Sci. Technol.*, vol. 28, no. 7, Jun. 2015.

[89] Y. Zheng, Y. Wang, J. Li, and Z. Jin, “Magnetization of the joint-free high temperature superconductor (RE)Ba2Cu3Ox coil by field cooling,” *AIP Adv.*, vol. 7, no. 9, p. 095218, Sep. 2017.

[90] C. Navau *et al.*, “Critical state in finite type-II superconducting rings,” *Phys. Rev. B - Condens. Matter Mater. Phys.*, vol. 71, no. 21, pp. 1–9, 2005.

[91] S. C. Wimbush and N. M. Strickland, “A Public Database of High-Temperature Superconductor Critical Current Data,” *IEEE Trans. Appl. Supercond.*, vol. 27, no. 4, Jun. 2017.

[92] J. Sheng, M. Zhang, Y. Wang, X. Li, J. Patel, and W. Yuan, “A new ring-shape high-temperature superconducting trapped-field magnet,” *Supercond. Sci.*

Technol., vol. 30, no. 9, p. 094002, Sep. 2017.

[93] S. Lee *et al.*, “Characteristics of an HTS pancake coil in persistent current mode using wind-and-flip winding method,” *IEEE Trans. Appl. Supercond.*, vol. 23, no. 3, pp. 4601305–4601305, 2013.

[94] Y. G. Park *et al.*, “Experimental Analysis on Initial Current Decay Characteristics of Persistent-Mode HTS Coil by External Alternating Magnetic Field,” *IEEE Trans. Appl. Supercond.*, vol. 25, no. 3, pp. 1–4, Jun. 2015.

[95] C. C. Rong, P. N. Barnes, G. A. Levin, J. D. Miller, D. J. Santosusso, and B. K. Fitzpatrick, “Investigation of the relaxation of persistent current in superconducting closed loops made out of YBCO coated conductors,” *IEEE Trans. Appl. Supercond.*, vol. 25, no. 3, Jun. 2015.

[96] C. F. Bunting, “Introduction to the finite element method,” 2008.

[97] T. A. Coombs, A. M. Campbell, A. Murphy, and M. Emmens, “A fast algorithm for calculating the critical state in superconductors,” *COMPEL - Int. J. Comput. Math. Electr. Electron. Eng.*, vol. 20, no. 1–4, pp. 240–252, 2001.

[98] G. Barnes, M. McCulloch, and D. Dew-Hughes, “Computer modelling of type II superconductors in applications,” *Supercond. Sci. Technol.*, vol. 12, no. 8, pp. 518–522, Aug. 1999.

[99] N. Amemiya, S. Murasawa, N. Banno, and K. Miyamoto, “Numerical modelings of superconducting wires for AC loss calculations,” *Phys. C Supercond.*, vol. 310, no. 1–4, pp. 16–29, Dec. 1998.

[100] G. Meunier, Y. Le Floch, and C. Guérin, “A nonlinear circuit coupled t - t0- φ formulation for solid conductors,” *IEEE Trans. Magn.*, vol. 39, no. 3 I, pp. 1729–1732, May 2003.

[101] Z. Hong, A. M. Campbell, and T. A. Coombs, “Numerical solution of critical state in superconductivity by finite element software,” *Supercond. Sci. Technol.*, vol. 19, no. 12, pp. 1246–1252, Dec. 2006.

[102] R. Brambilla, F. Grilli, and L. Martini, “Development of an edge-element model for AC loss computation of high-temperature superconductors,” *Supercond. Sci.*

Technol., vol. 20, no. 1, pp. 16–24, Jan. 2007.

[103] S. Stavrev *et al.*, “Comparison of numerical methods for modeling of superconductors,” *IEEE Trans. Magn.*, vol. 38, no. 2, pp. 849–852, Mar. 2002.

[104] F. Grilli *et al.*, “Finite-element method modeling of superconductors: From 2-D to 3-D,” *IEEE Trans. Appl. Supercond.*, vol. 15, no. 1, pp. 17–24, Mar. 2005.

[105] J. Rhyner, “Magnetic properties and AC-losses of superconductors with power law current-voltage characteristics,” *Phys. C Supercond. its Appl.*, vol. 212, no. 3–4, pp. 292–300, Jul. 1993.

[106] F. Grilli and S. P. Ashworth, “Measuring transport AC losses in YBCO-coated conductor coils,” *Supercond. Sci. Technol.*, vol. 20, no. 8, pp. 794–799, Aug. 2007.

[107] M. Zhang, J. Kvitkovic, S. V. Pamidi, and T. A. Coombs, “Experimental and numerical study of a YBCO pancake coil with a magnetic substrate,” *Supercond. Sci. Technol.*, vol. 25, no. 12, p. 125020, Dec. 2012.

[108] M. Zhang, K. Matsuda, and T. A. Coombs, “New application of temperature-dependent modelling of high temperature superconductors: Quench propagation and pulse magnetization,” *J. Appl. Phys.*, vol. 112, no. 4, p. 043912, Aug. 2012.

[109] M. Zhang, J. H. Kim, S. Pamidi, M. Chudy, W. Yuan, and T. A. Coombs, “Study of second generation, high-temperature superconducting coils: Determination of critical current,” *J. Appl. Phys.*, vol. 111, no. 8, Apr. 2012.

[110] V. M. R. Zermeño and F. Grilli, “3D modeling and simulation of 2G HTS stacks and coils,” *Supercond. Sci. Technol.*, vol. 27, no. 4, p. 044025, Mar. 2014.

[111] V. M. R. Zermeno, A. B. Abrahamsen, N. Mijatovic, B. B. Jensen, and M. P. Sørensen, “Calculation of alternating current losses in stacks and coils made of second generation high temperature superconducting tapes for large scale applications,” *J. Appl. Phys.*, vol. 114, no. 17, p. 173901, 2013.

[112] H. T. S. Wire, “2G HTS Wire | SuperPower 2G HTS Wire | SuperPower,” 2014. [Online]. Available: http://www.superpower-inc.com/content/2g-hts-wire. [Accessed: 08-Jan-2020].

[113] T. Doi, M. Hashimoto, S. Horii, and A. Ichinose, “Fabrication of YBa2Cu3O7

superconducting film on {100}<001> textured Cu tape via conductive buffer layers," *Mater. Trans.*, vol. 58, no. 10, pp. 1493–1499, 2017.

[114] Y. Iijima, N. Tanabe, O. Kohno, and Y. Ikeno, "In-plane aligned YBa2Cu3O7-x thin films deposited on polycrystalline metallic substrates," *Appl. Phys. Lett.*, vol. 60, no. 6, pp. 769–771, 1992.

[115] A. Goyal *et al.*, "Conductors with controlled grain boundaries: An approach to the next generation, high temperature superconducting wire," *J. Mater. Res.*, vol. 12, no. 11, pp. 2924–2940, Nov. 1997.

[116] A. P. Malozemoff, D. T. Verebelyi, S. Fleshler, D. Aized, and D. Yu, "HTS wire: Status and prospects," in *Physica C: Superconductivity and its Applications*, 2003, vol. 386, pp. 424–430.

[117] S. R. Foltyn *et al.*, "Materials science challenges for high-temperature superconducting wire," *Nat. Mater.*, vol. 6, no. 9, pp. 631–642, Sep. 2007.

[118] R. C. Duckworth *et al.*, "On the effect of NiW on the inductance and AC loss of HTS cables," in *IEEE Transactions on Applied Superconductivity*, 2005, vol. 15, no. 2 PART II, pp. 1578–1582.

[119] R. C. Duckworth *et al.*, "Transport ac loss studies of YBCO coated conductors with nickel alloy substrates," *Supercond. Sci. Technol.*, vol. 16, no. 11, pp. 1294–1298, Nov. 2003.

[120] O. Tsukamoto, S. Sekizawa, A. K. M. Alamgir, and D. Miyagi, "Methods to reduce AC losses in HTS coated conductors with magnetic substrates," *Phys. C Supercond. its Appl.*, vol. 463–465, no. SUPPL., pp. 770–774, Oct. 2007.

[121] S. H. Moon, "HTS Development and Industrialization at SuNAM Superconductor, Nano & Advanced Materials," 2014.

[122] "SuNAM Co., Ltd." [Online]. Available: http://i-sunam.com/home/en_product,1,3,1,1,1. [Accessed: 08-Jan-2020].

[123] S. P. S. Badwal, F. T. Ciacchi, and D. V. Ho, "A fully automated four-probe d.c. conductivity technique for investigating solid electrolytes," *J. Appl. Electrochem.*, vol. 21, no. 8, pp. 721–728, Aug. 1991.

[124] "Shanghai Superconductors." [Online]. Available: http://www.shsctec.com/Pages/SpecialProductList.aspx?ID=42&cl=en. [Accessed: 15-Mar-2020].

[125] "SuperPower®2G HTS Wire Specifications." [Online]. Available: http://www.superpower-inc.com/system/files/SP_2G+Wire+Spec+Sheet_for+web_2012FEC_v2_1.pdf. [Accessed: 25-Mar-2020].

[126] R. Kandasamy, X. Q. Wang, and A. S. Mujumdar, "Transient cooling of electronics using phase change material (PCM)-based heat sinks," *Appl. Therm. Eng.*, vol. 28, no. 8–9, pp. 1047–1057, Jun. 2008.

[127] T. Matsuda *et al.*, "Degradation of the performance of an epoxy-impregnated REBCO solenoid due to electromagnetic forces," *Cryogenics (Guildf).*, vol. 90, pp. 47–51, Mar. 2018.

[128] A. Badakhsh, C. W. Park, and B. Kim, "Preparation and analysis of paraffin-based phase change material using aluminum nitride as the reinforcing agent," in *FUNCTIONAL NANOSTRUCTURES PROCEEDINGS*, 2017, pp. 70–72.

[129] S. M. Shalaby, H. F. Abosheiash, S. T. Assar, and A. E. Kabeel, "Improvment of Thermal Properties of Paraffin Wax As Latent Heat Storage Material With Direct Solar Desalination Systems By Using Aluminum Oxide Nanoparticles," 2018.

[130] P. Bose and V. A. Amirtham, "A review on thermal conductivity enhancement of paraffinwax as latent heat energy storage material," *Renewable and Sustainable Energy Reviews*, vol. 65. Elsevier Ltd, pp. 81–100, 01-Nov-2016.

[131] V. V. Sychev, A. A. Vasserman, A. D. Kozlov, G. A. Spiridonov, and V. A. Tsymarny, "Thermodynamic properties of helium," *wdch*, vol. 1, 1987.

[132] A. Gurevich and H. Küpfer, "Time scales of the flux creep in superconductors," *Phys. Rev. B*, vol. 48, no. 9, pp. 6477–6487, Sep. 1993.

[133] T. Takematsu *et al.*, "Degradation of the performance of a YBCO-coated conductor double pancake coil due to epoxy impregnation," *Phys. C Supercond. its Appl.*, vol. 470, no. 17–18, pp. 674–677, Sep. 2010.

[134] J. H. Durrell *et al.*, "A trapped field of 17.6 T in melt-processed, bulk Gd-Ba-Cu-O reinforced with shrink-fit steel," *Supercond. Sci. Technol.*, vol. 27, no. 8, p. 082001, Aug. 2014.

[135] A. Patel *et al.*, "A trapped field of 17.7 T in a stack of high temperature superconducting tape," *Supercond. Sci. Technol.*, vol. 31, no. 9, p. 09LT01, Sep. 2018.

[136] H. Jin, L. Chen, and Y. H. Zhang, "Magnetic relaxation in high-temperature superconductors," *Phys. Lett. Sect. A Gen. At. Solid State Phys.*, vol. 255, no. 3, pp. 183–186, Jul. 1999.

[137] Y. Yeshurun, A. P. Malozemoff, and A. Shaulov, "Magnetic relaxation in high-temperature superconductors," *Rev. Mod. Phys.*, vol. 68, no. 3, pp. 911–949, Jul. 1996.

[138] U. Mizutani, T. Oka, Y. Itoh, Y. Yanagi, M. Yoshikawa, and H. Ikuta, "Pulsed-field magnetization applied to high-Tc superconductors," *Appl. Supercond.*, vol. 6, no. 2–5, pp. 235–246, Feb. 1998.

[139] G. M. Genkin and A. V Okomel, "Effect of magnetic-vortex interaction on the kinetics of magnetic-flux creep in type II superconductors," 1995.

[140] L. Gozzelino *et al.*, "Local magnetic investigations of MgB2 bulk samples for magnetic shielding applications," *IEEE Trans. Appl. Supercond.*, vol. 21, no. 3 PART 3, pp. 3146–3149, Jun. 2011.

[141] J. O. Wllis, M. E. McHenry, M. P. Maley, and H. Sheinberg, "Magnetic shielding by superconducting Y-Ba-Cu-O hollow cylinders," *IEEE Trans. Magn.*, vol. 25, no. 2, pp. 2502–2505, 1989.

[142] T. Sasaki, M. Tanaka, M. Morita, K. Miyamoto, and M. Hashimoto, "Magnetic Shielding by Superconducting Y-Ba-Cu-O Prepared by the Modified Quench and Melt Growth (QMG) Process," *Jpn. J. Appl. Phys.*, vol. 31, no. 4 R, pp. 1026–1032, 1992.

[143] L. Wera, J. F. Fagnard, G. A. Levin, B. Vanderheyden, and P. Vanderbemden, "Magnetic shielding with YBCO coated conductors: Influence of the geometry on its performances," *IEEE Trans. Appl. Supercond.*, vol. 23, no. 3, 2013.

[144] S. Denis, M. Dirickx, P. Vanderbemden, M. Ausloos, and B. Vanderheyden, “Field penetration into hard type-II superconducting tubes: Effects of a cap, a non-superconducting joint, and non-uniform superconducting properties,” *Supercond. Sci. Technol.*, vol. 20, no. 5, pp. 418–427, Mar. 2007.

[145] A. Patel, S. Hahn, J. Voccio, A. Baskys, S. C. Hopkins, and B. A. Glowacki, “Magnetic levitation using a stack of high temperature superconducting tape annuli,” *Supercond. Sci. Technol.*, vol. 30, no. 2, p. 024007, Feb. 2017.

[146] J. Rhyner, “Magnetic properties and AC-losses of superconductors with power law current-voltage characteristics,” *Phys. C Supercond. its Appl.*, vol. 212, no. 3–4, pp. 292–300, Jul. 1993.

[147] F. Sass, D. H. Dias, G. Sotelo, and R. De Andrade, “Superconducting levitation using coated conductors,” *IEEE Trans. Appl. Supercond.*, vol. 23, no. 3, pp. 3–7, 2013.

[148] D. K. Hilton, A. V. Gavrilin, and U. P. Trociewitz, “Practical fit functions for transport critical current versus field magnitude and angle data from (RE)BCO coated conductors at fixed low temperatures and in high magnetic fields,” *Supercond. Sci. Technol.*, vol. 28, no. 7, p. 074002, Jun. 2015.